Layer formation from multi-component electrolytic solutions

Zur Erlangung des akademischen Grades eines

DOKTORS DER INGENIEURWISSENSCHAFTEN (DR.-ING.)

von der KIT-Fakultät für Chemieingenieurwesen und Verfahrenstechnik
des Karlsruher Instituts für Technologie (KIT)
genehmigte

DISSERTATION

von

M.Sc. Christoph Helfenritter

aus Kassel

Tag der mündlichen Prüfung: 06.04.2023

Erstgutachter: Prof. Dr.-Ing. Matthias Kind
Zweitgutachterin: Prof. Dr. habil. rer. nat. Sabine Enders

Preface

The contents of this thesis originate from my time as Ph.D. candidate at the Institute for Thermal Process Engineering at the Karlsruhe Institute of Technology from February 2017 to January 2022.

My work at the institute was characterized by a great scientific freedom. I deeply acknowledge the trust that my advisor and "Doktorvater" Prof. Dr.-Ing. Matthias Kind gave me during that time. I got the time and space to develop my research topic and grow scientifically and personally. Also, I am very greatful that Prof. Dr. habil. rer. nat. Sabine Enders kindly took over the second review.

At this point I would like to thank the Deutsche Forschungsgesellschaft for the substantial financial contribution in form of NMR instrumentation within the instrumental facility Pro2NMR. With the instrumentation it was possible to measure diffusion coefficients.

To get to the point of finalization of such a thesis, many people crossed my way and have influenced this work and me as a person. My office mates Michael Barros Groß and Gina Kaysan had always lend an ear for problems popping up on the scientific journey. The same counts for all the others of the work group "AG Kind", namely Philipp Lau, Esther Laryea, Daniel Selzer, Hendrik Rehage, Nicolás Ramos and Monika Wolf. The two AG-Kind-fellows David Guse and Burkard Spiegel and my very good friend Annika Reinelt impacted this work to a certain degree as they kindly and constructively reviewed the manuscript. The coffee breaks, drinks after work and "Hallenfeste" will always bring up warm memories of the time at the institute besides the research work.

I had the opportunity to work together with many students. Advising and learning with Andreas Roth, Lingyue Liu, Aliénor Potthoff, Julius Sanders, Quintus Jünemann, Stefan Höll, Karam Swaid, Kai Bauer, Natalie Ritter, Richard Samman, Thomas Kieble, Patrick Mika, Michaela Gratzfeld and Jaroslav Knack filled me always with joy and happiness. Unfortunately, because of the novelty of this topic at the institute, not many results of Bachelor and Master students are part of this thesis. Every students thesis or work as lab assistant brought the research work forward but on the other hand setbacks were normal, from which new ideas grew.

I am very greatful and proud for having been part of this great institute with its great staff. Many co-workers became friends of mine, which cannot be taken for granted. I would like to thank Nicole Feger and Vanessa Gamer for their administrative support and the casual talks. Also, I am very greatful for the work of our workshop. I will always remind me on working with you on milling my salt layer. Thank you, Andreas Roth, Michael Wachter, Stefan Böttle, Stephan Find and Max Renaud.

Finally, I would like to thank my family and my wife Judith for their support during that time. I am happy that I got the opportunity to go to university and that it led me to this journey. Throughout my undergraduate studies and PhD years, Judy always had my back and provided endless support.

Karlsruhe, 23.04.2023
Christoph Helfenritter

Kurzfassung

Feste Oberflächen, die aus mehreren kristallinen Komponenten zusammengesetzt sind, werden häufig in der Produktgestaltung verwendet. Für pharmazeutische oder landwirtschaftliche Anwendungen werden Tabletten oder Granulate hergestellt, die mehrere Inhaltsstoffe enthalten. Diese sollen zu bestimmten Zeiten oder unter bestimmten Bedingungen ihre Wirkstoffe freisetzen. Um dies zu erreichen, sind meist zusätzliche Granulations- oder Beschichtungsschritte erforderlich. Dafür werden Lösungen oder Schmelzen mit festen Partikeln in Kontakt gebracht. Durch Verdampfen des Lösungsmittels oder Abkühlen der Flüssigkeit verfestigen sich die Bestandteile auf den Partikeln.

Neben der Produktgestaltung kommt es bei Fouling-Prozessen in Wärmeübertragern zur unbeabsichtigten Schichtbildung aus mehrkomponentigen Lösungen. Aufgrund von gelösten Stoffen in relativ hohen Mengen und Temperaturgradienten an den Wandoberflächen kann es dort zur Kristallschichtbildung kommen. Dies resultiert in unerwünschten Wärmeübertragungseinschränkungen.

Die Vorhersage der resultierenden Feststoffzusammensetzung aus kristallisierenden elektrolytischen Lösungen wird in der Literatur wenig diskutiert. Einige Arbeiten berichten von in-situ-Beschichtungsprozesse, die eine gewünschte Zusammensetzung der Oberfläche erzeugen. Damit ist es möglich, einen Wirkstoff in einem einzigen Prozessschritt mit einer anderen Komponente zu beschichten.

Ziel dieser Arbeit ist es, dem Leser eine Anleitung zur Beantwortung von Kristallisationsproblemen von Lösungen zu geben, die mehrere Komponenten enthalten. Sie soll für die Suspensionskristallisation, das Produktdesign von Granulaten und dünnen kristallinen Schichten anwendbar sein. Auch verwandte Gebiete wie Geologie, Mineralogie oder Legierungsforschung können von den Ergebnissen profitieren.

Es werden aus einer theoretischen Betrachtung drei Gruppen von Einflussgrößen ausgemacht, die es zu untersuchen gilt: Phasengleichgewichte, Kinetiken während des mehrkomponentigen Kristallwachstums und die Geschwindigkeit des Übersättigungsaufbaus (Übersättigungsrate). Das Modellsystem Na_2SO_4-Na_2CO_3-H_2O wird für die Untersuchung verwendet. In einem ersten Schritt müssen die Phasengleichgewichte und metastabilen Zonen bestimmt werden. Die Bestimmung von Phasengleichgewichten ist bereits gut bekannt, metastabile Zonen sind jedoch schwierig zu ermitteln. Die homogene Keimbildung wird nicht als Einflussfaktor auf die Schichtbildung ausgemacht. Allerdings ist deren Bestimmung dennoch für die Untersuchung und Bewertung der heterogenen und sekundären Keimbildung notwendig. Ein neuer pseudo-binärer Ansatz wird verwendet, um die Grenze der metastabilen Zone eines ternären Systems zu untersuchen. Er erweist sich als funktionell, aber die Überprüfung durch isotherme Verdampfungsexperimente führte nicht zu den ermittelten Grenzen, denn die metastabilen Zonen der Sekundärkeimbildung lagen bei beiden Materialien sehr nahe am Gleichgewichtszustand. Selbst bei sehr geringen Übersättigungen bilden beide Elektrolyte neue Keime. Dies wird bei der Entwicklung weiterer Versuchsmethoden in dieser Arbeit berücksichtigt.

Um die Kinetik des Kristallwachstums verschiedener Materialien aus hochgesättigten Lösungen zu untersuchen, wird eine neue Methode entwickelt und eingeführt. Die Absättigung eines dünnen Flüssigkeitsfilms in Kontakt mit einem kristallinen Substrat wird transient gemessen. In den Experimenten werden zwei Fälle von Mehrkomponentenkristallisation festgestellt. In den meisten Fällen wird eine gleichzeitige Kristallisation der zwei eingesetzten Salze beobachtet. In einigen wenigen Experimenten kommt es zur bevorzugten Kristallisation einer einzelnen der beiden Komponenten.

Es wird angenommen, dass der Einfluss der Übersättigungsrate auf den Schichtaufbau von Bedeutung ist, da ein schneller Übersättigungsaufbau zu einer gleichzeitigen Kristallisation aller Komponenten führen könnte. Eine langsamerer Sättigungsaufbau könnte eine Komponente begünstigen, die auskristallisieren kann, während eine andere Komponente in Lösung bleibt. Experimente zeigen jedoch, dass die Auswirkung auf die Feststoffzusammensetzung nicht stark ausgeprägt ist.

Die Ergebnisse lassen den Schluss zu, dass die Mehrkomponentenkristallisation aus der Lösung auf einem kristallinen Substrat eine geschichtete Oberfläche hervorruft. Dies hängt jedoch vor allem vom Phasengleichgewichtsverhalten und von den konkurrierenden Kristallisationskinetiken ab.

Zur mathematischen Vorhersage von Feststoffzusammensetzungen wird ein Simulationsmodell erstellt, dessen Ergebnisse allerdings von den experimentellen Ergebnissen der Schichtbildung abweichen. Die Abweichungen resultieren aus der fehlenden mathematischen Berücksichtigung von Porosität und Metastabilitätsverhalten. Dennoch sind die qualitativen Trends erkennbar.

Schließlich lässt sich eine Strategie für die Mehrkomponentenkristallisation ableiten, die entweder für das Produktdesign von Partikeln oder für andere verwandte Prozesse mit mehreren in Lösung befindlichen Komponenten verwendet werden kann.

Abstract

Solid surfaces composed of multiple crystalline components are widely used in product design. For pharmaceutical or agricultural applications, tablets or granules are produced that contain several ingredients. These are intended to release their active ingredients at specific times or under specific conditions. To accomplish this, additional granulation or coating steps are required. For this purpose, solutions or melts are brought into contact with solid particles. Evaporation of the solvent or cooling of the liquid causes the components to solidify on the particles.

In addition to product design, unintentional layer formation from solutions occurs during fouling processes in heat exchangers. Due to dissolved substances in relatively high amounts and temperature gradients on the wall surfaces, crystal layer formation can occur there. This results in undesirable heat transfer limitations.

Prediction of the resulting solid composition from crystallizing electrolytic solutions is rarely discussed in literature. Some work report on in-situ coating processes that produce a desired surface composition. This makes it possible to coat an active ingredient with a different component in a single process step.

The aim of this thesis is to provide the reader with a guide to solve crystallization problems of solutions containing several components. It should be applicable to suspension crystallization, product design of granules and thin crystalline films. Related fields such as geology, mineralogy, and alloy research may also benefit from the results.

From a theoretical examination, three groups of are identified for investigation: Phase equilibria, crystal growth kinetics of multiple components and supersaturation rate. The model system Na_2SO_4-Na_2CO_3-H_2O is used for its investigation. In a first step, phase equilibria and metastable zones of systems containing multiple components have to be investigated. The determination of phase equilibria is already well known but metastable zones are difficult to obtain. Homogeneous nucleation is not identified as an influencing factor on layer formation. However, its determination is nevertheless necessary for the investigation and evaluation of heterogeneous and secondary nucleation. A new pseudo-binary approach is used to investigate the metastable zone limit of a ternary system. It proves to be functional, but verification by isothermal evaporation experiments did not lead to the determined limits. Metastable zones of secondary nucleation were very close to the equilibrium state of both materials. Even at very low supersaturations, both electrolytes form new nuclei. This will be taken into account in the development of further experimental methods in this work.

To investigate crystal growth kinetics of various materials from highly saturated solutions, a new method is developed and established. The transient desupersaturation of a thin liquid film in contact with a crystalline substrate is measured. In the experiments, two cases of multi-component crystallization are found. In most cases, simultaneous crystallization of the two salts used is observed. In a few experiments, preferential crystallization of a single component occurs.

The influence of the supersaturation rate on the layer build-up is supposed to be important, as a fast supersaturation build-up could lead to simultaneous crystallization of all components. Slower supersaturation formation could favor one component to crystallize while another component remains in solution. However, experiments show that the effect on the solid composition is not strong.

The findings let to the conclusion that multi-component crystallization from solution on a crystalline substrate provokes a stratified surface. But it depends mostly on phase equilibrium behavior and on the concurrent crystallization kinetics.

A simulation model is created for the mathematical prediction of solid compositions, but its results deviate from the experimental results of layer formation. The deviations result from the lack of mathematical consideration of porosity and metastability behavior. Nevertheless, the qualitative trends are recognizable.

Finally, a strategy on multi-component crystallization can be deduced, which can either be used for product design of particles or other related processes with multiple components dissolved in solution.

Contents

Nomenclature

Acronyms

ATR-FTIR	Attenuated total reflection - fourier transformed infrared spectroscopy
API	Active pharmaceutical ingredient
BCF	Burton, Cabrera, and Frank
CCD	Charge coupled device
IR	Infrared
MSZL	Metastable zone limit
NC	Numerical control
NMR	Nuclear magnetic resonance
RSD	Residual standard deviation
USGS	United States Geological Survey
VDI	Verein Deutscher Ingenieure

Constants

π	Archimedes constant: 3.14159
R	gas constant: 8.31446 (J mol^{-1} K^{-1})
k	Boltzmann constant: $1.38065 \cdot 10^{-23}$ (J K^{-1})
N_A	Avogadro constant: $6.02214 \cdot 10^{23}$ (mol^{-1})

Latin symbols

A	component A
A	area (m^2)
a	empirical factor (-)
a	side length of unity cell (Å)
a_0	side length of reference unity cell (Å)
a_i	activity of component *i* (-)
a_i^*	activity of component *i* in equilibrium (-)
B	component B
b	side length of unity cell (Å)
b	empirical factor (-)
b_i	molality of component *i* (mol kg^{-1})
b_i^*	molality of component *i* in equilibrium (mol kg^{-1})
C	simulation cell in contact with solid
C	detector efficiency constant (-)
c	side length of unity cell (Å)
c^*	concentration in equilibrium (mol m^{-3})
$\bar{c}_i$	mean concentration of component *i* (mol m^{-3})
D	general diffusion coefficient (m^2 s^{-1})
$\mathbf{D}$	Fickian diffusion coefficient matrix (m^2 s^{-1})
D_i	self diffusion coefficient of component *i* (m^2 s^{-1})

D_{ij}	Fickian diffusion coefficient of component *i* with respect to component *j* (m^{2} s^{-1})
$D_{\mathrm{water,air}}$	diffusion coefficient of water in air (m s^{-1})
$D_{\mathrm{water,N_2}}$	diffusion coefficient of water in nitrogen (m s^{-1})
Đ_{ij}	Stefan-Maxwell diffusion coefficient of component *i* with respect to component *j* (m^{2} s^{-1})
$d_{50,0}$	median diameter related to number of particles (m)
d_h	hydraulic diameter (m)
d_j	jet diameter (m)
E	eutectic point
$\mathrm{E_{A\text{-}B}}$	eutectic point of binary system A and B
$\mathrm{E_{S\text{-}A}}$	eutectic point of binary system S and A
$\mathrm{E_{S\text{-}B}}$	eutectic point of binary system S and B
F	projection area of the detector hole on the volume of investigation (m^{2})
f_{het}	reduction factor for heterogeneous nucleation (-)
ΔG	excess free energy (J)
ΔG_A	excess surface free energy (J)
ΔG_V	excess volume free energy (J)
ΔG_v	free energy of phase transition (J)
g	crystallization order (-)
H	enthalpy (J)

H_0	initial distance of jet from liquid surface (m)
$h(t)$	time dependent liquid level (m)
h^*	dimensionless distance of jet (-)
$\Delta\tilde{h}_{v,\mathrm{water}}$	specific molar enthalpy of vaporization of water (J mol^{-1})
I_i	Raman intensity of species *i* (a.u.)
I_0	intensity of laser light (a.u.)
K_i	calibration constant of component *i* (-)
$k_{d,i}$	diffusion mass transfer coefficient (m s^{-1})
$k_{g,i}$	overall mass transfer coefficient (m^{3g-2} mol$^{-(g-1)}$ s^{-1})
$k_{g,i}^{'}$	internal mass transfer coefficient (m^{3g-2} mol$^{-(g-1)}$ s^{-1})
$k_{r,i}$	reaction/integration mass transfer coefficient (m^{3r-2} mol$^{-(r-1)}$ s^{-1})
L	length (m)
M	number of simulation cells
M^L	total mass in liquid phase (kg)
M_i^L	mass of component *i* in liquid phase (kg)
$\dot{M}$	mass flux (kg s^{-1})
$\dot{M}_i$	mass flux of component *i* (kg s^{-1})
$\tilde{M}$	molar mass (kg mol^{-1})
m	counter of simulation cells
$\dot{m}_{i,\mathrm{cryst}}$	specific crystallization mass flux of component *i* (kg m^{-2} s^{-1})
N_i	moles of component *i* (mol)

$\dot{N}_{\mathrm{dry}}$	molar drying flux (mol s^{-1})
n	number of samples (-)
$\dot{n}$	specific molar flux (mol m^{-2} s^{-1})
$\dot{n}_{i,\mathrm{cryst}}$	specific molar flux of crystallizing component *i* (mol m^{-2} s^{-1})
n_i	specific moles (mol m^{-2})
P	global eutectic point of ternary system
p	pressure (Pa)
p^*_{water}	vapor pressure of water (Pa)
$\dot{Q}$	heat flux (W)
r	radius of a sphere (m)
r	integration reaction order (-)
r^*	dimensionless radius of reactor (-)
S	solvent component S
S	saturation index (-)
s	length (m)
T	temperature (°C or K)
$\bar{T}$	caloric mean temperature (K)
T^*	saturation temperature (°C or K)
$T^{'}$	specific temperature (°C or K)
T_0	temperature at the surface of a body (K)
ΔT_{met}	metastable supercooling (K)

$\dot{T}$	cooling rate (K s^{-1})
V	volume (m^3)
$\dot{V}_{\mathrm{air}}$	volume flux of air (m^3 s^{-1})
v	velocity (m s^{-1})
v	growth rate (m s^{-1})
X_i	mass load of component *i* (kg kg^{-1})
$\hat{X}_i$	estimated mass load of component *i* (kg kg^{-1})
x_i	mass fraction of component *i* (kg kg^{-1})
$\tilde{x}_i$	molar fraction of component *i* (kg kg^{-1})
$\tilde{x}_{\mathrm{water,ph}}$	molar fraction of water in liquid at gas-liquid interface (mol mol^{-1})
$\Delta\tilde{x}_i$	molar fraction difference of component *i* (mol mol^{-1})
Δx_{met}	metastable supersaturation (kg kg^{-1})
$\dot{x}_i$	supersaturation rate (kg kg^{-1} s^{-1})
$\tilde{y}^{\infty}_{\mathrm{water}}$	molar fraction of water in gas phase (mol mol^{-1})
$\tilde{y}_{\mathrm{water,ph}}$	molar fraction of water in air at gas-liquid interface (mol mol^{-1})
z	length scale (m)

Greek symbols

α	angle of unity cell (°)
α	volume fraction of liquid (-)
α_{int}	internal heat transfer coefficient (W m^{-2} K^{-1})

β	angle of unity cell (°)
$\beta_{\mathrm{water,air}}$	mass transfer coefficient of water in air (m s^{-1})
$\beta_{\mathrm{water,N_2}}$	mass transfer coefficient of water in nitrogen (m s^{-1})
γ	angle of unity cell (°)
γ	surface tension (N m^{-1})
$\Delta_{v_{\mathrm{air}}}$	molar volume of air (-)
$\Delta_{v_{\mathrm{water}}}$	molar volume of water (-)
δ	lattice mismatch factor (-)
δ_{ij}	auxiliary variable (-)
μ_i	chemical potential of component *i* (-)
μ_i^*	chemical potential of component *i* in equilibrium (-)
ν	number of moles forming one mole of electrolyte (-)
ν	kinematic viscosity (m^2 s^{-1})
ν_{air}	kinematic viscosity of air (m^2 s^{-1})
ρ	density (kg m^{-3})
ρ^S	solid density (kg m^{-3})
ρ^L_{water}	density of liquid water (kg m^{-3})
η^L_{water}	dynamic viscosity of water (Pa s)
$\tilde{\rho}^L$	molar density of liquid phase (mol m^{-3})
σ	(=($S-1$)) relative supersaturation (-)
φ_{air}	relative humidity in air (-)

λ	heat conductivity (W m^{-1} K^{-1})
$\Gamma_{i,j}$	thermodynamic correction factor (-)
γ_i	activity coefficient of component *i* (-)
γ_i^*	activity coefficient of component *i* in equilibrium (-)
ξ_i	mass fraction of electrolytes in resulting solid material (kg kg^{-1})
Ω_{obs}	observation angle of the objective (°)
$\frac{\partial\sigma_i}{\partial\Omega}$	differential scattering cross area (-)

Operators

Δa	gradient of a
$\vec{a}$	vector
$\mathbf{A}$	matrix

Subscripts

0	boundary
1	index for component 1
2	index for component 2
3	index for component 3
A	per unit area
A	index for component A
B	index for component B
bulk	bulk volume
C	cell in contact with solid

char	characteristic
c	center
cool	cooling
crit	critical
cryst	crystallizing
cs	cross section
d	related to diffusion
dry	drying
g	related to overall crystal growth
h	hydraulic
het	heterogeneous
I	interface of adsorption layer
i	index for component *i*
init	initial
int	internal
j	index for component *j*
l	large
met	metastable
obs	observation
ph	phase boundary
r	related to reaction

ref	reference
S	index for solvent S
S	position S
s	small
th	theoretical
V	per unit volume

Superscripts

L	liquid phase
S	solid phase
∞	at great distance from phase boundary
*	saturated

Dimensionless numbers

$Bi = k_{g,i} \cdot L_{\mathrm{char}}/D$	Biot number
$Gr = g \cdot L_c^3 \cdot \Delta\rho/(\nu \cdot \rho^{\infty})$	Grashof number
$Nu = \alpha_{int} \cdot L_c/\lambda$	Nusselt number
$Pe = L_c \cdot v/D$	Péclet number
$Ra = Gr \cdot Sc$	Rayleigh number
$Re = v \cdot L_c/\nu$	Rayleigh number
$Sc = \nu/D$	Schmidt number
$Sh = \beta \cdot L_{\mathrm{char}}/D$	Sherwood number
$\bar{\theta} = \frac{\bar{T}-T_0}{T_1-T_0}$	dimensionless caloric mean temperature

$\bar{\theta} = \frac{T_c - T_0}{T_1 - T_0}$	dimensionless center temperature
$\tau = \kappa t / X^2$	dimensionless time

1 Crystallization of multi-component films

Solid surfaces composed of multiple crystalline components are widely used in product design. In the pharmaceutical industry, tablets shall contain multiple active pharmaceutical ingredients (API) that exert their respective effects at specific times [Ummadi et al., 2013; Suresh et al., 2017; Seo and Han, 2019]. If time-delayed drug release is favored, a coating layer is commonly used to provide a respective time lag [Sousa et al., 2002; Römbach and Ulrich, 2007; Xuan et al., 2020; Seo et al., 2020]. Such coating layers are applied in supplementary process steps, which require additional equipment and time. Similar requirements are placed on granules produced in the pharmaceutical industry but also in the agricultural industry. Fertilizers should release their ingredients at a distinct time or depending on the actual weather [Kochba et al., 1990; Lawrencia et al., 2021; Fu et al., 2018]. For this, it is necessary to adjust not only the material distribution but also their properties such as dissolution rate [Shaviv, 2001; Beig et al., 2020].

Imaginable process techniques of both product groups would be every kind of granulator or coating device, which are both similar in principle [Walker et al., 2000; Degrève et al., 2006; Suresh et al., 2017; Lawrencia et al., 2021]. A fluid containing dissolved or molten materials is brought in contact with solid particles. Through evaporation of solvent or cooling of the fluid, components solidify onto the original particles. That lets them grow until a desired size is reached. Schematic drawings of these processes are shown in Figure 1.1.

Granulation and coating have in common that a fluid containing solidifying components is deposited onto a solid surface. While coating processes aim to produce complete surface covers, granulation processes could result in partially covered particles.

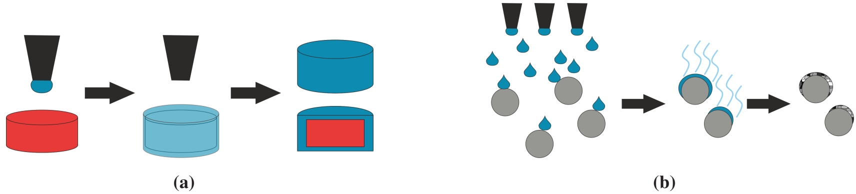

Figure 1.1: Schematic depictions of tablet coating (a) and granulation (b) processes.

Often, a certain material distribution is desired. For example, active film coating involves the application of API in multi-component aqueous solutions coated onto a substrate, e.g. a tablet. The final API distribution and the physicochemical properties shall be uniform in the top layer [Seo et al., 2020]. Often, coating steps are repeated with different materials to achieve material distribution rather than applying a multi-component solution that builds up layers itself [Kim et al., 2012]. Additives for coating processes are chosen with respect to their influence on thermodynamic and physicochemical properties [Seo et al., 2020; Beig et al., 2020; Lawrencia et al., 2021]. Polymorphic and solvate states of crystallizing components are also of great interest, as these result in altered properties such as crystal structure, solubility or density [Higashi et al., 2017].

Besides product design, unintended layer formation from solutions takes place during fouling processes in heat exchangers [Al-Gailani et al., 2020; Song et al., 2019; Lv et al., 2020]. Due to dissolved material in rather high amounts and temperature gradients at wall surfaces, crystallization of multiple components takes place. Hence, undesired heat transfer limitations occur. Also, material separation from melts can be related to this topic. The build-up of crystalline layers and impurity distribution deposited at surfaces depend on the process conditions such as temperature and composition of initial fluids [Parisi and Chianese, 2001; Jiang et al., 2014; Yazdanpanah et al., 2016]. In order to predict impurity integration or even produce pure layers, crystallization kinetics have to be investigated in more detail [Jiang et al., 2014].

1.1 State of the art

All application examples in Chapter 1 have in common that their final solid assemblages are of great interest. Multiple components dissolved in solutions (e.g., aqueous) are applied intentionally or non-intentionally on substrate materials such as tablets or tubing surfaces. Crystallization behavior in general and especially layer build-up from multi-component solutions are functions of phase equilibria, crystallization kinetics, and process conditions [Ulrich and Frohberg, 2013]. In order to produce a desired product or to describe material distributions, all have to be considered.

Phase equilibria, especially of electrolytic solutions, have been well investigated in the past [Jänecke, 1906; Caspari, 1924]. With thermodynamic activity models such as Pitzer, e-NRTL or UNIQUAC, it is possible to calculate the temperature dependent solubilities as well as stable solid states [Pabalan and Pitzer, 1987; Thomsen et al., 1996; Hingerl et al., 2014; Bhattacharia et al., 2015]. All these models depend on already existing experimental data. However, strategies for experimental determination of phase equilibria of new material systems are well established [Mullin, 2001]. For process design, metastable states are of great interest [Mersmann, 2001]. They are related to phase equilibria and often pictured together in phase diagrams. Also in product design, metastable states of the solution, but also of metastable solid forms, are of great importance for the final product [Kim and Ulrich, 2003; Ulrich and Frohberg, 2013; Jiang et al., 2014; Pawar et al., 2021; Urwin et al., 2021]. It is well known that additives or even impurities have a strong impact on metastable zones and solid states [Sangwal, 2009, 2010, 2011; Titiz-Sargut and Ulrich, 2002; Ulrich and Frohberg, 2013; Schmidt et al., 2013]. However, the determination of metastable zones of multiple components is not discussed to a great extent. Most of the investigations focus on the variation of metastable zone limits of one material influenced by a minor impurity. There is a lack of studies and strategies on metastability of multi-component systems with at least two equal crystallizing materials.

The influence of additives on metastable states can be related to influences on nucleation kinetics. In addition, crystal growth kinetics can be influenced by other materials. Again, some works focus on influences of minor additives on crystallization behavior of single materials [van der Leeden et al., 1989; Rauls et al., 2000; Kubota, 2001]. Furthermore, incorporation of impurities are discussed often [Jiang et al., 2014; Borsos et al., 2016; Darmali et al., 2018]. However, the concentrations of these foreign components are mostly very low. At higher concentrations, stronger impacts on crystallization behavior can be expected. Zago et al. [2020] and Penha et al. [2021] investigated simultaneous solidification of two species in a suspension crystallizer. They could observe that both components crystallized independently as own particles or grew on each other. From this, it can be gathered that crystallization behavior of multiple components are difficult to characterize.

Simultaneous crystallization of several components is defined as co-crystallization. The resulting formation is either a solid solution with several entities within the crystal lattice or a mixture of crystals. In pharmaceutical research, many efforts are made with respect to co-crystallization from solution. These allow the adjustment of physicochemical properties such as dissolution rate or solubility [Pawar et al., 2021]. Since co-crystallization takes place from multi-component solutions, it is necessary to investigate phase transition kinetics of single crystals as well as of co-crystals. With the knowledge of phase equilibria and transition kinetics, the production process can be designed to obtain the desired product, e.g. a specific co-crystal. In slurry crystallization processes, particles of either entity are put in solution to produce co-crystals [Sanjay et al., 2014]. Hence, growth and nucleation with respect to the process conditions have to be determined [Sun, 2013]. Even though many works focus on this topic, nucleation and growth kinetics are still lacking [Pawar et al., 2021]. Also, there are only a few papers on determination of thermodynamic behavior in phase diagrams of co-crystallization processes [Cruz-Cabeza et al., 2008; Shemchuk et al., 2020; Yu et al., 2021].

Not many studies exist that offer a view on layer build-up in product design by crystallization. Römbach and Ulrich [2007] or Katona et al. [2016] report on in-situ coating processes, which create distinct surface assemblages. With these, it is possible to coat an active ingredient in a single process step. But general methods for predicting final solid layer assemblages for electrolytic solutions are still lacking.

In contrast, layer build-up from multiple components has been investigated to a greater extent for colloidal systems [Routh, 2013; Schulz and Keddie, 2018]. In Figure 1.2, four imaginable solid layer assemblages are displayed.

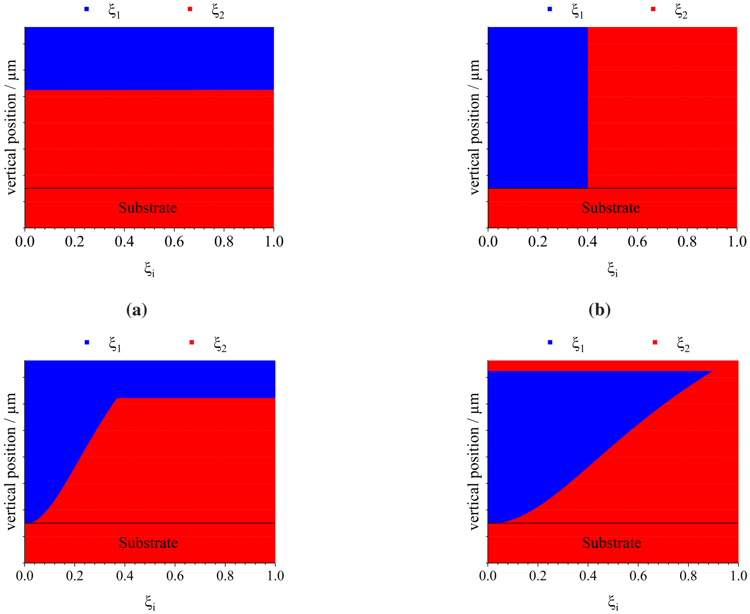

(a) (b) (c) (d)

Figure 1.2: Imaginable solid layer assemblages of two components on a single component substrate. (**a**): Total material separation with a pure top layer. (**b**): Uniform distribution of both components. (**c**): Stratification of both components with a steady increment. (**d**): Similarly, foreign component content increases over solid height but with a higher increment. The top layer is made of substrate material.

All examples have in common that the overall material composition is equal. Above the substrate (black line), component 1 makes up 40% and component 2 60%. In Diagram (a), a total phase separation between both components is displayed. This corresponds to the aforementioned in-situ coating. In this case, the substrate component 2 solidified first and the top layer consists of pure foreign component 1. In contrast, a homogeneous solid layer is depicted in Diagram (b).

Both components are present with a constant concentration above the substrate. Diagrams (c) and (d) represent a steady increment in foreign component. In case (c), foreign component 1 increases slower than in case (d). At a certain point, no more substrate material is left in solution. Hence, the upper layer is made of pure component 1. On the contrary, a pure layer of substrate component 2 is expected in case (d) due to the higher increment of component 1. Hence, this process can be described with an encapsulation of component 1.

The layer build-up of colloidal systems results from drying processes of solutions containing one or more types of colloidal particles [Routh, 2013]. Trueman et al. [2012] found the Péclet number to be a pragmatic marker to predict the solid layer assemblage. The Péclet number defines the relation between advective and diffusive fluxes. In the case of colloids, the advective term would be the phase change of the solvent from liquid to gas. The diffusive term refers to the movement of particles in solution. They adapted the evaporation so that the Péclet number of smaller and larger particles were smaller or greater unity, respectively ($Pe_s < 1 < Pe_l$). By meeting this criterion, they observed stratification. Others extended the decisive criterion, which will not be discussed further here [Schulz and Keddie, 2018].

In contrast to colloidal particles, electrolytic systems cannot be described by the theory of Trueman et al. [2012]. Due to the crystallization process at the solid-liquid interface, there is an additional advective flux. This would change the Péclet number. Additionally, the involved components may have different crystallization kinetics. Having a faster and a slower crystallizing component in solution would result in high fractions of the faster material in early stages of solidification. Due to the faster growth, this component would diminish its solution concentration faster than the other material. Finally, the layers developing later would be mostly made of the slower material. Hence, a stratified layer would arise only by differences in phase transfer kinetics. As a result, the theory from colloidal particle film formation cannot be applied to electrolytic systems but a broader investigation of phase equilibria and kinetics is necessary. Therefore, the description of layer build-up of electrolytic systems has to be developed as a funciton of its phase equilibria and crystallization kinetics. At first, these two points shall be investigated. Out of the results, further points may arise.

1.2 Research hypotheses

The above stated shortage in investigations of layer build-up from multi-component solutions leads to the principal research hypothesis (Hypothesis I) of this work:

Multi-component crystallization from solution on crystalline substrates provokes a stratified surface.

Dependent on phase equilibria of the involved components and differences in their crystallization kinetics a natural layering may occur. This may also depend on the speed of supersaturation build-up. In Figure 1.3, the hypothesis is sketched with its relation to influencing parameters, which were elaborated in the previous section.

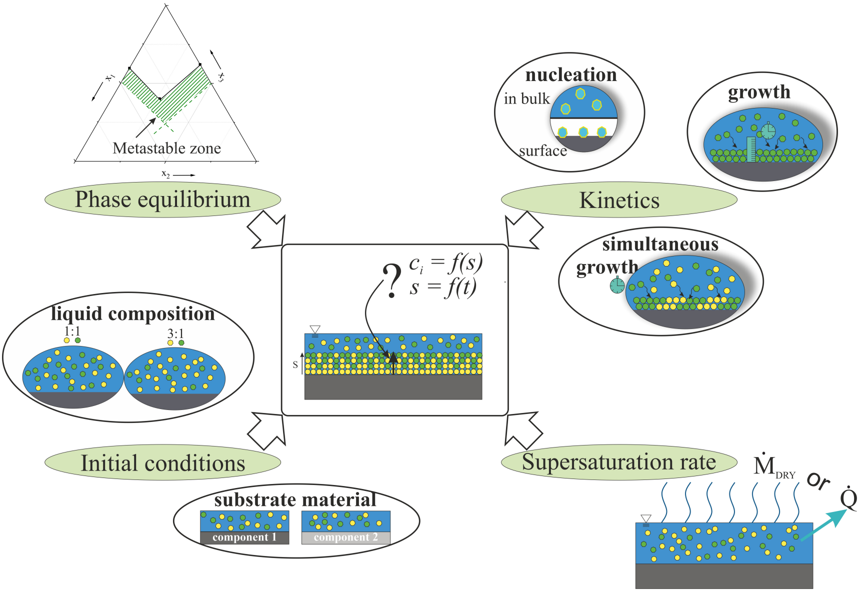

Figure 1.3: Overview and connection of the research hypotheses. The final layer distribution is influenced by four main factors: phase equilibrium, supersaturation rate, kinetics, and initial conditions. All factors are divided into sub-factors.

The solid assemblage resulting from multi-component crystallization on a substrate is dependent on the phase equilibrium, crystallization kinetics, supersaturation rate, and initial conditions. In order to investigate the impact of each, new methods are necessary. By defining the most relevant impact factors, the development of stratified surfaces from multi-component electrolytic systems can be predicted and transferred to other material systems.

First, experiments for determination of phase equilibria of multiple components are well known. To display the phase behavior, triangular diagrams are often used. On the top left, an example of a simple ternary system consisting of a solvent and two dissolved materials is depicted. The solubility line (black) separates the states of clear solution and solid build-up. The eutectic point is located at the intersection of both solubility lines. Below the eutectic point, a crystal mixture of both components is formed. But metastable zones (plotted in green) of these systems are difficult to determine. For binary systems, two methods exist - isothermal and polythermal method [Mullin, 2001]. Many samples of solutions over the solubility range have to be investigated to get robust results. Adding another component multiplies the number of samples to be evaluated. This would result in time-consuming investigations. To reduce evaluation time, it is hypothesized that:

Metastable zones of ternary systems can be predicted by a pseudo-binary approach (Hypothesis II).

Pseudo-binary means that the concentration of one component is treated as an additive while the other component is able to crystallize. With polythermal experiments of several saturated solutions, crystallization events are observed and correlated with theoretical considerations into metastable zones in ternary diagrams. The impact of metastable zones on stratification are easy to imagine. Inside the metastable zone, spontaneous phase transition is not probable. If another component solidifies to this point, the first solid layers would consist only of this component. Due to that, the component not yet crystallized would supersaturate further. Once crossing the metastable limit, nucleation and hence, growth are possible. The final solid would be stratified.

As previously mentioned, the kinetics are important for the eventual distribution of the components besides phase equilibria. If nuclei of one component are formed faster or the growth rate is high at low supersaturation, this component would be the main material in early solid layers. The other component would accumulate in the solution and subsequently solidify. In this work, the focus is laid on crystal growth onto a substrate. Nucleation is not discussed in greater detail. Added components will be treated as if they would grow onto the substrate. In the existing literature, there are no studies investigating simultaneous crystallization of multiple components nor kinetics in the presence of a high amounts of additives. This leads to Hypothesis III:

Kinetics of multiple crystallizing materials can be measured simultaneously and independently.

Since kinetics depend explicitly on supersaturation, the rate of supersaturation may be crucial for the final solid assemblage. Supersaturation can be generated by reducing the fraction of a solvent or by subcooling if the solubility is a function of temperature. The two ways are depicted on the lower right in Figure 1.3. An important process parameter in process design of crystallization processes is the supersaturation rate. Hence, Hypothesis IV is stated as:

The rate of supersaturation build-up has an impact on the final layer assemblage.

A fast supersaturation rate would lead to a mostly uniform layer because a high supersaturation is reached early. Hence, all materials could build nuclei or grow fast. In contrast, a low supersaturation rate would favor fast crystallizing materials. Other materials would crystallize later because their kinetics are more dependent on supersaturation. Finally, the initial conditions may influence the layer formation. The liquid composition and the provided substrate have an effect on the kinetics. A possibility to investigate the influence of those parameters is the analysis of solid assemblages after crystallization process. This approach is inspired by geological formation analysis [Jakobsson and Moore, 1986].

Before experimental investigation, the principal hypothesis will be addressed in theoretical calculations in Chapter 3. The influencing parameters will be varied in case studies to show their impact. Afterwards, the model material system sodium sulfate, sodium carbonate, and water will be investigated to answer the hypotheses I to IV. The system is chosen because of its well investigated phase diagram [Caspari, 1924]. With the software PhreeqC and its database

FREZCHEM, it is possible to calculate the phase equilibria at temperatures lower than 25°C [Marion et al., 2010; Toner and Sletten, 2013]. Up to this temperature, the phase diagram shows a rather simple behavior. Both electrolytes solidify as decahydrates. No other solid enitities are reported up to a temperature of 30°C [Caspari, 1924]. Hence, just one eutectic point exists at isothermal conditions. There is quite some practical relevance to this system as it is also used as model system for investigations regarding material recovery from waste waters [Karlsson et al., 2013; Shi and Rousseau, 2001; Shi et al., 2003; Bayuadri et al., 2006; Gourdon et al., 2010].

This work shall provide the reader a guidance for crystallization problems of solutions containing multiple components at rather high contents. Through connecting all influencing parameters, it shall be applicable to suspension crystallization, product design of granules, and thin crystalline layers. Also, related fields like geology, mineralogy, or alloy research may benefit from the results.

2 Theoretical background

As was stated before, layer formation from multi-component solutions depends on the phase equilibrium of material systems, solidification kinetics and the build-up of supersaturation. Mass transfer from liquid to solid can be described with the mechanisms nucleation and growth. The driving force for phase change from liquid to solid is characterized by the deviation from the actual to equilibrium chemical potential of the crystallizing component (compare Equation 2.1).

$$\Delta\mu_i = \mu_i - \mu_i^* = \tilde{R} \cdot T \cdot \ln\left(\frac{a_i}{a_i^*}\right) = \tilde{R} \cdot T \cdot \ln\left(\frac{\gamma_i \cdot b_i}{\gamma_i^* \cdot b_i^*}\right) \tag{2.1}$$

The difference in chemical potential depends on the temperature T, and the activities of component *i* at the actual a_i and equilibrium state a_i^*. The fraction of activities is known as saturation S. The activity may be described by the activity coefficient γ_i and molality b_i. If ideality prevails, activity coefficients have the value one. Then, supersaturation can be defined as the ratio of molalities or concentrations. The addition of other components changes the system and in particular influences the activity coefficients. In addition, other stable solid states are possible which in turn would change the equilibrium activity. The addition of other materials does not only change equilibrium states but also phase transition kinetics. Not only diffusion of ions is influenced by other entities in the liquid but also incorporation in the crystal lattice can be hindered or improved.

Phase transition in general and influences of other materials will be discussed in Section 2.1. Phase equilibria and metastable states, especially of multi-component systems, are highlighted in Section 2.2. Diffusion processes will be covered separately in Section 2.3.

To obtain supersaturation, two obvious ways arise from Equation 2.1. The first is changing temperature if the material system's equilibrium is temperature dependent. The molality b_i would stay constant whereas equilibrium molality b_i^* changes. The process pathway is depicted as a blue arrow in Figure 2.1.

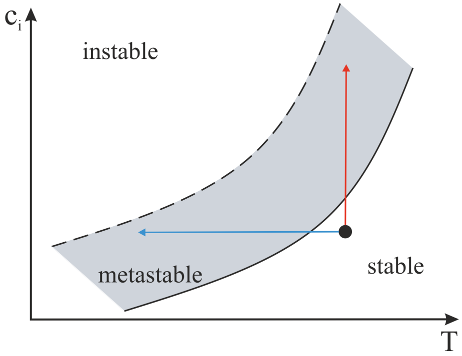

Figure 2.1: Solubility curve of component *i* in a binary system. Beneath the solubility line (full line), a solution is stable. Above the metastable zone limit (dashed line), a solution is instable and would build solid material immediately. The grey zone represents the metastable zone.

In addition, a decrease in solvent mass fraction through evaporation or drying would supersaturate a solution (compare Figure 2.1). Here, equilibrium activity remains constant and the actual activity changes. The pathway is represented by the red arrow. The supersaturated state is divided into two areas. The instable state indicates conditions when spontaneous phase transitions occur. The metastable state is dependent on process parameters such as stirring speed or supersaturation rate. At these conditions, spontaneous solidification does not emerge in reasonable time periods. It will be addressed in more detail in Section 2.2.

A cooling process is rather easy to picture. The solution to crystallize is cooled down by a cooling medium or through contact cooling. Evaporation or drying processes can be executed in very different ways. In Appendix A.1, the basic theoretical considerations for a drying channel process will be laid.

2.1 Nucleation and crystal growth

The molecular constituents of crystalline solids have a short- and long-range order. They are described by elementary cells, which have distinctive lattice lengths a, b, c and angles α, β, γ. Crystals of a material are built or grow in a distinct crystal system. All crystal systems are listed in Table 2.1 with their parameters of the elementary cell.

Table 2.1: List of crystal systems and their elementary cell parameters.

crystal system	**base vectors**	**angles**
cubic	$a = b = c$	$\alpha = \beta = \gamma = 90°$
hexagonal	$a = b \neq c$	$\alpha = \beta = 90°, \gamma = 120°$
monoclinic	$a \neq b \neq c$	$\alpha = \beta = 90°, \gamma \neq 90°$
orthorombic	$a \neq b \neq c$	$\alpha = \beta = \gamma = 90°$
rhomboedral	$a = b = c$	$\alpha = \beta = \gamma \neq 90°$
tetragonal	$a = b \neq c$	$\alpha = \beta = \gamma = 90°$
tricline	$a \neq b \neq c$	$\alpha \neq \beta \neq \gamma \neq 90°$

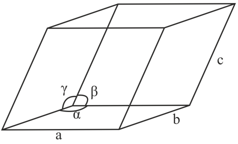

Nucleation and crystal growth are explained roughly in the following subsections. Furthermore, the influence of multiple components on both will be addressed.

Nucleation

In order to build a new crystal, an energy barrier has to be overcome. In a clear solution, particles have to be built from dissolved material. This mechanism is called primary homogeneous nucleation. In addition, primary heterogeneous nucleation and secondary nucleation are defined (compare Figure 2.2).

Heterogeneous nucleation requires other entities in solution such as particles, surfaces or bubbles. Secondary nucleation is defined as the build-up of new crystals in the presence of own particles.

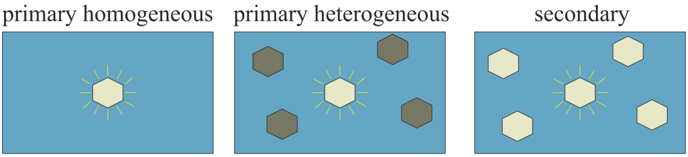

Figure 2.2: Schematic illustration of all nucleation mechanisms. Primary homogeneous nucleation generates new particles from clear solutions. From heterogeneous nucleation, new particles are formed in the presence of other solid materials. If solid material of the nucleating substance is present it is termed secondary nucleation.

From classical nucleation theory developed by Volmer [1939], the stability of a nucleus is dependent on the excess volume free energy ΔG_V and the excess surface free energy ΔG_A. In Equations 2.2a and 2.2b, both dependencies for homogeneous nucleation are demonstrated for a spherical nucleus. The sum of both is the overall excess free energy (Equation 2.2c).

$$\Delta G_V = \frac{4}{3}\pi r^3 \Delta G_v \tag{2.2a}$$

$$\Delta G_A = 4\pi r^2 \gamma \tag{2.2b}$$

$$\Delta G = \Delta G_V + \Delta G_A \tag{2.2c}$$

Both free energies are dependent on the nucleus size r. ΔG_v represents the change in free energy of the phase transformation per unit volume. Additionally, ΔG_A is a function of the surface tension γ between the crystal and the solution. In Figure 2.3, both energies and their sum ΔG are shown as a function of nucleus size r.

Up to the maximum of ΔG, nuclei are not able to grow but redissolve. By reaching the critical size, nuclei are stable and build a solid phase. The differentiation of Equation 2.2c $\frac{d\Delta G}{dr} = 0$ yields Equation 2.3.

$$\frac{d\Delta G}{dr} = 8\pi r\gamma + 4\pi r^2 \Delta G_v = 0 \tag{2.3}$$

Transposed to the radius, Equation 2.4 defines the critical radius of a nucleus.

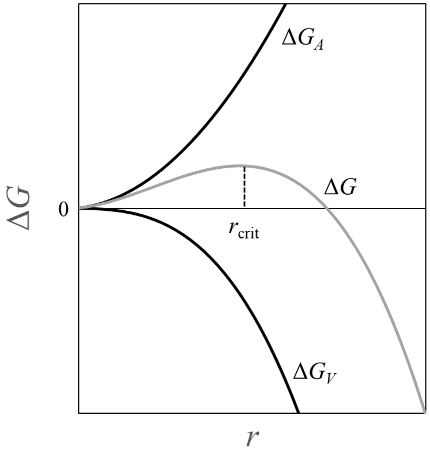

Figure 2.3: Evolution of free surface energy ΔG_A, free volume energy ΔG_V and the sum ΔG are depicted as a function of nucleus size r. The maximum of ΔG marks the point from which a nucleus is stable.

$$r_{\text{crit}} = -\frac{2\gamma}{\Delta G_v} \tag{2.4}$$

Applying the Gibbs-Thomson relation for ideal solutions, the critical supersaturation S_{crit} can be expressed as a function of r (compare Equation 2.5) [Mullin, 2001].

$$\ln\left(\frac{c(r)}{c^*}\right) = \ln(S_{\text{crit}}) = -\frac{2\tilde{M}\gamma}{\nu RT\rho r} \tag{2.5}$$

Apart from the radius, the critical supersaturation depends on molar mass $\tilde{M}$, surface tension γ, number of moles building one mole of an electrolyte ν, ideal gas constant R, temperature T, and solid density ρ in the liquid. Inserting Equations 2.4 and 2.5 in Equation 2.2c results in the critical excess free energy ΔG_{crit} to build a growable nucleus.

$$\Delta G_{\text{crit}} = \frac{16\pi\gamma^3}{3\left(\frac{\nu RT\rho}{\tilde{M}}\ln(S)\right)^2} \tag{2.6}$$

The rate of building nuclei can be described with the Arrhenius equation. Taking Equation 2.6 as free energy, results in Equation 2.7.

$$J = A \cdot \exp\left(-\frac{\Delta G_{\text{crit}}}{kT}\right) \tag{2.7}$$

Hence, nucleation rate is strongly dependent on supersaturation, temperature and surface tension. The derived equation is valid for nucleation processes in clear solutions. For heterogeneous nucleation, critical excess free energy changes to Equation 2.8.

$$\Delta G_{\text{crit}}^{'} = f_{\text{het}} \cdot \Delta G_{\text{crit}} \tag{2.8}$$

The factor f_{het} has a value of less than one and reduces the energy barrier. Other components suspended as particles or present as surfaces could activate nucleation. Also, gas bubbles or other "foreign" impacts belong to this class of nucleation. The influence of different lattice parameters of seed particles on the nucleation probability was investigated [Telkes, 1952; Tóth et al., 2012; Fan, 2013; Belyakov and Gourlay, 2014]. The lattice mismatch is defined with Equation 2.9.

$$\delta = \frac{a - a_{\text{ref}}}{a_{\text{ref}}} \tag{2.9}$$

If the deviation of lattice parameters δ is small, the probability of nucleation increases. Not only the lattice match was found to be relevant but also chemical functionality has to be similar [Chadwick et al., 2011].

The probability of nucleation increases further if particles of the crystallizing material are already present. Secondary nucleation can be divided into two possible cases. First, contact nucleation in agitated vessels leads to abrasion of suspended particles in micro and macro scale. Hence, new particles are not formed out of dissolved material but through breakage of already existing solids. In contrast, new particles may originate out of solution in the presence of a seeding particle. This is called seeding nucleation. There are only few theories how the presence of a crystal initiates nucleation. Cui and Myerson [2014] investigated nucleation of glycine in water. They concluded from their experiments that clusters should be formed in the interface layer at the solid surface or originate from the particle itself as micro-particles. Similar theories were raised by Qian and Botsaris [1997] as "embryo coagulation secondary nucleation", Garside and Davey [1980], and Tai et al. [1992]. In other studies, chiral components or polymorphism were investigated [Qian and Botsaris, 1998]. By seeding with a specific enantiomer or polymorph, it was possible to produce nuclei of the same species [Lorenz et al., 2006; Xu et al., 2020].

Nucleation probabilities of the three mechanisms come along with metastable states. The explanations of metastability in Section 2.2 require the considerations from this section.

Crystal growth

Existing crystals or nuclei are able to grow in a supersaturated solution. Even small supersaturation is sufficient to drive the growth process. Besides supersaturation, growth is dependent on the crystal faces, defects on the molecular and macroscopic level, and additives [Mullin, 2001]. Imperfections could be point defects in the crystal lattice up to pores in crystalline layers. Additives may have a positive or negative effect on the growth of one component. Surface adsorption can hinder the crystallization completely whereas the presence of another component improves crystallization. In Figure 2.4, some of the previous mechanisms are displayed.

With examples I - III, integration at three microscopic positions are shown. First (I), integration at a surface vacancy is energetically the most favorable. Second (II), the integration at a kink is shown. Lastly, the energetically worst case from microscopic point of view is at a free surface (III). In addition, surface adsorption (IV) - in this case of anions - hinders the integration of a species. In addition to microscopic influences at the surface, macroscopic scratches favor crystal growth at these positions.

To describe crystal growth, there are many theories in literature. Some of them are shortly presented. Based on a theory by Volmer [1939], the adsorption layer

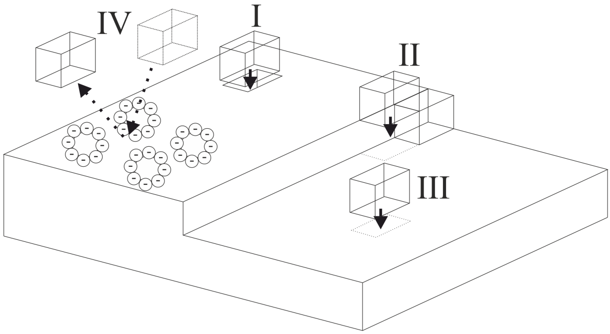

Figure 2.4: Schematic drawing of integration in the crystal lattice and of several influencing factors.

theory was developed to describe the growth as a step-wise build-up of crystal layers. A new layer would only be built if the lower layer was fully occupied. The theory was enhanced by Kossel [1927] and Burton et al. [1951] (BCF theory). The latter theory takes into account that growth rate is proportional to the square of supersaturation at low supersaturation. At higher values the relation is linear. However, the theory was developed for crystal growth from vapors which limits its adequacy to describe growth from solution. The polynuclear model assumes that first, nuclei have to be built on a crystal surface which grow laterally afterwards. After growth of a sufficient area, new nuclei can be formed on them. The diffusion-reaction theory is a more pragmatic way to describe the growth process [Mullin, 2001]. In its easiest form, it is a two-step process divided into a diffusion and a reaction step. First, it was proposed by Berthoud [1912] and Valeton [1924]. In fact, several more steps should be taken into account such as ion dehydration or surface diffusion. However, many effects such as layer growth or facetting of crystals cannot be described by the theory. Many of those theories are specific to growth sites, e.g. faces of the crystal.

Because layer formation on crystalline substrates is examined in this research study, a more general approach is required to describe growth. Hence, an overall crystal growth kinetic is desirable. Diffusion-reaction theory makes it easy to obtain a mass flux onto a growth area. The mass transfer is split up into two - diffusion and reaction - steps. Figure 2.5 illustrates the theory.

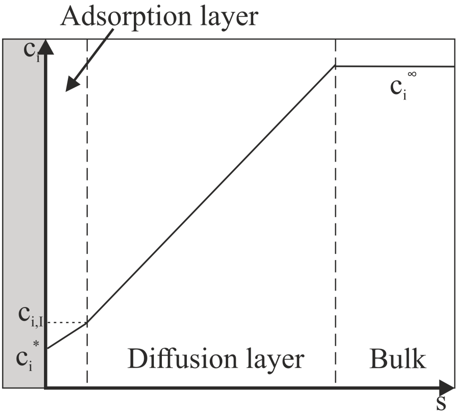

Figure 2.5: Schematic depiction of diffusion-reaction-theory. Concentration of crystallizing component i is a function of position s with respect to the crystal (grey rectangle). At the solid-liquid interface a constant equilibrium concentration of c_i^* is assumed. The integration takes place in the virtual adsorption layer. The interfacial concentration $c_{i,I}$ at the boundary to diffusion layer has to be determined theoretically. In the bulk phase a constant concentration c_i^∞ is given.

A virtual adsorption layer is imagined in the vicinity of the crystal surface. At the solid-liquid interface equilibrium concentration c_i^* is assumed. The adsorption layer stays in contact with a diffusion layer. The interfacial concentration is $c_{i,I}$, a theoretical value which is experimentally not possible to determine. In the bulk of the solution, a constant concentration c_i^∞ is reached. The inclination of concentrations in the adsorption and diffusion layer depends on mass transfer coefficients. Equations 2.10a - 2.10c show the dependency of mass flux from concentrations in the solution.

$$\dot{n}_i = k_{d,i} \cdot (c_i - c_{i,I}) \tag{2.10a}$$

$$\dot{n}_i = k_{r,i} \cdot (c_{i,I} - c_i^*)^r \tag{2.10b}$$

$$\dot{n}_i = k_{g,i} \cdot (c_i - c_i^*)^g \tag{2.10c}$$

The first equation represents mass transfer through diffusion from the bulk to the interface. Concentration $c_{i,I}$ is a theoretical value and not easy to obtain.

Mostly, it is replaced by combining Equations 2.10a - 2.10b. The mass transfer coefficients for the diffusion step $k_{d,i}$, the reaction step $k_{r,i}$, and the overall kinetic $k_{g,i}$ have to be determined from experiments. The first is mostly determined by dissolution measurements. Also, it could be derived from heat-mass-transfer analogies which are introduced in Appendix A.2. The mass transfer coefficient $k_{g,i}$ can be obtained from crystallization experiments. Equation 2.11 shows the relationship of the three mass transfer coefficients if the exponents $g = r = 1$. The exponent r characterizes the order of the integration process and g of the overall crystallization process.

$$\frac{1}{k_{g,i}} = \frac{1}{k_{d,i}} + \frac{1}{k_{r,i}} \tag{2.11}$$

With this, $k_{r,i}$ can be calculated. The theory has its limitations because a real growth process cannot be described by only two consecutive steps [Nielsen, 1984].

Furthermore, the dissolution process is assumed to be diffusion-limited which is not always the case [Bovington and Jones, 1970]. Nevertheless, it gives the opportunity to describe effective mass transfer in a rather easy way.

Diffusion-reaction theory is a widely used approach to describe crystal growth. Also, impacts of additives were investigated deploying the theory [Offermann et al., 1995; Tait et al., 2009]. Especially foreign ions can greatly impact the growth process. They could impact greatly the growth process even at low concentrations [Nielsen et al., 2016; Vavouraki and Koutsoukos, 2016]. Already in ppm-scales, ions could suppress or decrease the growth rate. Furthermore, added components could lead to preferential growth of polymorphs or face sites [van der Leeden et al., 1989]. Looking on multiple crystallizing components, it is possible that an additive would hinder growth of one of the substances and enhance the other. Mostly, the hindrance is ascribed to surface adsorption [Mersmann, 2001]. Additionally, phase equilibrium or viscosity could be affected which influences supersaturation and diffusivity, respectively.

The method to be chosen for measuring crystal growth kinetics depends on its aim. There are three scales imaginable: First, a pragmatic overall kinetic of many crystals, for example in a suspension crystallizer. Second, single particle growth rate. Lastly, face-specific growth rates. The methods for the two last-mentioned scales have in common that mostly the change in size is measured. For in-line measurements, camera systems or interferometric techniques are used [Kanzaki et al., 1998; Borchert et al., 2014; Eder et al., 2015; Wu et al., 2016]. An important requirement for all measurement is the knowledge of the fluid composition and temperature [Garside et al., 2002]. It has to be ensured that it remains constant throughout the process. Also, fluid parameters such as flow velocity or stirring speed have to be held constant depending on the method.

Mean growth rates from experiments with multiple independent crystals such as suspension crystallizers or fluidized beds can be retrieved in two ways. First, it is possible to measure the particle size distribution change under a known supersaturation. Another way is a desupersaturation measurement. An initially supersaturated solution is brought in contact with solid material such as seed crystals in a suspension crystallizer at constant temperatures. The specific surface of solids has to be known. The change in composition is tracked analytically. Imaginable methods would be spectroscopic methods such as ATR-FTIR or Raman spectroscopy. Other than that, measurement of changes in refraction indices or density are possible. A principal assumption of this method is that no nucleation occurs. Hence, the change in concentration can only be related to the growth process. [Garside et al., 2002]

2.2 Phase equilibrium and metastability

Phase equilibria of dissolved components are commonly displayed in solubility diagrams. The solubility is dependent on the chemical potential of a substance as already introduced. The dissolvable amount of many materials is a function of temperature (compare Figure 2.1). In addition, a metastable zone is marked by the dashed line in the figure. It is important to notice that the experimentally determined metastable limits are no exact boundary in contrast to the solubility line. These depend on experimental conditions like cooling rate or stirring speed. Therefore, it is an estimate for spontaneous nucleation in a solution. At supersaturations exceeding this zone, a solution is instable and very probable to build nuclei. Within the zone, spontaneous nucleation is unlikely under specific process conditions. For investigation of metastable limits, two methods are known. Solutions with a known supersaturation can be examined isothermally. With this, the metastable supersaturation Δx_{met} can be determined. The induction times to build nuclei are detected and related to the prevailing supersaturation. The metastable limit can be defined as the maximum concentration at which no nucleation took place in a previously defined time span [Mullin, 2001]. Hence, this limit depends strongly on the definition of the time span. The other method is polythermal and results in measured supercoolings ΔT_{met}. A solution with a known composition and saturation temperature is subcooled with a constant cooling rate. The temperature at which nucleation takes place is the metastable subcooling temperature. A variation of cooling rates would result in different limits. Moreover, both methods depend on other parameters such as stirring speed or the volume of the reactor. Both Δx_{met} and ΔT_{met} can be related to each other with Equation 2.12 [Nyvlt, 1984].

$$\frac{\Delta x_{\text{met}}}{\Delta T_{\text{met}}} = \frac{\partial x^*}{\partial T} \tag{2.12}$$

The fraction of undercooling and supersaturation can be estimated with the derivative of the solubility curve with regard to the temperature at equilibrium. If heterogeneous or secondary particles are added, the limit would decrease and lie in between the two lines in Figure 2.1. Thus, for every nucleation mechanism, limits have to be determined.

Added materials complicate the estimation and presentation of phase equilibria. In Figure 2.6, a solubility diagram of an exemplary ternary system is depicted.

The temperature is plotted vertically. The concentrations of the three components A, B, and S are represented by the sidelines of the triangular base plain. The solubility lines of binary mixtures are visible at the side plains of the diagram. It is obvious that these diagrams are not easy to handle. Hence, isothermal sections are usually used. In Figure 2.7, an isothermal triangular diagram at $T^{'}$ is shown.

The example shows a solvent S (top corner) with two components A and B (left and right, respectively) at a temperature of $T^{'}$. The solubility line (black full line) can be subdivided into two separate lines. The intersection of both defines

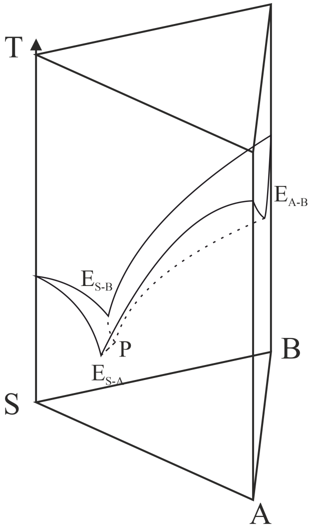

Figure 2.6: Exemplary ternary solubility diagram of a system composing of a solvent S and two materials A and B. Thin full lines show the binary data at the side plains. In dotted lines, connect the binary eutectic points (E) with the ternary eutectic point (P).

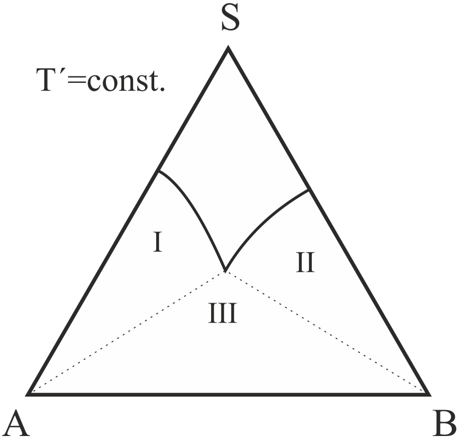

Figure 2.7: Triangular diagram of components A, B and S at $T^{'}$. The solid line inside the triangle depicts the solubility line. In the area I, only the solid component A may crystallize. Similarly, in area II only B may solidify. In area III, both solids A and B may occur.

the eutectic point. Besides solubility lines, the solid equilibrium states can be identified. The fine black lines connect them with the eutectic composition. In this example, both components are stable as a they are. The triangles divided by the fine lines represent the possible phase states. If a composition is given in area I, the point would split into solid material A and a solution on the solubility line. Analogously, a point in area II would result in B and a saturated solution. In area III, both solid entities are stable and in equilibrium with the eutectic solution. Logically, every point left of the solubility line is stable as a clear solution.

In isothermal diagrams, metastable limits can only be displayed with supersaturations Δx_{met}. In Figure 1.3, it is depicted schematically in the triangular diagram as a green dashed area. Multi-component metastable zones were mostly investigated in systems containing a main crystallizing agent and an impurity [Sangwal, 2009, 2010, 2011; Titiz-Sargut and Ulrich, 2002; Ulrich and Frohberg, 2013; Schmidt, Jones, and Ulrich, 2013]. In co-crystallizing systems, metastable zones were determined to be decisive on the final solid formation [Sun et al., 2019]. In other studies, metastable zones of co-crystallizing processes were determined with respect to supercooling but no translation into phase diagrams could be made [Boyd et al., 2010; Nasir et al., 2017; Yang and Florence, 2017]. For general description, metastable supersaturation as well as supercooling should be investigated. Especially graphical illustrations in triangular diagrams are of interest for easy process guidelines in product design. Lorenz et al. [2006] and Polenske and Lorenz [2009] investigated the metastable zone width of methionine enantiomers in water with respect to both and could give process suggestions to produce preferably one of the enantiomers.

2.3 Multi-component mass transfer

As described in the crystal growth section, the mass transfer to the solid is dictated by the reaction step at the interface and the diffusion process in the solution. The diffusional part will be addressed here in more detail. Due to a concentration gradient, a diffusion flux is induced. In general, the time-dependent concentration development of component *i* in a differential volume element is described by the continuity equation (Equation 2.13).

$$\frac{\partial \vec{c}}{\partial t} = \nabla \vec{\dot{n}} \tag{2.13}$$

The vectors are not related to spatial measures but represent the involved components:

$$\vec{c} = \begin{pmatrix} c_1 \\ c_2 \\ \vdots \\ c_{n-1} \end{pmatrix}, \; \vec{\dot{n}} = \begin{pmatrix} \dot{n}_1 \\ \dot{n}_2 \\ \vdots \\ \dot{n}_{n-1} \end{pmatrix}, \; \vec{x} = \begin{pmatrix} x_1 \\ x_2 \\ \vdots \\ x_{n-1} \end{pmatrix} \tag{2.14}$$

The molar flux $\dot{n}_i$ of component *i* in fluids may be described with the approaches of Fick or Maxwell-Stefan. Here, Fick's approach is used because it is mathematically easier to implement. In this work, the maximum mass fractions of dissolved sodium sulfate and sodium carbonate are 0.162 and 0.179, respectively. This represents the eutectic composition at 25°C. Converted into molar fractions this makes a sum of 7 mol-%, which makes it reasonable to define the solvent as a matrix material with substances diffusing in it. This leads to Equation 2.15 for the molar flux.

$$\vec{\dot{n}} = \mathbf{D} \cdot \nabla \vec{c} + \vec{\vec{x}} \cdot \dot{n}_{\text{tot}} \tag{2.15}$$

The Fickian diffusion coefficient **D** is a quadratic matrix of (n-1)x(n-1) elements with n being the number of involved components. One component is handled as a matrix material in which the others diffuse. In case of electrolytic solutions, the solvent lends itself to be the matrix material while the solutes diffuse. In contrast to Maxwell-Stefan diffusion coefficients, Fickian contain non-idealities like activity coefficients [Taylor and Krishna, 1993]. Thus, these have to be investigated experimentally or calculated from other diffusion coefficients. The thermodynamic correction factor in Equation 2.16 takes non-idealities into account and gives the relation between Maxwell-Stefan and Fick.

$$D_{ij} = Đ_{ij} \cdot \Gamma_{ij} \tag{2.16}$$

The definition of the factor was derived for ideal gases and is according to Krishna and Wesselingh [1997]:

$$\Gamma_{ij} = \delta_{ij} + \tilde{x}_i \cdot \left.\frac{\partial ln(\gamma_i)}{\partial \tilde{x}_j}\right|_{T,p} , \delta_{ij} = \begin{cases} 1, & i = j \\ 0, & i \neq j \end{cases} \tag{2.17}$$

Mixtures of liquids can also be described with this expression [Krishna and Wesselingh, 1997]. Electrolytic solutions should normally be treated different. Each ion has a diffusion coefficient and impacts one another. Here we assume that ions always diffuse as ion pairs and these may therefore be treated with the the above correlation.

The generalized Darken-relation connects self-diffusion coefficients with Maxwell-Stefan coefficients (Equation 2.18) [Krishna and van Baten, 2005, see].

$$Đ_{ij} = \frac{\tilde{x}_i}{\tilde{x}_i + \tilde{x}_j} \cdot D_j + \frac{\tilde{x}_j}{\tilde{x}_i + \tilde{x}_j} \cdot D_i \tag{2.18}$$

Self-diffusion can be determined from molecular dynamic simulations or NMR-measurements [Liu et al., 2013; Stejskal and Tanner, 1965]. The diagonal values of the matrix **D** are the diffusion coefficients of component i in the solvent. The others are cross diffusional values between diffusing components. If these are zero, the transport of the materials are independent from each other.

In Figure 2.8, two possible examples of multi-component concentration profiles are displayed. Several others are also imaginable but not considered her.

In (a), solely component A solidifies. Thus, the concentration at the surface is at equilibrium (c_i^*) whereas it is at higher values in the rest of the solution. Due to the lower value at the interface, the other components B and S (solvent) enrich at this position. Hence, it comes to a diffusional flux of these components in direction of the bulk solution. Added components do not only have an influence on the crystallization reaction behavior as stated in the section crystal growth. They also influence the diffusion as can be seen from the diffusion coefficient. In addition, the fact that other components develop a flux off the surface should influence the mass transport. If both components crystallize as is displayed in the Figure (b), the solvent enriches even more at the surface.

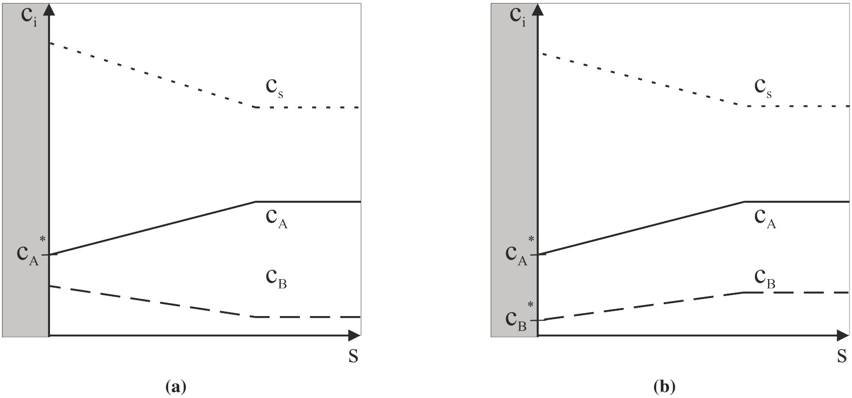

Figure 2.8: Schematic illustration of two possible examples of multi-component concentration evolution during crystallization. In (**a**), component A crystallizes while component B and solvent remain in solution. In (**b**), components A and B crystallize and solvent remains in solution.

3 Simulative case studies

The hypotheses from Section 1.2 are examined theoretically on their impact on solid layer build-up. (i) The influence of changes in phase equilibria is investigated with different solids crystallizing in various solvate states. Metastable states are neglected in theoretical investigation. (ii) Growth kinetics of two components are varied to observe the main influence factors. (iii) Supersaturation build-up seems to be crucial for solid assemblage from state of the art and theoretical background. Different cooling rates are examined on its impact on solid assemblage. The calculations are conducted in MATLAB® 2019b and are based on differential mass balances. All computations are conducted with parameters of the model system Na_2SO_4, Na_2CO_3, and H_2O, which is used later for all experimental studies. The principle simulation flow-sheet is depicted in Figure 3.1.

After initialization, supersaturation is calculated with a plug-in of the software PhreeqC of USGS [Parkhurst and Appelo, 2013]. The database *FREZCHEM* is used to determine the prevailing activities, supersaturations and equilibrium compositions [Marion et al., 2010; Toner and Sletten, 2013]. The database contains experimentally determined parameters to calculate thermodynamic equilibria with the Pitzer approach (see Pitzer [2018]) at temperatures below 25°C for concentrated solutions. It is parameterized for the $Na–K–Mg–Ca–Fe–H–Cl–SO4–NO_3–OH–HCO_3–CO_3–CO_2–O_2–CH_4–H_2O$ system. Once a component is supersaturated, crystallization is possible. The change of moles in solution is calculated each time step with the resulting fluxes from crystallization. Phase transfer from liquid to solid is calculated with the simple power law function. Because of the phase transfer fluxes, concentration gradients occur at the solid-liquid boundary. This would result in concentration gradients that induce diffusive transport (compare description in Section 2.3). Here, it is assumed that the diffusive transport

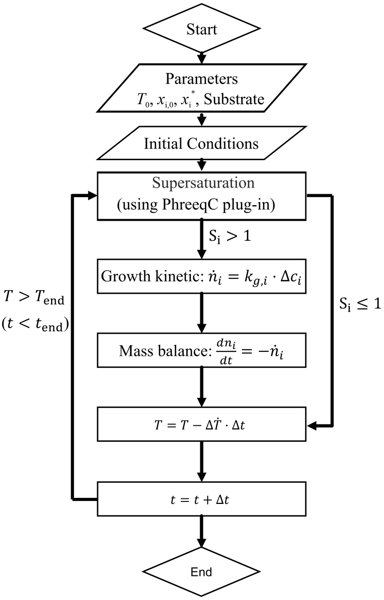

Figure 3.1: Flow-sheet of thin film modeling simulation.

within the film is so fast that arising concentration gradients are immediately compensated. Therefore, the bulk solution is approximated as ideally mixed (compare Figure 3.2).

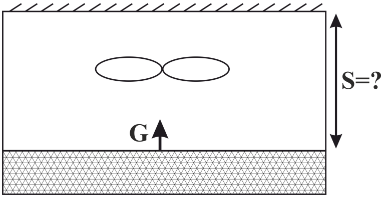

Figure 3.2: Schematic depiction of simulation environment. The bulk solution is assumed to be ideally mixed. The substrate will grow with the growth rate G.

Hence, no concentration gradients nor diffusion fluxes occur. The solution is simulated as a confined 1D sheet with an impermeable surface and a growing interface ($\widehat{=}$layer). Nucleation and metastability are neglected which is why all components including foreign materials are always treated as growable onto the substrate. Foreign materials are defined as substances, which are not present in the substrate at the beginning. In order to supersaturate the solution, the temperature is decreased. Because of ideally mixing conditions, the simulated volume is not discretized spatially. A more detailed description of the model with all equations and variables is given in Appendix A.3.

3.1 Solvate formation

The impact of phase equilibria on solidification behavior can either be attributed to a change in solubility because of a temperature changes or to different stable solid entities. Since many materials build solvates dependent on process conditions, its impact is investigated theoretically. Besides physicochemical properties of the resulting solid, the solidification process itself can be influenced. Due to the mass transport of additional solvent with the crystallizing material, the overall mass balance and with it the transient concentration changes are strongly affected. In order to compare different cases, initial solution conditions are set to equilibrium at eutecticum of the model system Na_2SO_4, Na_2CO_3, and H_2O at 25°C (eutectic composition at 25°C: $x_{\mathrm{Na_2SO_4}} = 0.162$, $x_{\mathrm{Na_2CO_3}} = 0.179$ and $x_{\mathrm{H_2O}} = 0.659$). The resulting solid states are the respective decahydrates. The solid layers resulting from simulations will be discussed with respect to their mass fraction of electrolyte ξ_i in the solid (Equation 3.1).

$$\xi_i = \frac{x_i}{\sum x_j},\ j \neq \text{solvent} \tag{3.1}$$

Because the stable solid entities are both decahydrates, the water content is spared out in the mass fraction expression. That means, a fraction of $\xi_{\mathrm{Na_2SO_4}} = 1$ displays that the solid material is made of sodium sulfate decahydrate only. The mass fractions of the solid will be plotted as a function of the layer thickness, which is calculated from phase transferring material. All calculations are done for the case that sodium sulfate decahydrate is the substrate material and sodium carbonate decahydrate the foreign material. Hence, the initial solid fraction of sodium sulfate and sodium carbonate are $\xi_{\mathrm{Na_2SO_4}} = 1$ and $\xi_{\mathrm{Na_2CO_3}} = 0$. Mass transfer coefficients of sodium sulfate decahydrate and sodium carbonate decahydrate are set arbitrarily to $k_{g,\mathrm{Na_2SO_4}} = 10^{-6}$ m s^{-1} and $k_{g,\mathrm{Na_2CO_3}} = 5 \cdot 10^{-7}$ $m^{2.5}$ $mol^{-0.5}$ s^{-1}, respectively. As will be seen later in this work (Section 4.2.4), these values are in the order of magnitude that arise from multi-component crystal growth experiments for the material system Na_2SO_4-Na_2CO_3-H_2O. Exponents are assumed to be $g_{\mathrm{Na_2SO_4}} = 1$ and $g_{\mathrm{Na_2CO_3}} = 1.5$. With these chosen coefficients, the substrate component grows with a faster kinetic at low supersaturation compared to the foreign component. Due to the exponent $g_{\mathrm{Na_2CO_3}} > 1$, the foreign component is more dependent on supersaturation. In Figure 3.3, the influence of exponent *g* on growth velocity *v* is shown.

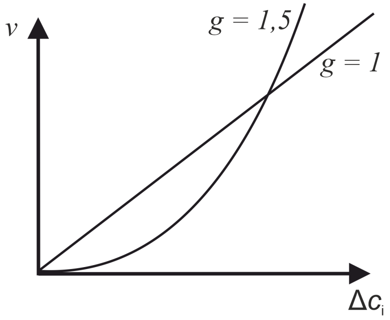

Figure 3.3: Impact of different exponents *g* on the growth velocity in dependence of the supersaturation. At low supersaturations the growth velocity *v* with $g = 1.5$ is lower compared with $g = 1$. At a certain supersaturation this behavior changes once both lines cross.

At low supersaturations, the growth velocity with $g = 1$ is greater than with $g = 1.5$. At a certain supersaturation, the relation is inverted. Dissimilar kinetics are chosen because differences in other parameters are easier to determine. After reaching the final temperature of 10°C with a cooling rate of 0.01 K s^{-1}, the solution is held isothermally for an additional hour.

In addition to the investigations of hydrated solids, the impact of changing the hydration state is addressed. For this purpose, anhydrous solids are examined without changing any properties other than the number of water molecules from ten to zero. Changing the thermodynamic stable forms would result in changes of other properties such as solubility. Because anhydrous forms of both materials are not stable at low temperatures, the plug-in PhreeqC is used as if both components would crystallize in their stable forms in the temperature range, namely decahydrates. To simulate anhydrous crystallization, the mass balances are adapted so that water does not transfer from liquid to solid but solely the electrolytic components. Hence, the difference in the anhydrous cases correspond solely to no water integration into the solid. Hence, only the mass balances are changed. In Figure 3.4, two cases are shown with different hydration states of the resulting solids.

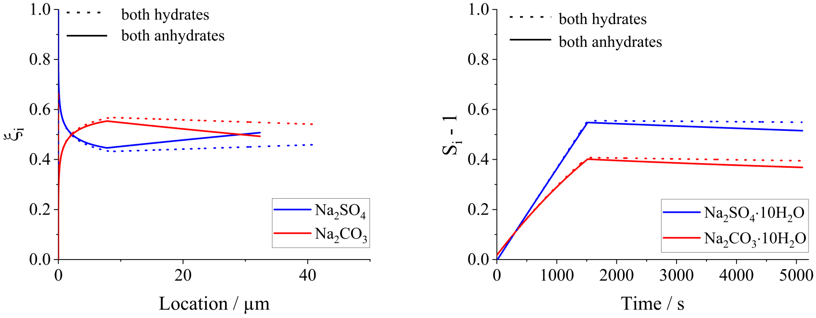

(a) **(b)**

Figure 3.4: Case studies on the influence of solvate formation. Diagram (**a**) depicts the resulting solid layer compositions. In (**b**), calculated supersaturations (with PhreeqC) over time are plotted. Solid lines were simulated with both components crystallizing as decahydrates. Dotted lines represent calculations of anydrous crystallization.

In Diagram (a), the mass fractions of both materials are depicted with respect to the location in the resulting solid layer. Location 0 µm corresponds to the substrate. With dotted lines, the results from simulations are shown with both components crystallizing as decahydrates. Solid lines represent cases of anhydrous crystallization of both components. Blue color represents sodium sulfate and red stands for sodium carbonate. In the vicinity of the substrate, both cases are very similar. The mass fraction of sodium sulfate decreases strongly and sodium carbonate tends to be the major component in the solid in early occurring solid layers. At a distance of 10 µm, the composition profiles of the cases change. In case both components crystallize as solvates, the mass fraction of sodium carbonate remains clearly higher than sodium sulfate. But with increasing solid thickness, the fraction of the foreign component reduces. If both components crystallize as anhydrates, the reduction of foreign component begins at the position of 10 µm and results in an intersection at location 30 µm. From this point, the substrate material sodium sulfate is dominant.

In Diagram (b), supersaturation of both components $S_i - 1$ is depicted over time. Hence, it represents the driving force development of the process. Again, blue and red stand for sodium sulfate and sodium carbonate, respectively. Interestingly, the courses of supersaturation in Figure 3.4 (b) do not differ as much as the solid layer evolutions. This is because of the assumption that the equilibrium is not affected due to the change from hydrates to anhydrates. In both cases, it increases with supercooling up to values of 0.6 and 0.4, respectively. After reaching a maximum, both decrease slightly with process time. The inclination of the anhydrous simulation is steeper than the other. Hence, just little differences in supersaturation development due to changes in the mass balance provoke strong deviations in the resulting solid layers. Differences are found especially in higher solid layers. Early layers are not affected at all.

If differences were not only assumed in mass balances but also in thermodynamic behavior, the influences on stratification must be even stronger. Therefore, a profound investigation of the phase equilibrium is necessary.

3.2 Crystal growth rates and limitations

In Hypothesis II in Section 1.2, growth kinetics were identified as influencing factors of the solid layer composition. Final layer assemblages as well as process times should be influenced greatly. To compare different growth kinetics, three cases are simulated. Differences in solid layer assemblages are assumed to appear if the kinetics of both components differ. The solely varied parameter here is the growth exponent g of the foreign component. With it, the influence of slower and faster crystallizing materials is considered while the other component is not affected at all. Another possibility would be the variation of $k_{g,i}$, which is not considered in this work. The kinetic values are chosen arbitrarily to determine their impact. All other parameters are kept constant. Again, a saturated solution at 25°C with an initial composition of $x_{\text{Na}_2\text{SO}_4} = 0.162$ and $x_{\text{Na}_2\text{CO}_3} = 0.179$ is brought in contact with a sodium sulfate substrate. A cooling rate of 0.01 K s^{-1} is applied. The final temperature of 10°C is held for an additional hour. Thus, the total process time adds up to 5100 s. The mass transfer coefficients of sodium sulfate and sodium carbonate are set again arbitrarily to $k_{g,\text{Na}_2\text{SO}_4} = 10^{-6}$ m s^{-1} and $k_{g,\text{Na}_2\text{CO}_3} = 5 \cdot 10^{-7}$ m$^{3g_{\text{Na}_2\text{CO}_3} - 2}$ mol$^{-(g_{\text{Na}_2\text{CO}_3} - 1)}$ s^{-1}, respectively. The exponent of sodium carbonate $g_{\text{Na}_2\text{CO}_3}$ is 1, 1.5, and 2. This setting allows to examine the growth behavior if one component sodium sulfate is diffusion limited while the other - sodium carbonate - is strongly dependent on the order of crystallization.

In Figure 3.5, spatially resolved solid compositions in the direction of (layer) growth (Diagram (a)) and supersaturation in solution over time (Diagram (b)) are shown.

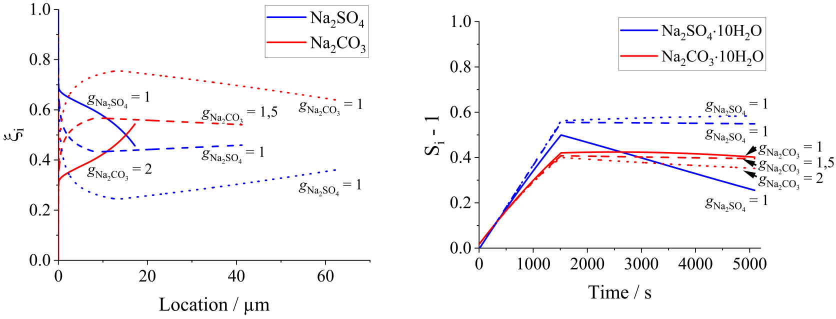

(a) **(b)**

Figure 3.5: Case studies on the influence of growth kinetics. Diagram (**a**) depicts the resulting solid layer compositions. On the right (**b**), calculated supersaturations (with PhreeqC) over time are plotted.

The diagram on the left shows the solid composition as a function of vertical location in the solid layer. It is evident that the layer thickness increases with increasing the exponent of the foreign component. Additionally, the composition of substrate material at the interface varies drastically with increasing exponent. In cases of exponents g not equal to one, the foreign components share rapidly takes values higher than the substrate component. The extreme example of $g_{\text{Na}_2\text{CO}_3} = 2$

leads to a mass fraction of sodium carbonate of nearly 80% at 10 µm. Afterwards, it comes to a static increase of sodium sulfate content. Thinking the process further, contents would equalize and sodium sulfate would be the dominant component again. The other extreme is represented by the solid lines with $g_{\mathrm{Na_2CO_3}} = 1$. The content of substrate material decreases slower and equalizes with foreign content at 20 µm. Afterwards, the inclination of the foreign component is high. This would lead to high contents of foreign component from this point on. In case of $g_{\mathrm{Na_2CO_3}} = 1.5$, the resulting solid layer is mostly homogeneous. Contents lie close to 50%.

The diagram on the right displays the time evolution of supersaturation $S - 1$ in the solution on top of the substrate. It shows similar courses of sodium sulfate and carbonate supersaturation for all simulations. It is characterized by an inflection point at 1500 s because of the end of the cooling process. Afterwards, supersaturation declines with a constant rate or stagnates. The evolution of sodium carbonate supersaturation decreased with higher exponents. But the differences to $g_{\mathrm{Na_2CO_3}} = 1$ are small. The lower the coefficient, the higher the inflection point and the steeper the ongoing supersaturation. The most significant influence of foreign components exponent can be noticed in sodium sulfate supersaturation. While supersaturation strongly decreases with an exponent of $g_{\mathrm{Na_2CO_3}} = 1$, it remains mostly constant in the other cases.

The conclusion of the case study is that stratification increases with higher differences in mass transfer kinetics in the case of $\mathrm{Na_2CO_3}$/$\mathrm{Na_2SO_4}$ in the prevailing parameter range. It is probable that these results can be transferred to most other systems and parameter ranges. Hence, multi-component concurrent kinetic analyses are necessary to predict the spatially resolved solid phase assemblages.

3.3 Rate of supersaturation build-up

As was hypothesized (Section 1.2), the rate of supersaturation build-up is crucial for the solid formation. Growth rates are directly affected by supersaturation. Hence, the earlier higher supersaturations are reached, the higher the solidification fluxes. On the other hand, process time is relevant, too. The longer a solid is exposed to a supersaturated solution, the longer growth can take place. To compare supersaturation rates, it is necessary to define a process endpoint. On the one hand, it can be defined by reaching a desired temperature. Thus, the process time of slower cooling rates is longer. On the other hand, process termination can be defined by a certain time range. Hence, the higher cooling rate would reach lower temperatures. This could result in other thermodynamic equilibria which is not desired. An adequate solution to combine thermodynamic and time considerations is the definition of a final temperature and an isothermal part until reaching the defined process time.

In the following, simulation results with and without isothermal holding times at final temperatures of 10°C will be discussed. In Figure 3.6, a comparison of two cooling rates of a system crystallizing with equal crystal growth kinetics is depicted.

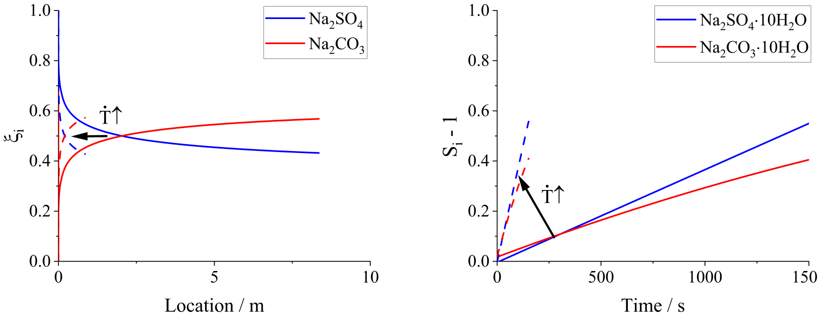

(a) **(b)**

Figure 3.6: Case studies on the influence of supersaturation rate. Diagram(**a**) depict the resulting solid layer compositions. On the right (**b**), calculated supersaturations (with PhreeqC) over time are plotted. Solid lines were simulated with a cooling rate of 0.01 K s^{-1}. Dashed lines were calculated with 0.1 K s^{-1}.

The initial composition is set to $x_{\mathrm{Na_2SO_4}} = 0.162$ and $x_{\mathrm{Na_2CO_3}} = 0.179$ which corresponds to a saturated solution at 25°C. A substrate composed of sodium sulfate is contacted and cooling rates of 0.01 K s^{-1} and 0.1 K s^{-1} are applied. Mass transfer coefficients are again set arbitrarily to $k_{g,\mathrm{Na_2SO_4}} = 10^{-6}$ m s^{-1} and $k_{g,\mathrm{Na_2CO_3}} = 5 \cdot 10^{-7}$ m$^{2.5}$ mol$^{-0.5}$ s^{-1}, respectively. The exponents are $g_{\mathrm{Na_2SO_4}} = 1$ and $g_{\mathrm{Na_2CO_3}} = 1.5$. Similar to other case studies, different kinetics are chosen for both components because resulting layers show significant differences by varying other parameters.

Solid lines correspond to the slower cooling rate. Hence, process time is 1500 s. The final thickness of the solid layer is calculated to 8 µm. The solid composition is mostly homogeneous. Close to the substrate at the y-axis, the initial solid composition of sodium sulfate changes to a value below sodium carbonate. The finally calculated fraction of sodium carbonate reached 0.6. Looking at the supersaturation over time for a slow cooling rate in Diagram (b), both materials increase steadily. The slope of sodium sulfate is steeper which leads to higher supersaturations compared to sodium carbonate after 300 s. At first, more sodium sulfate crystallizes which leads to higher contents in the solid layer. In the solution, supersaturation of both components increases due to cooling. Sulfate is a little more temperature dependent. Thus, the slope is steeper. Once supersaturation of both intersect, a stronger growth of sodium carbonate leads to a higher content in the solid. Afterwards, carbonate dominates the growth process and leads to a higher amount in the solid.

The other example shows the same process but with a cooling rate of 0.1 K s^{-1}. With dashed lines in Diagram (a), the solid composition is displayed. The final solid thickness is reduced and adds up to 1 µm. Due to the short process time of 150 seconds, just a small amount is able to transfer to the solid phase. Close to the substrate sodium sulfate is the major material in the solid. Early, both components are equally represented and afterwards sodium carbonate has a higher fraction. Because of the high cooling rate, mass transfer through solidification is not able to catch up. Hence, both supersaturation courses incline, sodium sulfate steeper than sodium carbonate. The final supersaturation is similar compared to the slower process.

Comparing both processes, two similarities can be concluded. First, the foreign component sodium carbonate has a higher fraction at early stages of solid generation. With lower cooling rates, the break-even point is reached later than with higher rates. Second, the inclination of sodium sulfate supersaturation is steeper than sodium carbonate in both processes. Only small qualitative differences can be recognized in solid layers despite the obvious deviation in thickness. Thinking further, it would be expected that solidification fluxes of sodium sulfate increase which would lead to a higher content of this component in upcoming layers.

To investigate the impact of supersaturation rates with equal process times, another case study is shown in Figure 3.7. This time, the total process time is fixed to 5100 seconds. The final temperature for both cooling rates is again 10°C. Upon reaching the temperature, an isothermal part follows. All other variables are equal to the previous case.

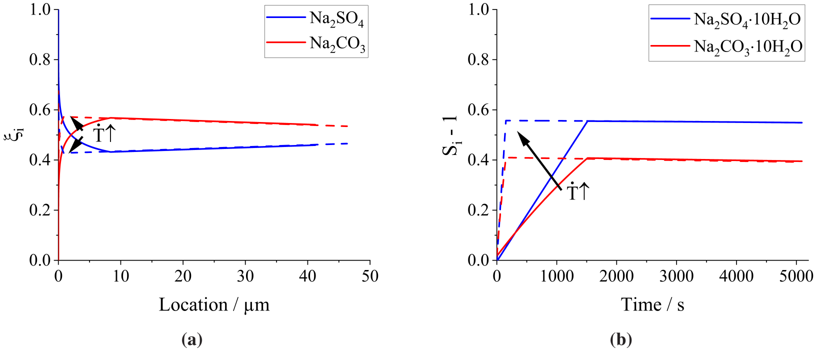

Figure 3.7: Case studies on the influence of supersaturation rate. Diagram (**a**) depicts the resulting solid layer compositions. On the right (**b**), calculated supersaturations (with PhreeqC) over time are plotted. Solid lines were simulated with a cooling rate of 0.01 K s^{-1}. Dashed lines were calculated with 0.1 K s^{-1}. In Diagram (b), the inflection point of the courses indicates the initiation of the isothermal part.

The courses in Diagrams (a) and (b) illustrate continuations of the diagrams of Figure 3.6. The final thicknesses of both simulations still deviate despite equal process times. The slow cooling rate of 0.01 K s^{-1} produces a final layer thickness of a little more than 40 µm while the faster rate generates nearly 50 µm. Interestingly, the solid compositions over solid thickness lie on top of each other. Hence, the only difference in solid composition is generated in the vicinity of the substrate. From approximately 10 µm, the courses are very similar. Also, the supersaturations after 1500 s are equal. Up to that point, the faster cooling rate rapidly elevates supersaturation to values of 0.6 and 0.4, respectively. The growth kinetics are too slow to decrease supersaturation so that the process points after 1500 s are independent from the cooling rate.

Supersaturation rate influences the solid layer assemblage mostly in the direct vicinity of the substrate. With the prevailing parameters, no greater differences can be observed and layers are mostly homogeneous. However, stronger impacts are expected with greater differences in kinetics. Also, metastable states are not considered here. Supersaturation rate influences nucleation and thus, impacts solid assemblage. Hence, experimental investigation is still necessary to assess this process parameter.

3.4 Conclusion

In the case studies, it is shown that phase transfer kinetics, phase equilibria, and supersaturation rate play a key role in stratification of materials during crystallization. Phase equilibria are discussed in terms of different solvate states. A great difference was observed if both components crystallize anhydrously or as decahydrates. In simulations, only the mass balance was changed so that the water flux was adjusted to the hydrate state. Realistically, solubility, activity and other properties would also change. That makes phase equilibria crucial for layer assemblages. Growth kinetics influence final layer assemblages especially if kinetics differ greatly. Strong differences result in strong stratification up to phase separation. Supersaturation rates impact layer compositions not as strongly as expected. But still, higher supersaturation rates lead to more homogeneous compositions.

The simulations already show how the individual process parameters influence the solid layers. However, these are only tendencies that must be verified with experimental investigations. In addition, metastable zones were not considered in the case studies. All components were assumed to grow on a substrate without building a nucleus. However, this mechanism has to be considered. Foreign components have to build nuclei on a substrate and start to grow afterwards. Logically, at the beginning, metastable zones of foreign materials would lead to a sole crystallization of the substrate material. With higher supersaturations of the foreign material, it will start to crystallize, too.

In the following Chapter 4, the hypotheses from Section 1.2 will be investigated experimentally. The shown tendencies of varied parameters from simulations should be fortified or disproved with experimental data. Therefor specific experiments are designed to answer the questions of layer build-up from multicomponent electrolytic solutions.

4 Experimental results and discussion

In this chapter, the experimental procedures for determining the before stated required parameters and experimental results are presented. First of all, phase equilibria and metastable zone widths will be addressed. Especially the determination of metastable zones is complex and will be explained in detail. A pseudo-binary approach will be used to evaluate the metastable zones of a ternary system to examine Hypothesis I. All nucleation mechanisms will be discussed and their respective metastable zones will be analyzed. Furthermore, their relevance with regard to stratification effects will be explained (Section 4.1). In a second part, the determination of growth kinetic parameters of involved components in multi-component solutions is explained. A new method based on desupersaturation measurements in a thin film is introduced and the results of experiments conducted at different temperatures and supersaturation are shown. With it, Hypothesis II - Kinetics of multiple crystallizing materials can be measured simultaneously and independently - will be verified (Section 4.2). Finally, stratification experiments are conducted to show that substrate materials as well as supersaturation rate influence the final composition (Hypothesis III). With this, stratification behavior in general will be evidenced (Section 4.3).

4.1 Phase equilibria and metastable zone widths of multi-component solutions

In this section, Hypothesis II - Metastable zones of ternary systems can be predicted by a pseudo-binary approach - will be examined. The experimental idea and set-up as well as some results were developed and conducted together with

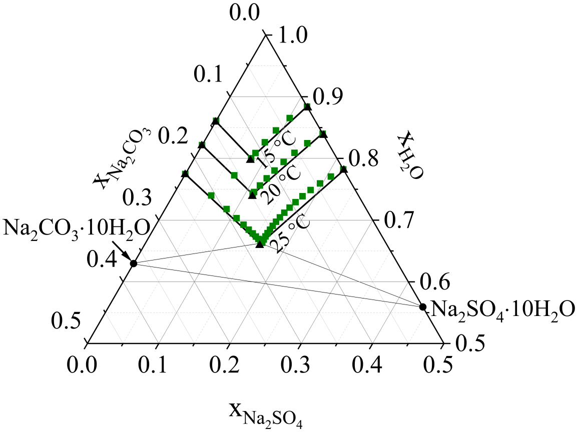

Figure 4.1: Triangular diagram of the material system Na_2SO_4-Na_2CO_3-H_2O. The black triangular data points are taken from Caspari [1924]. The green squares are calculated with PhreeqC and its database *FREZCHEM* [Marion et al., 2010; Toner and Sletten, 2013]. The black lines are linearized approximations of the solubility curve.

Richard Samman and Michaela Gratzfeld in their bachelor and master theses, respectively. In order to determine metastable zones some assumptions apply for the phase equilibria of a ternary system. (i) There is no change in solid state equilibrium phases in the investigated temperature range. This is true for the material system Na_2SO_4-Na_2CO_3-H_2O at temperatures below 30°C [Caspari, 1924]. (ii) Solubility lines in ternary diagrams can be assumed to be linear. This is a reasonable approximation as is shown in Figure 4.1.

The phase diagram at different temperatures from 15 to 25°C shows a nearly linear behavior of the solubility lines. With black triangles, binary and eutectic experimental solubilities from literature are marked. Green rectangles represent calculated solubility points at three different temperatures - 15, 20, and 25°C. The database *FREZCHEM* [Marion et al., 2010; Toner and Sletten, 2013] in PhreeqC [Parkhurst and Appelo, 2013] was used for calculations. The stable solid states at these temperatures are indicated with black dots and display the decahydrates of sodium sulfate and sodium carbonate. In Appendix A.4, an additional triangular diagram of the material system at 30°C is depicted in Figure A.4. The phase behavior changes drastically at temperatures above 30°C. The linearization of the solubility line is important for implementation of the following assumption: (iii) Equation 2.12 applies in the form of Equation 4.1 also for multi-component systems:

$$\left.\frac{\partial x_i}{\partial T}\right|_{x_j=const.} = \frac{\Delta x_{i,\mathrm{met}}}{\Delta T_{\mathrm{met}}} \tag{4.1}$$

The left side of the equation represents the inclination or first derivative of the solubility curve at a constant mass fraction of an added component j. The other side stands for the relation of the metastable supersaturation $\Delta x_{i,\mathrm{met}}$ and metastable temperature difference ΔT_{met}. To obtain a metastable zone width in an isothermal ternary triangular diagram, it is necessary to express it in terms of $\Delta x_{i,\mathrm{met}}$. One possible way would be the isothermal method. Several solutions with known compositions are exposed to temperatures below the solubility temperature and induction time until crystallization is monitored. The disadvantage of this approach is that large numbers of solutions have to be investigated. Not only different compositions have to be analyzed but also repetitions with new samples have to be conducted. One other possibility for investigation would be a gradual removal of the solvent. Again, a large number of samples is necessary to get significant information on metastable states. Furthermore, a constant supersaturation rate is necessary. Otherwise, no generalizations can be retrieved. To achieve supersaturation, evaporation of the solvent would be appropriate. Since evaporation is strongly dependent on the water activity which itself depends on the composition, the rate has to be adapted permanently. A better controllable way is the polythermal approach with a theoretical conversion to the triangular diagram. Taking Equation 4.1, $\Delta x_{i,\mathrm{met}}$ can be calculated with the knowledge of $\left.\frac{\partial x_i}{\partial T}\right|_{x_j=const.}$ and ΔT_{met}.

In the following sections, the application of the stated theory for primary homogeneous nucleation will be explained. Also, secondary and heterogeneous nucleation will be discussed. The latter is of greater interest in this work since the foreign component has to form growable nuclei on the substrate.

4.1.1 Methodology

To investigate metastable limits of homogeneous nucleation, initial solutions over the whole concentration range with a known equilibration temperature are prepared. All solutions are set to equilibrium with the stable solid entities sodium sulfate decahydrate and sodium carbonate decahydrate. The stirred suspensions are stored at a constant temperature - 15, 20, and 25°C - for at least one week. The supernatant liquid is filtered and analyzed quantitatively with Raman spectroscopy (see Appendix A.5). With this, the solubility line is determined experimentally. Afterwards, the metastable limits are investigated with the polythermal method [Nyvlt, 1984]. For this purpose, the crystallization system Crystalline (Technobis) is used. The system has eight independent reactors (glass vials with a volume of 6 mL and a diameter of 16.6 mm), which can be homogenized with magnetic bars or overhead stirrers. The reactor temperatures range from -20°C to 145°C.

After initialization at a temperature above the solubility temperature ($T > T^* + 10$ K) and ensuring total dissolution, the transmission signal is set to 100%. The stirring speed of a magnetic bar is set to 1000 min^{-1} at all time and in all experiments. Then, a constant subcooling rate of 0.1 K min^{-1} is applied to the point of -10°C. Once the transmission decreases, the nucleation point is found. It is important to note that the transmission signals do not decrease with the formation of the first nucleus. It would react only after the formation and growth of several particles. Hence, nucleation probably starts earlier than measured. The time lag is neglected here because of low cooling rates. Thus, the metastable temperature difference will not be affected strongly. After reaching the low point temperature, the solution is heated with a rate of 10 K min^{-1} and held at the initial temperature for 90 minutes. The long holding time is necessary to dissolve the salt to have a clear solution again. Afterwards the cycle is repeated for at least five times. This leads to a series of metastable temperature differences ΔT_{met}. This is done for different compositions and for different equilibrium temperatures. Those are converted with Equation 4.1 into $\Delta x_{i,\text{met}}$.

The investigation of heterogeneous nucleation is not approached with the polythermal but with the isothermal method. The experiments should simulate the behavior of a solution in contact with a crystalline solid material at a specific supersaturation. Ideally, the two main model substances sodium sulfate decahydrate and sodium carbonate decahydrate would be used as heterogeneous nuclei to study the effects of both on the respective counter material. However, this is not possible due to the solubility behavior. Sodium tetraborate decahydrate (known as borax) and calcium carbonate (calcite) are used as heterogeneous seeds. Borax is selected because of its crystal structure, which is monoclinic like the decahydrates of sodium sulfate and carbonate. Also, the lattice parameters are similar (compare Table 4.1).

Table 4.1: List lattice parameters of sodium sulfate decahydrate, sodium carbonate decahydrate, borax, and calcite.

lattice parameters	$Na_2SO_4 \cdot 10\,H_2O$	$Na_2CO_3 \cdot 10\,H_2O$	$B_4Na_2O_7 \cdot 10\,H_2O$	$CaCO_3$
a	11.51 Å	12.750 Å	11.858 Å	4.989 Å
b	10.38 Å	9.001 Å	10.674 Å	-
c	12.83 Å	12.590 Å	12.197 Å	17.062 Å
angle (other than 90°)	β =107°	β =115.83°	β =106.41°	γ =120°
source	[Ruben et al., 1961]	[Libowitzky and Giester, 2003]	[Morimoto, 1956]	[Markgraf and Reeder, 1985]

In some publications, borax was already used as seeding agent for sodium sulfate decahydrate [Telkes, 1952; Purohit and Sistla, 2021]. On the contrary, calcite is trigonal and very different from the investigated substances. Thus, the seeding effectivity is expected to be lower. In Table 4.2, the respective crystal systems and purities of all substances used in the experiments are listed. All chemicals were purchased from Carl Roth GmbH + Co. KG (Karlsruhe, Germany).

Table 4.2: List of used substances and selected properties.

substance	crystal system	material specification
Na_2SO_4	orthorhombic	$\geq 99\%$ p.a., ACS
$Na_2SO_4 \cdot 10\,H_2O$	monoclinic	$\geq 99\%$ p.a., ACS
Na_2CO_3	monoclinic	$\geq 99\%$
$Na_2CO_3 \cdot 10\,H_2O$	monoclinic	$\geq 99.5\%$ Ph.Eur.
$B_4Na_2O_7 \cdot 10\,H_2O$	monoclinic	$\geq 99.5\%$ p.a., ACS, ISO
$CaCO_3$	triclinic	$\geq 98.5\%$ Ph.Eur.

To find the metastable state of heterogeneous nucleation, supersaturated solutions are prepared. Their compositions shall be within the previously determined metastable zone of homogeneous nucleation for a certain temperature. In order to dissolve all components the temperature is initially increased. Afterwards, the clear solutions are cooled to the investigation temperature, i.e. the corresponding temperature at which metastable states should be analyzed and held for 30 minutes. Again, a magnetic stir bar at a speed of 1000 min^{-1} is used. Then, a suspension of seeding solution is added. A schematic drawing is shown in Figure 4.2 on the left. Afterwards, an induction time of two hours is provided. If no crystallization occurred in three independent reactors, a higher concentration is investigated. On the contrary, if a nucleation event is observed, the concentration is lowered. If the difference in Δx_i of a nucleated and a non-nucleated solution is lower than 0.005, the zone width is found. This procedure is conducted at three points in the phase diagram, one of which in the three phase area and two in the respective two phase areas (compare Figure 2.7).

Similarly, secondary nucleation limits are investigated. Single crystals are used instead of a seeding solution. For this purpose, either sodium sulfate decahydrate or sodium carbonate decahydrate particles are fixed at one position (Figure 4.2 on the right).

Due to the fixation, abrasion effects of suspended particles can be neglected. Hence, transmission changes and observation of suspended crystals can be referred directly to the presence of the solid particle.

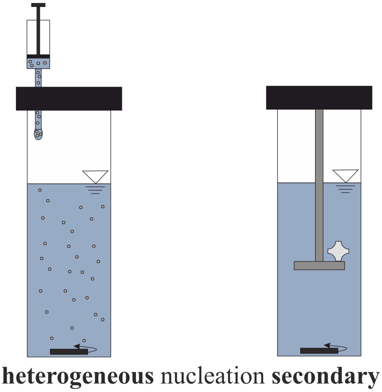

Figure 4.2: Schematic depictions of seeding strategies for heterogeneous (on the left) and secondary nucleation (on the right). A suspension consisting of solution and seeding particles is added at the time when the desired temperature is reached. Similarly, a single seed particle attached to a carrier is added if secondary nucleation is investigated.

4.1.2 Results

At first, homogeneous nucleation will be discussed. The metastable zone limit (MSZL) and the solubility line define the investigation range for the two other nucleation mechanisms. It is assumed that limits of heterogeneous and secondary nucleation lie within the homogeneous metastable zone.

Homogeneous nucleation

From Equation 4.1 it is apparent that two variables have to be determined to obtain the metastable supersaturation $\Delta x_{i,\mathrm{met}}$. The derivative of the solubility curve at a constant mass fraction of component j can be determined theoretically while the metastable subcooling ΔT_{met} has to be identified experimentally.

First, the triangular diagram is transformed in a pseudo-binary phase diagram. The procedure is displayed in Figure 4.3.

Solubility lines at several temperatures (here 15, 20, and 25°C) are displayed as black lines in diagram (a). Additionally, lines with constant mass fractions of sodium sulfate and sodium carbonate are shown in blue and red, respectively. The intersections of solubility lines with constant mass fraction were transferred to

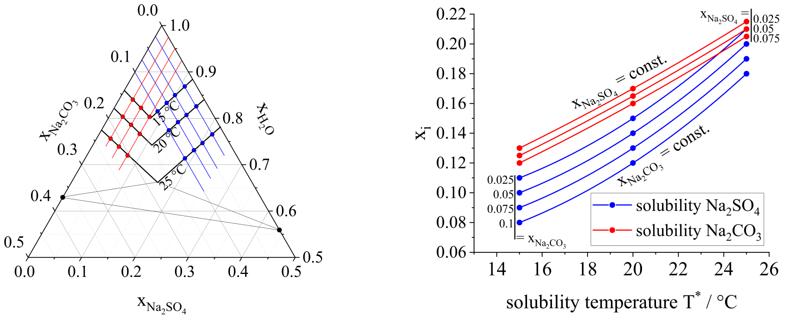

(a)

(b)

Figure 4.3: Diagram (**a**) represents the triangular diagram of Na_2SO_4-Na_2CO_3-H_2O at three different temperatures. Lines with constant mass fractions of sodium carbonate (in red) and sodium sulfate (in blue) are added. The intersections are transferred to diagram (**b**).

the pseudo-binary diagram (b). The points of one solubility line with a constant mass fraction x_j can be described with a quadratic function in this temperature range. Since all lines of one component i are similar but shifted upwards, their inclinations and derivatives are equal. The resulting derivatives of $\left.\frac{\partial x_i}{\partial T}\right|_{x_j=const.}$ are shown in equations 4.2 as functions of the solubility temperature T^* in °C.

$$\left.\frac{\partial x_{Na_2SO_4}}{\partial T}\right|_{x_{Na_2CO_3}=\text{const}} = -6.07 \cdot 10^{-4} + 5.34 \cdot 10^{-4} \cdot T^* \tag{4.2a}$$

$$\left.\frac{\partial x_{Na_2CO_3}}{\partial T}\right|_{x_{Na_2SO_4}=\text{const}} = 2.23 \cdot 10^{-3} + 3.06 \cdot 10^{-4} \cdot T^* \tag{4.2b}$$

The experimental determination of metastable subcooling ΔT_{met} was conducted at three different temperatures. The cooling and stirring rates were kept constant at 0.1 K min^{-1} and 1000 rpm. All experiments were repeated at least five times and resulted in a ΔT_{met} distribution. The results will be explained exemplarily for 20°C. Results for 15 and 25°C can be reviewed in Appendix A.8. The final results of these experiments will be shown in the following without derivation.

From polythermal measurements, the nucleation temperatures of eight different and independent compositions are shown in Diagram (a) in Figure 4.4.

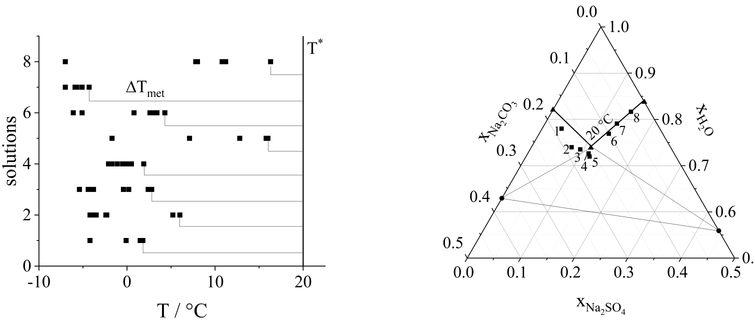

(a) **(b)**

Figure 4.4: In Diagram (**a**), nucleation temperatures are displayed as black squares. On the y-axis, eight different solutions are assigned. Their initial compositions are displayed in Diagram (**b**). Metastable subcooling ΔT_{met} was defined as the temperature difference between saturation temperature T^* and the highest nucleation temperature.

The saturated solution's initial compositions are displayed in Diagram (b). They show a slight deviation from the assumed linear behavior of the solubility line especially on the carbonate side. In Diagram (a), a broad distribution of each composition's nucleation temperature can be seen. No trend of solution composition on metastable subcoolings was found. To find a consistent description of a metastable zone with stratification, the lowest subcooling difference was defined as metastable. This corresponds to the highest nucleation temperature. Up to this, spontaneous nucleation is unlikely. Hence, all metastable subcoolings of different solutions at all investigated saturation temperatures can be compared (Figure 4.5).

Still, the deviations between several solutions are high. The lowest metastable subcoolings were taken as measures for each saturation temperature. This corresponds to the assumption that subcooling or metastable limits do not depend on the composition. Again, this implies that nucleation events are unlikely up to this temperature difference.

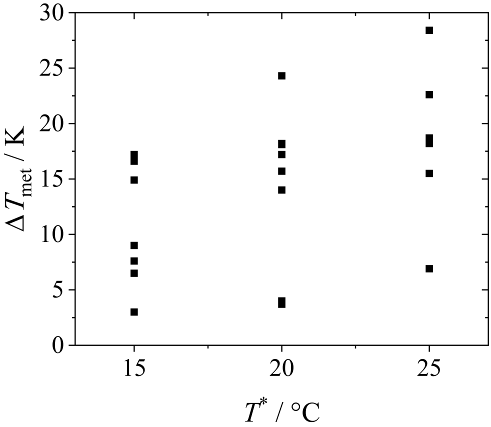

Figure 4.5: Metastable subcoolings ΔT_{met} are applied over saturation temperature T^*. Each square resulted from minimum subcooling of independent solutions.

A slight increase of metastable subcooling can be observed over saturation temperature. For convenience an averaged and constant metastable subcooling of $\Delta T_{\text{met}} = 5$ K was assumed for further evaluation. At this point, it should be reiterated that the experimental determination of metastable limits dependends on experimental settings like cooling rate or stirring speed. Thus, metastable limits are always subject to uncertainty. In Figure 4.6 (a), the resulting metastable limit calculated with theoretical examination from experimental data is displayed at 20°C.

The metastable zone (marked in green) defines the regions in the triangular diagrams where spontaneous nucleation is unlikely. In order to verify the determination procedure, evaporation experiments were conducted (compare Appendix A.6). Saturated solutions were supersaturated isothermally through drying. The mean drying rate depended on solution composition and was in the range of 0.001 - 0.009 g min^{-1}. It was calculated with the change in mass over the process time. These were achieved with maximum possible nitrogen flux. Thus, no higher drying rates could be reached. In Figure 4.6 (b), compositions are marked with black stars when crystallization was observed.

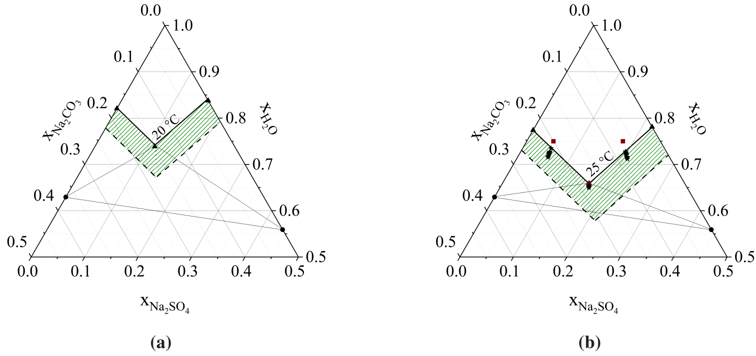

Figure 4.6: In Diagram (**a**), the metastable zone is marked with dashed green area. It resulted from theoretical considerations (using Equation 4.1 with Equations 4.2a and 4.2b) and experimental investigation of ΔT_{met} at a saturation temperature of 20°C. In Diagram (**b**), nucleation points of drying experiments for verification of the metastable zone at 25°C are marked with black stars. In total 15 solutions were investigated. All lie within the metastable zone. Initial compositions are marked with brown squares.

Upon reaching nucleation point, drying was stopped. The solution was weighed to obtain the reduced mass. With the assumption that only water evaporated, it was possible to determine final compositions. The three initial compositions were always equal and are represented by the brown squares. Other than expected, all solutions crystallized within the metastable zone. Even very low supersaturation was sufficient to induce nucleation. However, applied drying rates were the maximum achievable with the experimental set-up. To compare supersaturation generation of drying with cooling, it is necessary that drying rates are comparable to cooling rates. Taking again Equation 4.1 and setting Δx_i to $\dot{x}_i$ and ΔT to $\dot{T}$, the relation between both can be described by the derivative of the solubility curve. Hence, the corresponding cooling rate of 0.001 - 0.009 g min^{-1} would be in the range of 0.002 - 0.01 K min^{-1}. The solutions were not supersaturated appropriately to compare both results. Due to the far lower supersaturation rate, the solution had more time to build nuclei which is why earlier nucleation could be observed. Technically, it was not possible to apply lower cooling rates than 0.01 K min^{-1}. Experiments with this cooling rate brought similar results compared to 0.1 K min^{-1} (compare Diagrams (c) and (e) in Figure A.10 in Appendix A.8). Thus, it would be of interest if experiments with higher drying and supersaturation rates would lead to similar metastable zones.

Heterogeneous nucleation

For layer growth on substrates, heterogeneous nucleation is of higher interest than homogeneous. The substrates component would grow anyway. Foreign substances have to build nuclei prior to growth which would be more probable on a crystalline layer than in clear solutions. Hence, heterogeneous nucleation will be the dominant mechanism. The influence of other entities on nucleation depends on crystal structure and chemical functionality. In case studies and later on in experiments, only the two materials Na_2SO_4 and Na_2CO_3 dissolved in water are considered. It is not possible to investigate the heterogeneous influence on nucleation behavior of one to the other electrolyte. If a solution would be supersaturated with respect on sodium sulfate, but not on sodium carbonate, additional sodium carbonate would dissolve. Thus, other materials should simulate the behavior of the used electrolytes.

In several studies on sodium sulfate decahydrate nucleation, borax was used as an effective nucleation driver. Due to the similar crystal structure between sodium carbonate decahydrate and sodium sulfate decahydrate, it was assumed that borax would also improve nucleation of carbonate. Based on the results from homogeneous nucleation, metastable zones were investigated in presence of borax particles. Other than for homogeneous nucleation, experiments were conducted isothermally with a known composition and thus, supersaturation. In Figure 4.7, all evaluated solutions are marked with stars and squares.

All solution compositions were investigated three times. In case no crystallization was observed in an induction time range of two hours, the composition is marked with a square. In contrary, stars show crystallized compositions during induction time. The metastable zone limit was set in between a solution that did not yet crystallize (square) and the solution that built nuclei (star). As was expected from literature, borax is an excellent nucleation driver for sodium sulfate. The metastable zone limit lay very close to the solubility line. All solutions crystallized

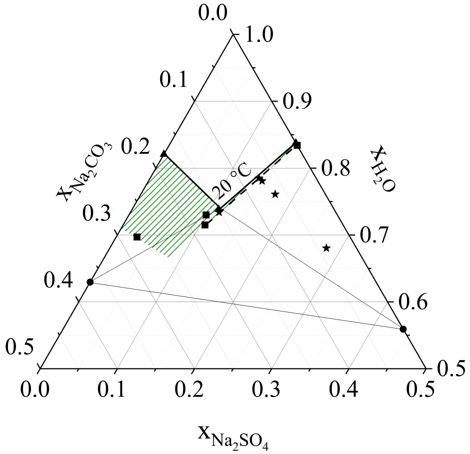

Figure 4.7: Green dashed area displays the metastable zone from heterogeneous nucleation experiments with borax seeds. Black squares represent non-crystallized compositions whereas black stars show compositions which crystallized within two hours. Metastable zone limit lies close to the solubility line of sodium sulfate. On the carbonate side, it was not possible to detect it. No crystallization occurred.

within two hours with exception of saturated solutions. Hence, sodium sulfate crystallization is strongly accelerated by the addition of small amounts of borax. In contrast, sodium carbonate was not affected in any way by the addition of the same amount. Even at higher supersaturation with respect to sodium carbonate, no nucleation could be observed. Also, two ternary compositions did not crystallize. The three points beneath eutectic point were chosen with respect to the elongation of both solubility lines. The squares on the left represent points which lie above the elongation of sodium sulfate solubility line, whereas the star lies below both elongations. These experiments show strikingly that sodium sulfate decahydrate crystallized upon slight supersaturation even at higher carbonate mass fractions. On the contrary, sodium carbonate decahydrate did not crystallize in any case in presence of borax. Hence, the low lattice mismatch did not improve nucleation.

The example of borax shows that even similar components could act differently. If borax would be taken as a substrate material, only sodium sulfate would crystallize and carbonate would remain dissolved. At some point, carbonate would crystallize onto the pure layer of sodium sulfate. Hence, the metastable limit would generate a stratified solidification. For a complete understanding of the imagined case, heterogeneous nucleation of sodium carbonate in presence of sodium sulfate would be needed. This is not realistic to achieve due to the solubility as explained earlier. Besides intended stratification in product development, the investigations provide new data for fouling prevention or material separation. The example of borax shows an excellent agent, which is able to accelerate crystallization of one component while the other and even similar component still stays in solution. If both components are not influenced or even inhibited by a certain solid, this component could be used hypothetically be used as tube coating in a heat exchanger to prevent fouling. With respect to the prevailing material system, calcite would represent such a component. In several experiments, no crystallization could be observed with suspended calcite particles. In Figure 4.8, experimental data is shown.

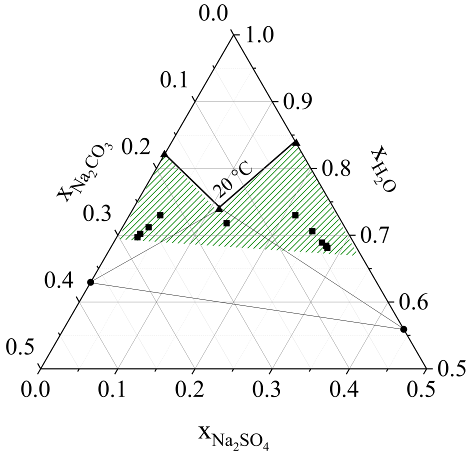

Figure 4.8: Green dashed area displays the metastable zone from heterogeneous nucleation experiments with calcite seeds. Black squares represent non-crystallized compositions within two hours. A definite boundary of the metastable zone cannot be drawn, since no crystallization occurred in any experiment.

All points are displayed as squares which indicates that no crystallization was observed. Hence, calcite inhibits or at least does not affect nucleation of both components in the actual arrangement. Whether this component would be a suitable coating material would need to be evaluated in comparison to conventional pipe materials such as stainless steel.

Secondary nucleation

A crucial nucleation mechanism of layer formation from solutions is secondary nucleation. Logically, abrasion is not of interest but the presence of crystalline solids of crystallizing materials. Due to the contact of a substrate, secondary nucleation is possible. In order to analyze secondary nucleation, the experimental set-up of heterogeneous nucleation was used but with a single crystal composed of one of the solution components. This should simulate the presence of a substrate. Solutions were supersaturated and a particle was inserted on a fixed position. The solution was stirred to homogenize it. At different compositions, crystallization behavior was observed. In Figure 4.9, the results are displayed. All points represent a series of three independent experiments.

If new nuclei were formed, again stars represent the composition. Points marked in blue were seeded with sodium sulfate decahydrate particles and points marked red with sodium carbonate decahydrate particles. As can be seen, even slightly supersaturated solutions built new particles regardless of the seeding agent and the position in the triangular diagram. In Figure 4.10, exemplary photographs of nucleated solutions are shown.

At first, nuclei built a cloud-like agglomerate in the vicinity of the seed particle. From observations it was clear that nucleation took place and not dendritic growth. Single particles were clearly distinguishable by eye. At higher supersaturations and with longer times, particles were suspended into solution.

The results show that even low supersaturations are sufficient to induce nucleation of both components. This has to be considered in other experimental set-ups of this work. Also, it shows that crystals will not solely grow at low supersaturations but build new nuclei even without abrasion.

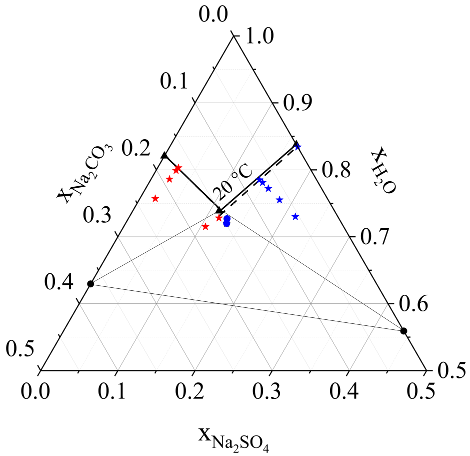

Figure 4.9: Triangular diagram with marked compositions from secondary nucleation experiments. Blue stars represent observed nucleation events in all repetitions within two hours. Compositions marked with blue dots did not crystallize in every repetition. Metastable zone limits lie both very close to the solubility lines.

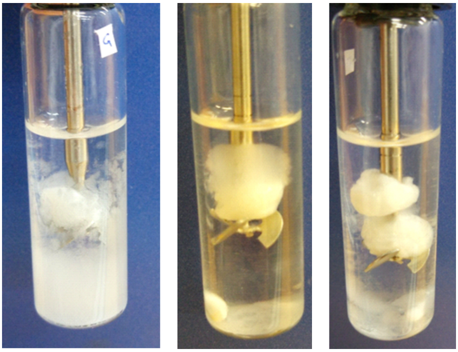

Figure 4.10: Photographs after secondary nucleation are shown (taken from master thesis of Michaela Gratzfeld). The single seed crystal was located on the white plateau which lies above the propeller. The picture on the left shows a high number of nuclei which were built in the entire solution. In the middle, only a cloud-like conglomerate was observable in the vicinity of the seed crystal. The picture on the right shows an example of distribution of the cloud conglomerate into the entire volume over time.

4.1.3 Conclusion

Hypothesis I - Metastable zones of ternary systems can be predicted by a pseudo-binary approach - cannot be supported completely. It has been shown to be capable of determining the metastability limits for homogeneous nucleation with a small amount of time. However, it was not possible to verify the estimated limits by drying experiments. Nevertheless, the determined limits were considered for further metastability studies and proved to be an adequate basis.

In terms of layer formation on crystalline substrates, only heterogeneous and secondary nucleation are of greater interest. Homogeneous nucleation will not occur since solid materials - foreign or own - are always present. Nevertheless, homogeneous nucleation and its resulting metastable zone limits are necessary to define relevant parameter ranges for the investigation of other mechanisms. Experiments on heterogeneous nucleation showed that seed crystal selection has a great impact on nucleation behavior. In terms of stratification behavior, it would have been interesting to see how the two electrolytes Na_2SO_4 and Na_2CO_3 interacted as heterogeneous nuclei. Since this evaluation was not possible because of the solubility behavior, another heterogeneous seed was chosen. Borax crystallizes in the same crystal system and has similar lattice parameters. Sodium sulfate decahydrate crystallized even at low supersaturations whereas sodium carbonate decahydrate was not affected at all in its crystallization behavior. Even at the metastable zone limit of homogeneous nucleation, no crystallization event was observed. Furthermore, it could be shown that this behavior can be transferred into the three phase area beneath the eutectic point of the triangular diagram. Virtual extensions of the solubility lines showed that solutions above sodium sulfate solubility would not crystallize even though they were supersaturated with respect to carbonate. The positive influence of borax on sodium sulfate decahydrate can be compared with the seeding behavior in secondary nucleation experiments. Hence, borax induces crystallization of sodium sulfate as well as sodium sulfate decahydrate itself even in presence of carbonate ions. This specific behavior would generate stratified solid layers. First, the preferred component - sodium sulfate decahydrate - would solidify. Due to that, the other component - sodium carbonate decahydrate - supersaturates more and more and at some point it would cross metastable zone limit. The result would be two pure layers. In case one of the crystallizing components, e.g. sodium carbonate decahydrate, were the substrate material and would have the positive influence on the foreign component, the resulting layer would be mostly homogeneous. The one component would grow and the other would build nuclei rapidly.

Secondary nucleation is foremost essential for further experimental design. The experiment was chosen to simulate the nucleation induction of a present solid entity which is also dissolved. This is similar to a substrate in contact with a layer. From these experiments, it is evident that at low supersaturations not only growth but also nucleation occurs. This is important for the design of experimental growth studies. Nucleation events must be prevented at all times. Therefore, the initially set supersaturation should not cause nucleation, but only growth. It is also important for conducting drying experiments of thin films in contact with a substrate. The highest supersaturations likely occur at the gas-liquid interface because the solvent is displaced by drying. If nuclei are produced at this position, growth would lead to a cover layer on the fluid. This would prevent further drying which is also not intended.

In addition to stratification behavior, these experiments give the opportunity to evaluate components on their selectivity or inhibition behavior. On the one hand, material separation processes can be easily adapted. On the other hand, unintentional crystallization such as fouling could be prevented if tubes are coated with a material showing inhibiting behavior or if specific inhibiting ions are added.

4.2 Growth parameters in multi-component solutions

In this section, Hypothesis III - Kinetics of multiple crystallizing materials can be measured simultaneously and independently - will be examined. In order to do so, requirements for a measurement technique of multi-component crystal growth kinetics are enumerated. Possible techniques, theoretical drawbacks, and necessary assumptions are summarized. At the end, the developed method is presented. The principal experimental set-up was developed together with Andreas Roth in his master thesis.

There are two classical methods to determine crystal growth rates from solution. (i) Measuring the change in size of a particle or surface. (ii) Tracking the concentration change in solution - known as desupersaturation [Garside et al., 2002]. As already stated in Section 2.1, there are many experimental approaches to track crystal growth kinetics of single components. Also, it is known that additives influence crystal growth. Nevertheless, the simultaneous growth of multiple components is not investigated so far. Therefore, a new method has to be found to measure crystal growth rates of concurrent crystallizing materials. The requirements for the method are: (a) Nucleation processes must be suppressed. (b) Growth location must be well defined. (c) The growth of each component must be distinguishable. To meet these, only the second (ii) of the two principal methods - namely desupersaturation - is appropriate. If the change in size of a particle would be measured, it could not be distinguished between the components. Mostly, desupersaturation was applied in a set-up of suspension crystallizers [Cornel et al., 2008; Cornel and Mazzotti, 2009; Vavouraki and Koutsoukos, 2012, 2016; Glade et al., 2004]. The disadvantage of the system is that many particles exist, making requirement (b) difficult to accomplish. Also, requirement (a) is not easy to meet since nucleation could occur due to of abrasion in a stirred suspension. Hence, a defined surface with a thin supersaturated film in contact would be suitable. A schematic drawing of this approach is depicted in Figure 4.11.

The mass transfer and inverse crystal growth rate depend on the concentration gradient in the fluid. It is assumed that equilibrium conditions for the crystallizing component prevail at the solid-liquid interface ($c_{i,ph} = c_i^*$). The gradient in the film depends on the limitation of the process. If diffusion of the ions is limiting, the solid line gradient occurs. If the integration into the substrate limits mass transfer, the dashed gradient develops [Mersmann, 2001]. To obtain growth kinetics and hence, the variables $k_{d,i}$, $k_{g,i}$, $k_{r,i}$, g and r from Equations 2.10, crystal growth and dissolution experiments have to be conducted. The diffusion mass transfer coefficient of component i $k_{d,i}$ may be analyzed from dissolution experiments, because dissolution can be assumed diffusion limited [Mullin, 2001]. All other variables have to be determined from crystal growth experiments.

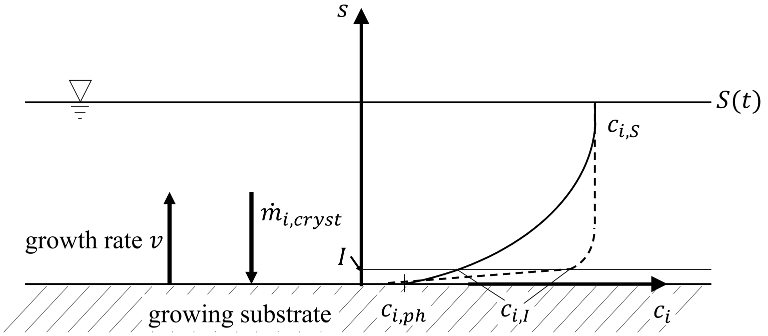

Figure 4.11: Schematic depiction of the proposed set-up. A supersaturated film with a thickness of $S(t)$ stays in contact with a growing substrate. The mass transfer of components i $\dot{m}_{i,cryst}$ causes crystal growth v. Growth rate as well as mass transfer depend on the concentration gradient in the liquid. The developing gradient itself depends on the limiting transfer step. If diffusion process is limiting then the gradient follows the solid line. If integration into the substrate is limiting then the dashed gradient occurs.

It is assumed that a measurement of the concentration at the gas-liquid interface - indicated with $c_{i,S}$ - is sufficient to calculate growth rates and hence, kinetic parameters. In Section 4.2.1, this assumption is fortified with numerical calculations. Also, heat-mass-transfer analogy can be used for justification. A short summary is given in Appendix A.2.

To analyze the change in concentration, an analytical tool is necessary which can distinguish between various materials. In principle, all spectroscopic methods are applicable for this purpose. The selection of a suitable method depends on the material system. For example, if water is used as a solvent, IR spectroscopy would be a poor choice because the IR activity of water is very high and overlaps with IR signals of other species [Goulden, 1959]. In case of water, Raman spectroscopy is a good option [Lilley, 1973]. Not only the solvent but also the solutes have to respond to the applied spectroscopic method. This makes the choice of the analytical tool very important. The material system used in this work - aqueous solution of Na_2SO_4 and Na_2CO_3 - allows Raman spectroscopic analysis. Since both substances have a common sodium ion, only the anion concentrations SO_4^{2-} and CO_3^{2-} have to be followed. This allows to correspond the change in anion concentration in the thin film with growth of the respective solid entities as can be seen from the chemical reaction equations (Equation 4.3 a and b).

$$2\mathrm{Na}^{+} + \mathrm{SO}_4^{2-} + 10\mathrm{H_2O} \rightleftharpoons \mathrm{Na_2SO_4} \cdot 10\mathrm{H_2O} \tag{4.3a}$$

$$2\mathrm{Na}^{+} + \mathrm{CO}_3^{2-} + 10\mathrm{H_2O} \rightleftharpoons \mathrm{Na_2CO_3} \cdot 10\mathrm{H_2O} \tag{4.3b}$$

In the investigated temperature range (17 - 23.5°C) only sodium sulfate decahydrate and sodium carbonate decahydrate occur (compare Figure 4.1).

4.2.1 Multi-component diffusion simulation

To justify the experimental approach, one-dimensional diffusion simulations are conducted. The simulations shall shed light on the question what time resolution is necessary to measure crystallization kinetics in thin films. Also, the assumption of single-point concentration measurements shall be evaluated. For this purpose, simulations of concentration profiles and resulting mass transfer coefficients $k_{g,i}$ are analyzed with regard to a possible experimental evaluation in a thin film.

In Figure 4.12, phase transfer flux $\dot{n}_i$, mass transfer coefficient $k_{g,i}$, and concentration difference $\Delta\tilde{x}_i$ are plotted over time exemplarily. Through Equation 2.10c all variables are connected to each other.

In every crystallization process, the variables would follow the displayed characteristic evolution. Only the time ranges would change. The course of all variables in Figure 4.12 can be divided into two phases. The deciding variable is the mass transfer coefficient $k_{g,i}$. As can be seen, at a certain time it takes a steady-state value. Up to that point, the mass transfer flux $\dot{n}_i$ is dictated mostly by the changing mass transfer coefficient (phase I). Afterwards, mass transfer is mostly determined by the concentration difference $\Delta\tilde{x}_i$. It is the aim of the measurement technique to identify the constant mass transfer coefficient at long times. Therefore, phase I should be short and phase II should be present at the most part of the experiments. The short- and long-term behavior can be compared with transient one-dimensional heat conduction [Stephan et al., 2019]. The analogy is shown in Appendix A.2.

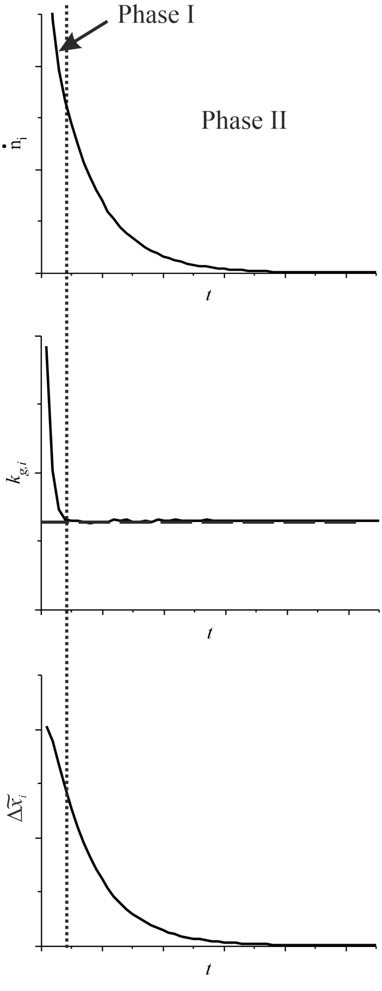

Figure 4.12: Exemplariy plots of mass flux $\dot{n}_i$, mass transfer coefficient $k_{g,i}$, and mass fraction difference $\Delta\tilde{x}_i$ over time show a separation in two phases. It is distinguished by the behavior of $k_{g,i}$. Once it takes a constant value, phase II prevails.

Model set-up

A thin film in contact with a substrate forms the simulation environment. It is discretized with an Eulerian frame so that the mesh is fixed at all times. A type of VoF-method (Volume of Fluid) is applied so that the growth of the substrate is incorporated in the modeling framework [Hirt and Nichols, 1981]. At the beginning, all cells are filled with a supersaturated solution and then brought in contact with the substrate. The substrate grows with an integration kinetic following Equation 4.4.

$$\dot{n}_{i,cryst} = k_{r,i} \cdot (c_{i,\mathrm{C}+1} - c_i^*) \tag{4.4}$$

The substrate grows with the molar flux $\dot{n}_{i,cryst}$ into cell C, which is why the volume fraction of solution decreases in this cell. If a cell is fully occupied with solid material, its concentration is set to equilibrium conditions so that no flux constraint applies. A more in-depth explanation of the moving boundary can be found at the end of this section. It is assumed that solution and solid densities are equal. Hence, no volume changes occur due to phase transition and convection can be neglected. In the rest of the cells, the continuity equation (Equation 2.13) prevails. Fick's equation is used for the description of the diffusional flux. Gupta et al. [2019] showed that this approach is feasible to describe the diffusion of similar material systems. In their publication, they compared the pore diffusion of different electrolytes. One electrolyte is present in a pore and another in the bulk which stays in contact. They simulated and experimentally measured the diffusion processes of the participating ions. The considered material systems always had a common cation Na^+ and two different anions. This compares well to the material system in this work. They compared simulations with and without cross diffusion effects. If the diffusivities of the ions are similar then, cross diffusion effects can be neglected and each ion flux can be treated independently. Therefore, the following Fickian equation is taken to model the material transport (Equation 4.5).

$$\vec{\dot{n}} = \mathbf{D} \cdot \nabla \vec{c} \tag{4.5}$$

In Helfenritter and Kind [2022b], it was shown that the consideration of cross diffusional effects are neglectable in the case of the model material system. Hence, the interacting diffusion coefficients of dissolved material are set to zero ($D_{ij} = D_{ji} = 0$). The diffusion coefficients are calculated from self-diffusion coefficients taken from literature or NMR-measurements (Appendix A.7). First, Maxwell-Stefan coefficients are determined with the Darken relation (Equation 2.18).

Kim and Srinivasan [2016] showed that the relation is also valid for electrolytic systems. The coefficients from Equation 2.18 can be multiplied with a thermodynamic correction factor to obtain the Fickian diffusion coefficient (Equation 2.16). To determine the factor, activity coefficients of carbonate and sulfate ions were calculated with PhreeqC for solution mixtures that contain molar fractions of sodium sulfate and sodium carbonate in the ranges of $0.011 < \tilde{x}_{\mathrm{Na_2SO_4}} < 0.022$ and $0.012 < \tilde{x}_{\mathrm{Na_2CO_3}} < 0.031$, respectively. In this range, the function of the natural logarithm of the activities can be linearized as a function of the molar fractions (compare Figure 4.13).

With this, the derivative in Equation 2.17 is a constant and equals the inclination. In Equation 4.6, these constants are shown as the factors of the molar fractions.

$$\mathbf{\Gamma_{ij}} = \begin{bmatrix} 1 + \tilde{x}_1 \cdot 10.461 & \tilde{x}_1 \cdot -11.021 \\ \tilde{x}_2 \cdot -7.995 & 1 + \tilde{x}_2 \cdot 8.813 \end{bmatrix} \tag{4.6}$$

It is assumed that electroneutrality is valid at all times and that the ions diffuse as ion pairs. Thus, the diffusion of sodium ions is linked to their anions and will not be modeled. This makes it possible to define the transport of sulfate and carbonate ions to the transport of the dissolved electrolytic molecule, either Na_2SO_4 or Na_2CO_3.

The space is divided into $M = 1000$ equal cells with a width of $\Delta s = 1.5 \cdot 10^{-7}$ meters. The time steps are set to $\Delta t = 10^{-6}$ seconds. The explicit method is used to solve the equations. The process is assumed to be isothermal at 20°C to provide the driving force. The initial solution is saturated at 25°C. In Figure 4.14, the simulation scheme is depicted.

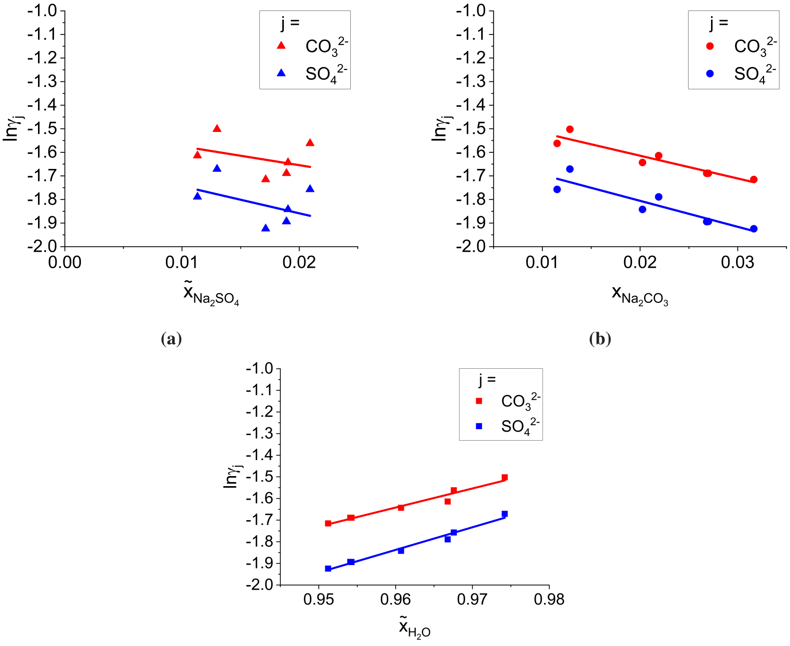

(a) **(b)**

(c)

Figure 4.13: Calculated activities of aquoeous solutions containing sodium sulfate and sodium carbonate in the molar fraction range of $0.011 < \tilde{x}_{\mathrm{Na_2SO_4}} < 0.022$ and $0.012 < \tilde{x}_{\mathrm{Na_2CO_3}} < 0.031$. In Diagram (**a**), the natural logarithm of $CO_3{}^{2-}$- and $SO_4{}^{2-}$-activities are depicted as a function of sodium sulfate molar fraction. Similarly, Diagrams (**b**) and (**c**) show the dependence of the activities from sodium carbonate and water molar fractions, respectively. In this concentration range, the dependence of $ln\gamma_j$ from x_i can be approximated with a linear function.

The boundary conditions of the cell in contact with the substrate (m = C) are as follows: The cell in contact with the solid is a virtual cell, which provides the phase transfer flux (Equation 4.4). The concentrations of crystallizing components are set to equilibrium conditions. Other concentrations are adjusted so that no flux condition prevails between the cell in vicinity of the substrate (m = C) and the first real fluid cell (m = C + 1). In case of a solely crystallizing ansolvate, the

$m = M$	$c_i(t, m = M) = c_i(t, m = M - 1)$
⋮	
⋮	
$C < m < M$	$\frac{d\vec{c}(t,m)}{dt} = \boldsymbol{D} \cdot \frac{d^2\vec{c}(t,m)}{ds^2}$
⋮	
⋮	
$m = C$	$c_{i,\text{cryst}}(t, m = C) = c_{i,eq}$, $\dot{n}_{i,\text{cryst}} = k_{r,i} \cdot (c_{i,C+1} - c_{i,C})$ others: no flux condition

Figure 4.14: Simulation scheme of the liquid film with the prevailing equations and boundary conditions.

compositions of the other components in the fluid cell are adapted according to Equation 4.7.

$$\frac{\tilde{x}_2(t)}{\tilde{x}_3(t)} = \frac{\tilde{x}_2(t + \Delta t)}{\tilde{x}_3(t + \Delta t)} \tag{4.7}$$

It is assumed that the proportions of components 2 and 3 are equal from one to another time step. At the beginning, the cell in vicinity of the solid is set to C = 1. Due to the growing solid, the solid-liquid interface is not static but moving. The liquid fraction in the vicinity cell can be expressed in terms of length scales according to Equation 4.8.

$$\alpha = \frac{\Delta s_{\mathrm{C}}}{\Delta s} \tag{4.8}$$

The volume fraction α is known from Volume-of-Fluid theory [Hirt and Nichols, 1981]. The change in total liquid film thickness s is calculated at each step with Equation 4.9.

$$\frac{\partial s}{\partial t} = \frac{\sum \dot{n}_{i,cryst} \cdot \tilde{M}_i}{\rho^S} \tag{4.9}$$

Due to the moving boundary, the change in total thickness equals the change of the vicinity cell thickness (Equation 4.10).

$$\Delta s_{\mathrm{C}}(t+\Delta t) = \Delta s_{\mathrm{C}}(t) - \frac{\Delta s}{\Delta t} \tag{4.10}$$

Due to the virtual nature of the vicinity cell and the rather high spatial resolution, it is assumed that the change of Δs_{C} has no influence on mass fluxes. If $\Delta s_{\mathrm{C}} < 0$, the vicinity cell with its conditions will transfer from m = C the cell above (m = C + 1). All other cell properties will remain as before.

The boundary at the top is defined with no flux condition. Initial concentrations are set so that they are comparable with experiments. Also, equilibrium conditions are set realistically.

Simulation results

There are three possible cases to discuss in ternary growth processes. Firstly, a component crystallizes alone as a non-solvate. Secondly, a single solvate is built. Lastly, both electrolytic components crystallize. In the latter case, the equilibrium concentrations are assumed to be independent of the number of solvate molecules, only the phase transfer currents are different due to the solidifying solvent. The diffusion of the molecules will be treated independently. Self-diffusion coefficients of carbonate and sulfate ions are assumed to be equal and constant in the simulated concentration range. Because of electroneutrality, the salts are assumed to diffuse as an ion pair. Self-diffusion coefficients of carbonate and water in the prevailing concentration range were determined with NMR-diffusion measurements. The results can be looked up in Appendix A.7. At high electrolytic concentrations, rather low values of water diffusivity were achieved. The original self-diffusion coefficient of pure water is $D_{\mathrm{H_2O}} = 2.6 \cdot 10^{-9}\ \mathrm{m^2s^{-1}}$ at 25°C [Wang, 1965]. It is assumed that the self-diffusion coefficient of sulfate ions assumes values similar to those of carbonate ions. Nielsen et al. [1952] determined the self-diffusion coefficient of sulfate ions to slightly higher values of $D_{\mathrm{Na_2SO_4}} = 6 \cdot 10^{-10}\ \mathrm{m^2s^{-1}}$ at high concentrations (3 mol $\mathrm{L^{-1}}$). The self-diffusion coefficients used here are $D_{\mathrm{Na_2SO_4}} = D_{\mathrm{Na_2CO_3}} = 3 \cdot 10^{-10}\ \mathrm{m^2s^{-1}}$ and $D_{\mathrm{H_2O}} = 1 \cdot 10^{-9}\ \mathrm{m^2s^{-1}}$. The initial composition of all simulations were $\tilde{x}_{\mathrm{Na_2SO_4}} = 0.029$, $\tilde{x}_{\mathrm{Na_2CO_3}} = 0.043$, and $\tilde{x}_{\mathrm{H_2O}} = 0.928$. The equilibrium molar fraction of sodium sulfate is assumed to be $\tilde{x}^*_{\mathrm{Na_2SO_4}} = 0.019$ for sole crystallization of sodium sulfate as anhydrate or hydrate. If both electrolytic components crystallize, equilibrium is described by $\tilde{x}^*_{\mathrm{Na_2SO_4}} = 0.018$ and $\tilde{x}^*_{\mathrm{Na_2CO_3}} = 0.033$. To obtain steady-state phase transfer coefficients, it is crucial that the majority of the process takes place in phase II. In phase II, the process is mostly dictated by the concentration difference between the point at the measurement position and at the solid-liquid interface. The mass transfer coefficient of the integration process $k_{r,i}$ is not dependent on the overall concentration difference but on the difference at the virtual interface. If the diffusion mass transfer coefficients are larger than the integration coefficients, the concentration difference between the virtual interface and the measurement point would decrease faster than at the integration interface. Thus, reducing the integration coefficient would result in longer process times, but the concentration at the measurement point would still be affected early. Therefore, Phase II would be reached earlier in any case compared to the overall process duration. This is why only diffusion limitation will be covered here. The reaction constant at the solid liquid interface is set to $k_{r,i} = 7 \cdot 10^{-3}$ m s^{-1} for all crystallizing components. This value is used to simulate a reaction resistance that has a similar order of magnitude compared to the diffusion resistance in the film ($D_{ii}/\Delta s \approx 7 \cdot 10^{-3}$ m s^{-1}). In Figure 4.15, the concentration evolution in the vicinity of a growing surface of the components sodium sulfate (a), sodium carbonate (b), and water (c) are depicted. The molar fraction of each component in the liquid film is plotted over the distance from the surface. Diagram (d) shows the resulting mass transfer coefficients over time, which were calculated with Equation 2.10c. At each time step, exponent g was assumed to be one, the concentration difference at positions 0.15 mm and 0 mm and the calculated phase transfer flux (Equation 4.4) were considered.

The varying line styles correspond to the aforementioned possible cases of multi-component crystallization. Anhydrous crystallization of sodium sulfate is depicted with solid lines, crystallization of sodium sulfate decahydrate with dashed lines and concurrent anhydrous crystallization of sodium sulfate and sodium carbonate with dotted lines. First, $\mathrm{Na_2SO_4}$ in Diagram (a) is examined in detail. The initial concentration of 0.029 diminished rapidly close to the substrate for all cases. Immediately, a spatial gradient developed into the entire liquid film. At the time of five seconds, the concentration at 0.15 mm diminished from its initial value. Afterwards, the courses of the three cases do not change significantly

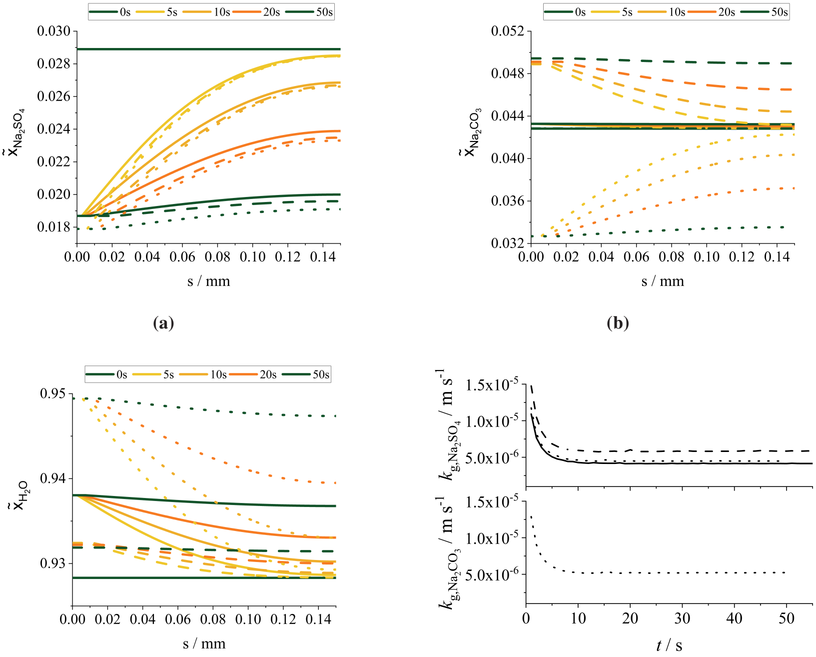

(a)

(b)

(c)

(d)

Figure 4.15: (**a**)-(**c**): Concentration gradients over space of Na_2SO_4, Na_2CO_3, and H_2O, respectively. Solid lines represent simulations of Na_2SO_4 crystallizing as an anhydrate. Dashed lines depict the case of crystallization of sodium sulfate decahydrate. Two components crystallizing as anhydrates are shown as dotted lines. (**d**): The diagrams shows all mass transfer coefficients of the simulated cases over time. Line shapes are chosen comparably to Diagrams (**a**)-(**c**).

at the farthest point. Also, the spatial gradient develops similarly. Anhydrous crystallization is slower compared to the others and hence, reaches equilibrium later. Even though equilibrium concentration of simultaneous growth is lower, its process does not take significantly longer than the single anhydrous case.

Na_2CO_3 and H_2O show a completely different behavior. If sodium sulfate crystallizes as an anhydrate (solid lines), the change in concentration of Na_2CO_3 is small and not detectable in the scale of the diagram. The course is similar to the course of component H_2O in this case. Due to the solidification of sodium sulfate, the others level up and reach equilibrium at higher concentrations of $\tilde{x}_{\mathrm{Na_2CO_3}} = 0.044$ and $\tilde{x}_{\mathrm{H_2O}} = 0.937$. In case of sodium sulfate crystallizing as a decahydrate, the enrichment of sodium carbonate increases further. Na_2SO_4 and H_2O transfer to the solid which leads to a final molar fraction of sodium carbonate of $\tilde{x}_{\mathrm{Na_2CO_3}} = 0.049$. Logically, water does not enrich as it does in the first case. But still, it reaches $\tilde{x}_{\mathrm{H_2O}} = 0.932$. If both components crystallize as anhydrates, the course of sodium carbonate equals the one of sodium sulfate. This is because of similar growth and diffusion kinetics. As a result, the enrichment of water increases to the value of $\tilde{x}_{\mathrm{H_2O}} = 0.949$.

Comparing the overall mass transfer coefficients over time in Diagram (d), it is obvious that all lie in similar orders of magnitude. Most importantly for the measurement of steady-state mass transfer coefficients, phase II is reached very early. At the latest, it took 10 s in case of single and multiple anhydrous crystallization in comparison with process times greater than 50 s. It can also be noted that the mass transfer coefficient of sodium sulfate assumes similar values ($k_{g,\mathrm{Na_2SO_4}} = 4 \cdot 10^{-6}$ m s^{-1}) under the conditions studied, regardless of whether it crystallizes as a single component or together with sodium carbonate (compare solid and dotted lines in Diagram (d)). The steady-state mass transfer coefficients of the crystallizing decahydrate lie at $k_{g,\mathrm{Na_2SO_4}} = 6 \cdot 10^{-6}$ m s^{-1}. The resulting mass transfer coefficient of component 2 in the last case is $k_{g,\mathrm{Na_2CO_3}} = 5 \cdot 10^{-6}$ m s^{-1}.

Since phase II is dominant in all three cases, it can be concluded that the proposed measurement of a single point in the film is appropriate for kinetic analysis. From it, constant mass transfer coefficients can be retrieved in experiments. Other case studies on influencing factors such as different diffusion coefficients, integration limitation and solvation numbers can be seen in the publication Helfenritter and Kind [2022b].

4.2.2 Methodology

For the kinetic measurements of dissolution and crystal growth, a liquid thin film of 150 µm thickness is put on a microscopic glass (thickness: 0.145 ± 0.015 mm, Zitt-Thoma GmbH) inside a tempered stainless steel body (depicted in Figure

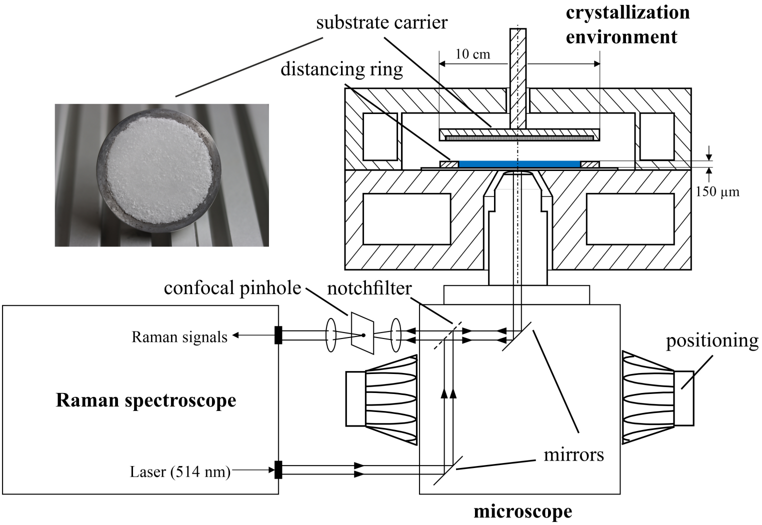

Figure 4.16: Depiction of the experimental set-up. The upper part is the crystallization environment to which the Raman spectroscope is connected with an objective. The principal idea is adapted from Müller et al. [2009]

4.16). An inverse confocal micro Raman spectroscope is added to measure multi-component crystal growth kinetics. The set-up meets all aforementioned requirements for a multi-component crystal growth experiment. (a) With low supersaturation of at maximum 3 K, nucleation processes are suppressed. (b) A tabletted substrate defines the sole growth location. (c) Raman spectroscopy is able to distinguish between several components [Scharfer et al., 2007; Ludwig et al., 2007; Nijdam et al., 2015].

Experimental setting

The crystallization environment is composed of a tempered stainless steel body, a distancing ring of about 150 µm which confines the fluid, and a substrate carrier. The temperature is set through a thermostat (Lauda RC6). The set-up is aligned with the work of Müller et al. [2009]. The substrate carrier is made of aluminum and carries a tablet of one of the salts to be analyzed. Through an opening in the middle of the body, a microscopic objective (Zeiss EC "Plan-Neofluar" 100x/1.3 Oil) is inserted. It stays in contact with the glass through an immersion oil (Zeiss, Immersol 518 N). A laser with a wavelength of 514 nm is focused at the edge of the liquid film. The focus point is set in order that the edge of the illumination volume just reaches the microscopic glass. Thereby the highest intensity is achieved. The focus volume has a diameter of 10 µm. The center is placed five µm away from the microscopic glass. This corresponds with a distance of 145 µm from the substrate. A confocal pinhole with a diameter of 400 µm ensures spatial resolution. The scattered light from the crystallization environment returns through the objective and is directed onto a notch filter. All light with the laser's wavelength is rejected. The remaining light is guided onto the confocal pinhole so that only the light from the focus point transmits. Afterwards, a slit of 300 µm ensures that no light from the surrounding could enter the spectrograph. A monochromator splits the scattered light and a CCD-camera counts the photons.

To correlate the obtained spectra with prevailing concentrations in the liquid, a calibration is needed. The Raman intensity of a species i I_i is defined with Equation 4.11.

$$I_i = \frac{\partial \sigma_i}{\partial \Omega} \cdot c_i \cdot N_A \cdot V \cdot \Omega_{\text{obs}} \cdot F^{-1} \cdot C \cdot I_0 \tag{4.11}$$

The intensity is linearly dependent on the concentration of species i c_i. Also, it is a function of the differential scattering cross area $\frac{\partial \sigma_i}{\partial \Omega}$, which contains spectral properties at a certain wavelength. All other parameters are not material-specific but constant for a spectrum. Avogradro number N_A is a natural constant. Volume of investigation V, observation angle of the objective Ω_{obs}, the projection area of the detector hole on the volume of investigation F, an efficiency constant of the detector C, and the initial laser light intensity I_0 are experimental set-up parameters. If the intensities of two species are divided and one is defined as a reference material, e.g. water, all constants cancel and Equation 4.12 arises.

$$\frac{I_i}{I_{\text{water}}} = \frac{\partial \sigma_i \cdot \partial \Omega}{\partial \sigma_{\text{water}} \cdot \partial \Omega} \cdot \frac{\tilde{M}_i}{\tilde{M}_{\text{water}}} \cdot \frac{c_i}{c_{\text{water}}} = K_i \cdot X_i \tag{4.12}$$

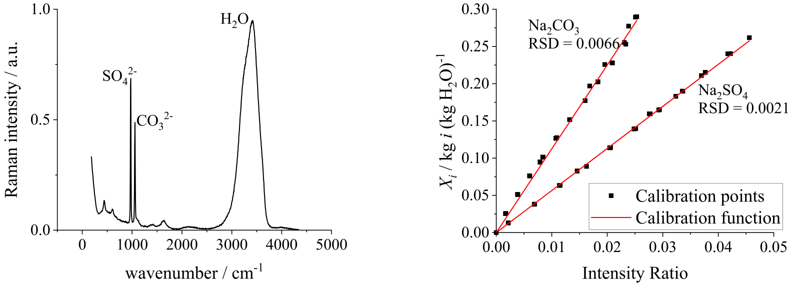

(a) **(b)**

Figure 4.17: (**a**) Raman spectrum of an aqueous solution with mass loads of sodium sulfate and sodium carbonate of $X_{Na_2SO_4} = 0.114$ and $X_{Na_2CO_3} = 0.152$. The prominent peaks can be assigned to the indicated anions SO_4^{2-} and CO_3^{2-} and water. (**b**) Calibration functions of Na_2SO_4 and Na_2CO_3 related to water at 25°C. The slopes of the linear functions represent both calibration factors. The residual standard deviations (RSD) for the calibration functions are given.

It finally results in a linear function of the intensity ratio and the mass load of component *i* with respect to water. The areas beneath each peak are taken as measure of intensity. In Figure 4.17 (a), a Raman spectrum of the prevailing material system is shown. Several spectral results of different solution compositions lead to linear calibration functions for both electrolytes, which are displayed in Figure 4.17 (b).

Generally, Raman spectrums are temperature dependent [Ferraro, 2003]. In the investigated temperature range (17 - 23.5°C), the change is not significant which is why the shown functions are used over the whole temperature range. In Appendix A.5, the detailed calibration procedure is provided.

Before starting an experiment, the temperature is adjusted so that the liquid is supersaturated but metastable with respect to nucleation. At this point, the substrate carrier is not in contact with the liquid. Raman measurements are started at this point to identify the initial solution composition. After at least five minutes, the carrier is carefully put onto the liquid to start the experiment. Raman spectrums are taken with an integration time of five seconds and a laser power of 85 mW.

Sample preparation

The sample carrier is displayed in Figure 4.16 on the top left. A substrate is tabletted into the cavity. Either sodium sulfate decahydrate or sodium carbonate decahydrate is used. The best result in producing a defined and smooth surface is achieved by mixing anhydrous with decahydrate powder in a 50/50 wt-% ratio. This mixture is milled with a mortar and pestle to get a fine particle size ($d_{50,0} = 5$ µm). After pouring approximately 2 grams into the carrier it is compacted with a pressure of 0.8 MN m^{-2} for 60 seconds. For this purpose, a material testing machine is used (10 kN ProLine, Zwick). Then, one gram of a saturated solution is added carefully. The purpose of the wetting is first, to strengthen the adhesive forces between the particles and second, to minimize surface roughness and porosity. Also, it should convert the anhydrous powder to the hydrate form. The pressing procedure is repeated with the same pressure but for 300 seconds. Again, saturated solution is applied to obtain a liquid film on top of the solid. The overlaying solution is absorbed with a paper towel and dried with an air stream. This causes water to be removed and the dissolved substances to crystallize on the substrate surface, closing possible pores.

Data evaluation

As was shown in simulations (compare Section 4.2.1), the concentration evolution $c_{i,S}(t)$ at the point farthest away from the substrate could be taken to evaluate mass transfer kinetics. To evaluate mass transfer coefficients from dissolution and desupersaturation measurements, some assumptions and correlations apply. In experiments, the measured concentration $c_{i,S}$ at position $s(t)$ can also be calculated from mass balances. Therefor the change in solution composition at the measurement point is equalized with the phase change of component *i*. A mass balance of crystallizing component *i* incorporates the assumption (Equation 4.13).

$$\frac{dM_i^L}{dt} = M^L \cdot \frac{dx_i}{dt} + x_i \cdot \frac{dM^L}{dt} = \dot{M}_i \tag{4.13}$$

It is assumed that $M^L \cdot \frac{dx_i}{dt} >> x_i \cdot \frac{dM^L}{dt}$ applies. From all phase transition fluxes, the total mass is adjusted each step (Equation 4.14).

$$\frac{dM^L}{dt} = \sum \dot{M}_i \tag{4.14}$$

Mass fluxes of crystallizing components are associated with growth kinetics (Equation 2.10c) through the following Equation 4.15.

$$\dot{M}_i = A \cdot \tilde{M}_i \cdot \dot{n}_i \tag{4.15}$$

Crystallization order g and mass transfer coefficient $k_{g,i}$ are adapted to the experimental data until the square errors are minimized. In dissolution measurements, g is set to unity while $k_{g,i}$ equals $k_{d,i}$. With Equations 2.10, it is possible to determine $k_{r,i}$ and r from $k_{d,i}$, $k_{g,i}$, and g. In this work, the evaluation of $k_{r,i}$ and r will not be shown. The results can be reviewed in the publication Helfenritter and Kind [2022a]. Nevertheless, the comparison of the variables $k_{d,i}$, $k_{g,i}$, and g will show whether there is a diffusion or integration constraint.

4.2.3 Ternary dissolution

From dissolution experiments, diffusion mass transfer coefficients can be obtained. For this, the general assumption applies that dissolution processes underlie only diffusion constraints (compare Section 2.1). Because crystallization kinetics of multiple components are under investigation, dissolution should also take place in the presence of foreign material. Therefor solutions rich in foreign component and with no content of the evaluated material are brought in contact with a substrate. Under isothermal conditions, the dissolution of the tablet was followed by the increasing concentration in solution. In Figures 4.18 (a) and (b), dissolution courses at 17°C of sodium sulfate decahydrate and sodium carbonate decahydrate are depicted, respectively.

It shall be noted that the hypothetical mass fractions (compare Equation 4.16) of sodium sulfate decahydrate and sodium carbonate decahydrate in solution are represented by blue and red squares in both diagrams.

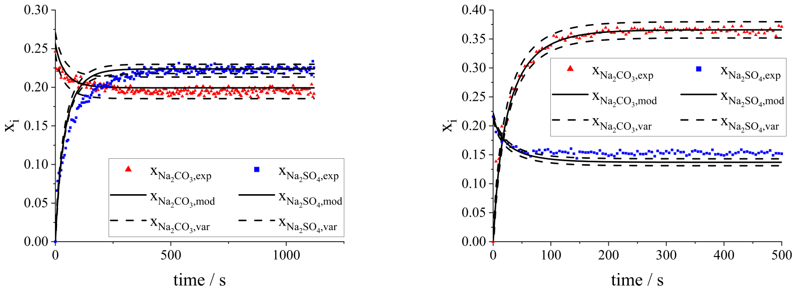

(a) **(b)**

Figure 4.18: Dissolution courses at 17°C of sodium sulfate decahydrate (**a**) and sodium carbonate decahydrate (**b**). Mass fractions are displayed with respect to the respective decahydrate in solution. Solid lines are modeled courses with average kinetic data from multiple experiments. Dashed lines are accuracy ranges which were taken as the experimental measurement uncertainty of both components.

$$x_{i\cdot 10\mathrm{H_2O}} = x_i \cdot \frac{\tilde{M}_{i\cdot 10\mathrm{H_2O}}}{\tilde{M}_i} \tag{4.16}$$

The initial concentrations of the respective foreign materials were chosen rather high at $x_{\mathrm{Na_2SO_4\cdot 10H_2O}} = 0.22$ and $x_{\mathrm{Na_2CO_3\cdot 10H_2O}} = 0.25$. With dissolution of the substrate material, the concentration in solution increased. Thus, the mass fraction of the other component diminished. After 150 seconds, a steady-state was reached which equaled equilibrium composition at this temperature. By applying Equations 4.13 - 4.15 from theoretical considerations, it is possible to model the dissolution process with the power law function (Equation 2.10a). The sum of least square errors was used to adjust the model curve to the experimental data. For that, mass transfer coefficient was varied. The equilibrium concentration was taken from the steady-state value. This led to averaged mass transfer coefficients of $k_{d,\mathrm{Na_2SO_4}} = (6 \pm 2) \cdot 10^{-6}$ m s^{-1} and $k_{d,\mathrm{Na_2CO_3}} = (10 \pm 4) \cdot 10^{-6}$ m s^{-1} in a multi-component set-up. At least nine independent experiments were conducted with different equilibration temperatures. All obtained kinetic parameters were averaged to obtain the mean value. The deviation was limited to the shown values even though different final equilibrium temperatures were applied. The kinetic parameters are listed in Table 4.3 together with the data from crystallization experiments. The diffusional mass transfer coefficients of the ternary systems are of similar magnitude to the corresponding values for binary experiments [Helfenritter and Kind, 2022a].

4.2.4 Ternary crystallization

Crystallization processes were conducted with varied starting supersaturations and different equilibrium temperatures. The temperature range was between 17°C and 23.5°C. The limits were set so that only decahydrates of both components are stable which is not the case at temperatures above 27°C. Furthermore, the initial supersaturation was limited to 3 K. With higher supersaturations, spontaneous nucleation could not be prevented (compare Section 4.1). Because of the narrow temperature range, mass transfer coefficients did not differ significantly. Hence, only a single equilibrium temperature and supersaturation will be discussed here. The other results can be seen in Helfenritter and Kind [2022a].

Having two components in solution, which are able to solidify, two different cases are possible: material separation of a single component and simultaneous growth. Both were observed during the experimental study independent from the substrate choice. Thus, the principal behavior cannot be related solely to the substrate material. First, results from simultaneous growth processes will be shown for both substrate materials. The concentration courses at 17°C with similar initial supersaturation are depicted in Figure 4.19.

The initial solutions were saturated at 20°C and brought in contact with the substrates after a temperature of 17°C was reached. The compositions of $x_{\mathrm{Na_2SO_4\cdot 10H_2O}} = 0.25$ and $x_{\mathrm{Na_2CO_3\cdot 10H_2O}} = 0.37$ correspond to supersaturations of $S_{\mathrm{Na_2SO_4\cdot 10H_2O}} = 1.09$ and $S_{\mathrm{Na_2CO_3\cdot 10H_2O}} = 1.05$ calculated with PhreeqC under usage of the *FREZCHEM* database [Marion et al., 2010; Toner and Sletten, 2013]. Diagram (a) in Figure 4.19 shows the behavior on a sodium sulfate decahydrate substrate. The two components show a similar desupersaturation behavior. In contrast to dissolution mass transfer coefficients, no deviations are given for all crystallization experiments. This is because of varying crystallization orders that occurred in independent experiments. With it, the units and order of magnitudes of the mass transfer coefficient $k_{g,i}$ vary, too. Sodium sulfate crystallized

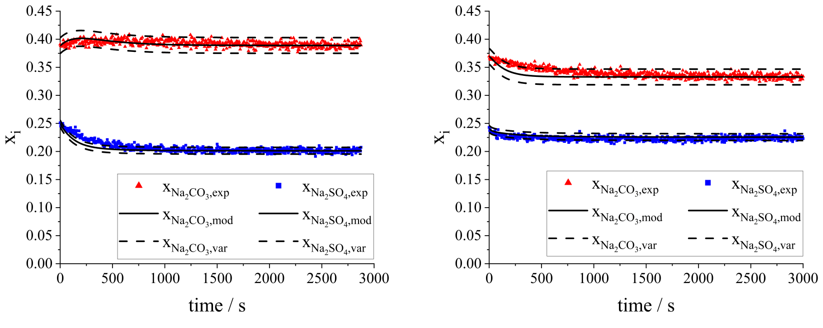

(a) **(b)**

Figure 4.19: Desupersaturation courses at 17°C on sodium sulfate substrate (**a**) and sodium carbonate substrate (**b**). Solutions were saturated at 20°C. Both components transfer from liquid to solid. Mass fractions are displayed with respect to the respective decahydrate in solution. Solid lines are modeled courses with average kinetic data from multiple experiments. Dashed lines are accuracy ranges which were taken as the experimental Raman measurement uncertainty of both components.

with an averaged mass transfer coefficient of $k_{g,\mathrm{Na_2SO_4}} = 2 \cdot 10^{-6}$ m s^{-1} and a crystallization order of $g = 1$. On the other hand, sodium carbonate decahydrate had the same order ($g = 1$) but a slightly higher averaged mass transfer coefficient of $k_{g,\mathrm{Na_2CO_3}} = 6 \cdot 10^{-6}$ m s^{-1}. As a result, both components equilibrated in similar time ranges. The kinetic parameters are listed in Table 4.3 together with the data from dissolution experiments. Comparing the coefficients with the diffusional mass transfer coefficients from before ($k_{d,\mathrm{Na_2SO_4}} = 10 \cdot 10^{-6}$ m s^{-1} and $k_{d,\mathrm{Na_2CO_3}} = 6 \cdot 10^{-6}$ m s^{-1}), it is clear that a combination of diffusion and integration limitation prevailed. $k_{g,i}$ incorporates diffusional and integrational resistances (compare Equation 2.11). If $k_{g,i}$ was smaller than $k_{d,i}$, the mass transfer coefficient at the interface $k_{r,i}$ had to be smaller than $k_{d,i}$ and dictated the process velocity. Since the differences were not very large, the overall kinetics were also limited by the diffusion process. In binary experiments on sodium sulfate decahydrate substrates, solely diffusion limitation was observed [Helfenritter and Kind, 2022a]. Hence, the presence of carbonate ions led to a hindrance at the interface and slowed down the process. On the other hand, sodium carbonate decahydrate crystallization onto sodium sulfate decahydrate appeared to be similar to the crystallization behavior on itself.

The behavior on a sodium carbonate decahydrate substrate in Diagram (b) was slightly different. The substrate component crystallized reached equilibrium after 500 seconds whereas the foreign component did not equilibrate during the process time of 3000 seconds. The substrate material solidified faster with an averaged mass transfer coefficient of $k_{g,\mathrm{Na_2CO_3}} = 3 \cdot 10^{-6}$ m $\mathrm{s^{-1}}$ and an order of $g = 1$. On the other hand, sodium sulfate crystallized with a higher order of $g = 2$ and an averaged mass transfer coefficient of $k_{g,\mathrm{Na_2SO_4}} = 1 \cdot 10^{-7}$ $\mathrm{m^4}$ $\mathrm{mol^{-2}}$ $\mathrm{s^{-1}}$. The kinetic parameters are also listed in Table 4.3. Both components were in parts integration limited. Sodium sulfate was mostly integration limited. The order of 2 indicated this on first sight. Similarly to the other experiment, the substrate component appeared to crystallize with diffusion and integration limitation. The comparison of the ternary mass transfer coefficient with the binary showed an interesting behavior of sodium carbonate. In contrast to sodium sulfate decahydrate, it was mostly unaffected by the foreign sulfate ions and crystallized at similar orders compared with binary experiments. The mass transfer coefficient was in a similar order of magnitude [Helfenritter and Kind, 2022a].

With regard to stratification behavior, both processes can also be interpreted phenomenologically. The first process on a sodium sulfate substrate would result in a mostly homogeneous surface composition because both components crystallized with a similar growth velocity. Also, they reached equilibrium in a similar time range. Hence, the solid build-up is uniform. On the contrary, the simultaneous solidification on sodium carbonate decahydrate led to a stratified layer. Due to the fast crystallization of the substrate material itself, the layers in the vicinity of the substrate were rich in sodium carbonate. But because of the simultaneous slower growth of sodium sulfate, these layers were not pure. After 500 seconds, no solidification of sodium carbonated was detected which is why the upper layers have to be made of pure sodium sulfate. This can be interpreted as a self-coating step.

Material separation was observed in just a few cases regardless of the substrate material. All cases had in common that initial supersaturation was low. Two examples at 23.5°C are displayed in Figure 4.20.

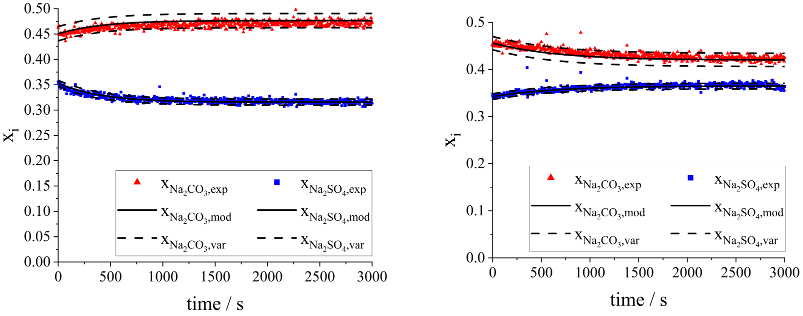

(a) **(b)**

Figure 4.20: Desupersaturation courses at 23.5°C on sodium sulfate substrate (**a**) and sodium carbonate substrate (**b**). Solutions were saturated at 25°C. Just the substrate material transferred to the solid phase. The foreign component remained in solution. Mass fractions are displayed with respect to the respective decahydrate in solution. Solid lines are modeled courses with average kinetic data from multiple experiments. Dashed lines are accuracy ranges which were taken the experimental measurement uncertainty of both components.

Both cases had in common that initial concentrations and supersaturations were equal. The compositions of $x_{\mathrm{Na_2SO_4\cdot 10H_2O}} = 0.34$ and $x_{\mathrm{Na_2CO_3\cdot 10H_2O}} = 0.46$ correspond to supersaturations of $S_{\mathrm{Na_2SO_4\cdot 10H_2O}} = 1.03$ and $S_{\mathrm{Na_2CO_3\cdot 10H_2O}} = 1.02$ calculated with PhreeqC under usage of the *FREZCHEM* database [Marion et al., 2010; Toner and Sletten, 2013]. From Diagram (a), it can be easily seen that only the sodium sulfate concentration decreased while sodium carbonate enriched in the solution. The time to equilibration was about 1500 seconds. The time taken to reach steady-state already provided information on whether the process was diffusion- or integration-limited. Since equilibration of dissolution measurements took about 100 seconds, the present process had to be integration limited. Also, the kinetic evaluation led to the same conclusion. The averaged mass transfer coefficient was determined to $k_{g,\mathrm{Na_2SO_4}} = 6 \cdot 10^{-7}$ m s^{-1} while the order of crystallization was $g = 1$. Hence, the mass transfer coefficient was just a tenth of the diffusion mass transfer coefficient. A similar interpretation and evaluation could be made for the reverse case. Sodium carbonate decahydrate crystallized onto a substrate made from itself with an order of $g = 1$ and an averaged kinetic factor of $k_{g,\mathrm{Na_2CO_3}} = 8 \cdot 10^{-7}$ m s^{-1}. The kinetic parameters are also listed in Table 4.3. The time to a steady-state was about 1000 seconds. Hence, it can be concluded that sulfate ions also impact the growth process of sodium carbonate in case they stay in solution. Due to the enrichment of foreign component, the growing material was hindered. In multi-component diffusion simulations, it was shown that the highest enrichment of foreign component occurred at the growth surface which also explains this behavior. It comes to lower concentration gradients of growing material in the vicinity which slows down the growth process.

The phenomenological viewpoint is rather easy to picture. Because of the sole phase transition of the substrates component, a mostly pure layer was generated. The foreign component enriched in solution. If supersaturation would be increased further, it would result in solidification of this component. This would lead to a mostly pure layer of the foreign component onto a pure substrate material. Hence, this process would be a self-coating step in a single process. In Table 4.3, all evaluated averaged kinetic parameters are listed. The values were averaged from several experiments. The results from dissolution experiments are presented with deviations because the reaction order was always $g = 1$. Because of changing crystallization orders, it was not possible to give deviations for kinetic parameters of the crystallization process. Two cases of crystallization processes are distinguished. First, a sole crystallization of one component in presence of another (separation) and co-crystallization (simultaneous).

4.2.5 Conclusion

A method was found to meet all the above stated criteria. (a) Nucleation processes are suppressed, (b) the growth location is well defined, and (c) the growth of each component is distinguishable. Confocal micro Raman spectroscopy showed its ability to analyze the concentration changes of elelctrolytes in thin films and in a sufficient spatial and time scales. The assumption to measure at just a single point

Table 4.3: List of all determined kinetic parameters from dissolution and desupersaturation measurements.

type of crystallization	parameter	$Na_2SO_4 \cdot 10H_2O$	$Na_2CO_3 \cdot 10H_2O$
dissolution	$k_{d,i}$ / m s^{-1}	$(6 \pm 2) \cdot 10^{-6}$	$(10 \pm 4) \cdot 10^{-6}$
separation	$k_{g,i}$ / m s^{-1}	$6 \cdot 10^{-7}$	$8 \cdot 10^{-7}$
	g / -	1	1
simultaneous	$k_{g,i,\text{substrate}}$ / m^{3g-2} mol$^{-(g-1)}$ s^{-1}	$2 \cdot 10^{-6}$	$3 \cdot 10^{-6}$
	$g_{\text{substrate}}$ / -	1	1
	$k_{g,i,\text{foreign}}$ / m^{3g-2} mol$^{-(g-1)}$ s^{-1}	$1 \cdot 10^{-7}$	$6 \cdot 10^{-6}$
	g_{foreign} / -	2	1

was verified with multi-component Fick diffusion simulations. Also, heat-mass transfer analogies justified this assumption.

With respect to layer formation, initial evidence was retrieved from the presented measurements. In cases of simultaneous crystallization, material stratification was identified if sodium carbonate decahydrate was used as substrate. Because of faster kinetics of the substrates material, the layers in vicinity of the substrate were rich in its material. With advancing solidification, the fraction of the foreign component increased up to unity. Thus, the final layers would be made of the foreign material only. This phenomenological explanation can be compared with Diagram (c) in Figure 1.2 in Section 1.1. With sodium sulfate decahydrate substrates, a mostly uniform solid layer would be predicted from kinetic data (compare Diagram (b) in Figure 1.2 in Section 1.1). Both mass transfer coefficients were in a similar order of magnitude. Regardless of the substrate, all crystallization steps were diffusion and integration limited.

In cases of material separation, the foreign component remained supersaturated in solution. The enrichment resulted in a drastic slowdown of the crystallization of the crystallizing component. The mass transfer coefficient was just one tenth of the diffusion mass transfer coefficient. The resulting solid layer was of pure substrate material. It was assumed that with further supersaturation the solidification of foreign component could be provoked. This would lead to a pure layer of foreign component on the substrate material and hence, to a self-coating (compare Diagram (a) in Figure 1.2 in Section 1.1).

With this section, Hypothesis III - It is possible to determine multi-component growth rates from solution - can be supported. The obtained kinetic results can be used for modeling of layer formation, which will be shown in Chapter 5. Also, other processes such as fouling crystallization in tubes or at surfaces, build-up of geological salt formations or alloy formation could benefit from the developed method and their results.

4.3 Post-process assessment of the solid

The theoretical explanations of possible solid compositions in the conclusion of the previous chapter lead to the question whether these phenomena can also be observed in resulting solid layers. For this purpose, an experimental set-up is designed, which is also intended to answer Hypothesis III of this thesis - The rate of supersaturation build-up has an impact on the final layer assemblage. Additionally, the influence of initial conditions will be addressed in this chapter (compare Figure 1.3 in Section 1.2). The experiments and different set-ups were conducted and developed together with Stefan Höll, Karam Swaid, Kai Bauer and Thomas Kieble in their bachelor theses. The general set-up is similar to the one in Section 4.2. A liquid film containing Na_2SO_4 and Na_2CO_3 is brought in contact with a substrate. Other than before, the film thickness is not limited to 150 µm. Since a larger amount of phase-transferring material is required to evaluate the solid, a starting mass of at least 2 g of solution is used. In crystal growth experiments in the previous section, at most 3 mg were transferred from liquid to solid. The impact of supersaturation rates and of substrate materials on the stratification will be characterized here. Supersaturation is the driving force for crystal growth and nucleation and hence, an obviously important parameter. From nucleation experiments, it is well known that cooling or evaporation rates influence the metastable zone [Mullin, 2001]. The substrate material is another apparent influence parameter since the kinetics and the behavior of different materials could differ immensely. This is shown in Section 4.2. Here, the resulting layers are analyzed and the actual impact on solid formation is demonstrated.

4.3.1 Methodology

There are different ways to supersaturate a solution. Considering Equation 2.1, a raising of a component's mass fraction with respect to its equilibrium state would supersaturate it. Thus, a reduction of other components, e.g. the solvent through drying, increases saturation. To achieve comparable drying conditions, a channel is designed and experiments are conducted. Another way to supersaturate a solution is a change in temperature. This is only possible if the solubility is temperature dependent. As can be seen from Figure 4.1 in Section 4.1, this is the case for the material system Na_2SO_4, Na_2CO_3, and H_2O. For this, an experiment is designed which permits to vary cooling rates of a liquid film in contact with a crystalline substrate.

Sample preparation

The samples in cooling and drying experiments are produced the same way. The procedure is similar to the preparation of substrates in Section 4.2.2. A quadratic aluminum sample carrier is filled with a powder of one of the respective salts. The tabletting procedure resembles the one already explained for crystal growth substrate preparation. The only difference is the form of the substrate carrier and the applied pressure. The applied pressure is 3.2 MN m^{-2}. In addition to compacting powder, the material testing machine is able to determine positions with a measurement uncertainty of 1.5 µm. With this, it is possible to evaluate the thickness of the substrate and its position inside the carrier (compare Figure 4.21). This is important for the analysis of the new surface with respect to its height.

In order to determine the position of the substrate, it is necessary to identify the dimension of each carrier. Prior to substrate production, lengths z_1 and z_2 are ruled out. After the compaction, length z_3 can be read out. The prepared substrates are covered with laboratory foil and stored at 8°C so that the material does not change. Prior to the experiments, saturated solution is added again to wet the surface. It is carefully removed with a paper towel and dried with air. Afterwards, about 2 g of a eutectic ternary solution are added. The exact weight is recorded with a laboratory scale.

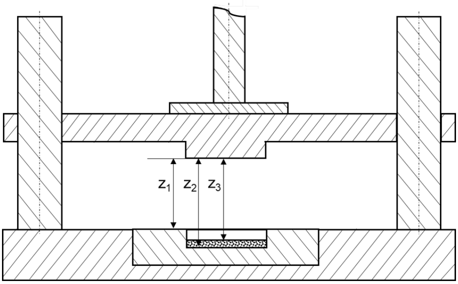

Figure 4.21: Drawing of tabletting device. The stamp is moved downwards. The guidance ensures that it fits into the cavity. The loose powder is compacted. Prior to the substrate production lengths z_1 and z_2 of all carriers have to be determined. Length z_3 is identified after a substrate is produced.

Generation of supersaturation

In order to cool a solution in contact with a substrate, two aluminum plates are designed to incorporate the sample carrier. Tempered water flows through cavities to temper the device. The installation is displayed in Figure 4.22.

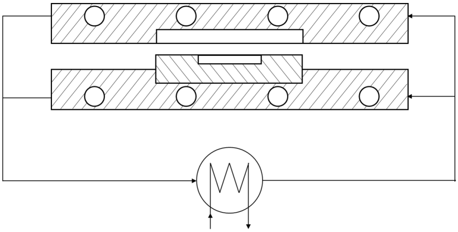

Figure 4.22: Schematic drawing of the cooling station. It consists of two aluminum plates which can be tempered by water flowing through. The temperature is set with an adjustable thermostat. Substrate carriers are inserted into a cavity in the middle.

The total set-up is insulated with a 3 cm layer of insulation material (AF/Armaflex®, $\lambda = 0.033$ W m^{-1} K^{-1}). The initial temperature (25°C) of the device is set to the equilibrium temperature of the applied solution ($x_{\text{Na}_2\text{SO}_4} = 0.162$ and $x_{\text{Na}_2\text{CO}_3} = 0.179$) for at least 30 minutes. A programmable thermostat (LAUDA ECO E10) decreases the temperature gradually. Two different cooling rates -

0.01 K min^{-1} and 0.1 K min^{-1} - are used. The offset between thermostat and liquid temperature lies below one minute which is why it is neglected. After reaching 16°C, the experiments are aborted or temperature is held constant for an additional hour to allow an entire equilibration. After finishing the experiment, potential supernatant solution is removed with a syringe and stored for quantitative analysis. Afterwards and in cases no solution can be retained, lint-free wipes are put onto the solid surface. The carrier is flipped upside down to remove remaining pore solution. This is a crucial step in two ways. First, remaining solution would hinder the layer analysis. Furthermore, solvent is able to evaporate which causes additional crystallization. This would result in falsified layer compositions.

Also, an experimental set-up is used to evaporate the applied solution. A specifically designed drying channel is shown in Figure 4.23.

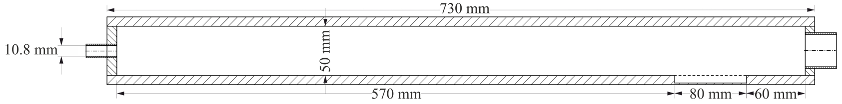

Figure 4.23: Technical drawing of the drying channel. All walls except the top cover are made of aluminum and have a thickness of 10 mm. The cover is made of Plexiglass®. The inlet for the tempered air is located on the left side. The slot for the substrate carrier is located 570 mm from the inlet to ensure fully developed airflow.

The considerations for the underlying design are explained in Appendix A.1. Also, deeper theoretical background on drying is given there. The channel allows to adjust the evaporation rate and steady-state temperature. Air and wall temperature, humidity, and volume flux can be varied. According to Equation A.1 these are the principal influencing parameters on drying rate. The width of the channel is 60 cm. The channel is insulated with a 2 cm layer of AF/Armaflex® ($\lambda = 0.033$ W m^{-1} K^{-1}). The flow of dry compressed air is divided and adjusted with two volume flow meters (Q-Flow 140, Vögtlin [$\Delta\dot{V} = \pm5\%$]). One is connected with a tempered bubble column and the other with a thermostat. Thereby, drying conditions are regulated. Temperature (Pt-100 [$\Delta T = \pm 0.01$ K]) and humidity (thermo-hygrometer BC21, Trotec [$\Delta\varphi = \pm 2\%$]) are measured above the sample regularly. It should be constant throughout the drying process. To guarantee constant conditions, all parameters are regulated to the desired settings and run for at least an hour. Then, the sample carrier with a saturated solution is inserted and the process starts immediately. The experiment ends as soon as no liquid can be recognized on the solid. The sample carrier is removed and weighed to obtain the mass of the generated layer.

After both experimental procedures, the carriers are covered with laboratory foil and stored in a fridge at 8°C until the layers are analyzed according to Section 4.3.1.

Layer analysis

The resulting solid surfaces are analyzed layer by layer. An NC milling machine is used for that purpose. A representative section from the middle of the sample carrier is removed with a layer depth of 50 µm. The principle is shown in Figure 4.24.

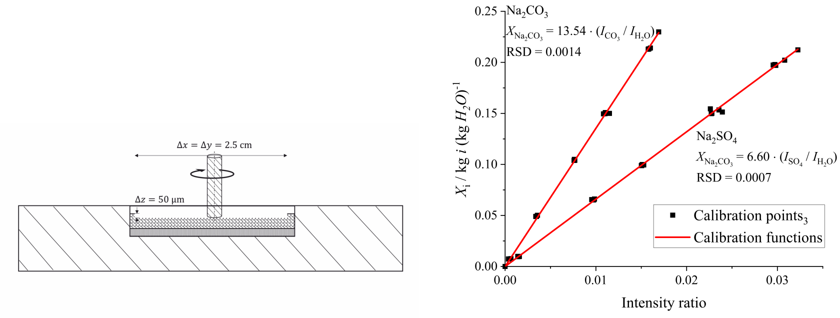

(a) **(b)**

Figure 4.24: In (**a**), a drawing of solid removal is shown. If not other specified, layers are cut off in 50 µm steps. The area of withdrawal is 25x25 mm. Solid is removed until the substrate is reached. Some layers of the substrate are removed, too. Thus, penetration from solution can be examined.

A metal cutter (WF 4/3, Kunzmann) with a stainless steel milling head (∅ = 4 cm) is used to remove the salt from the top of the surface. A rotating speed of 2500 min^{-1} and an axial feed of 200 mm min^{-1} are applied. The powdered salt is collected, weighed and stored in a glass container. Afterwards, the glass containers are put into a drying chamber at temperatures above 60°C to remove hydrate and residual water. Then, the salt is dissolved in a known amount of water. The solution is analyzed with Raman spectroscopy at 25°C. A tempered cell (compare Figure 4.24 (a)) is used at isothermal conditions.

A similar setting is used compared to Section 4.2.2. The experimental cell is substituted and the objective is replaced by an air objective with an optical enlargement of ten. Hence, the focus point is much larger compared to the already explained setting and appropriate for analyzing a solution. Since the setting is different from the former, another calibration function is used here (Figure 4.24 (b)). From Raman results, the composition of the solution is calculated. With the relation of measured mass loads and known masses of removed salt and added water, it is possible to calculate the actual layer composition in each solid layer.

4.3.2 Results

The influence of initial conditions will be discussed in terms of a variation of substrate materials. A change of solution composition would also result in changing layer assemblages but will not be examined in this work. It could be a possible topic for future works. The resulting layer composition of different supersaturation rates can be interpreted in various ways. On the one hand, they can be compared with case studies from section 3.3. With this, conclusions of kinetic parameters or occuring metastable states can be drawn. Also, it is possible to interpret solution compositions over the process time from final layer compositions. Thus, the history of solidification and fluid composition can be concluded from material formation.

Impact of substrate

To observe the influence of substrate materials, only cooling experiments will be examined. In Figure 4.25, two resulting solid material assemblages are displayed.

Both diagrams show the layer-wise composition of the resulting solid from cooling experiments with a cooling rate of 0.01 K min^{-1} and an initial solution composition of $x_{\mathrm{Na_2SO_4}} = 0.162$ and $x_{\mathrm{Na_2CO_3}} = 0.179$. Every layer was removed in 50 µm steps. The solid layer composition is expressed as material fraction

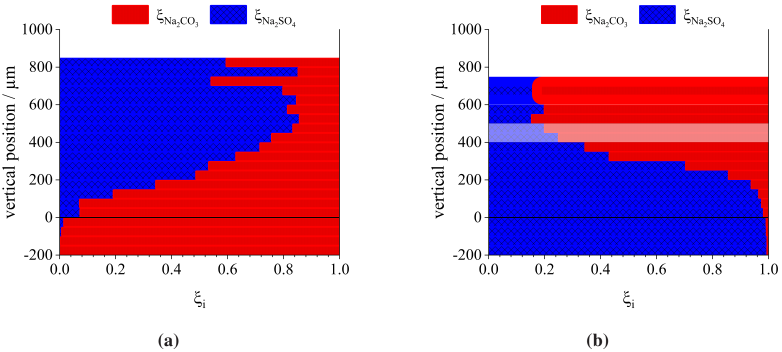

Figure 4.25: Diagrams of solid layer composition as a function of vertical position in the assemblage. In Diagram (**a**), the average of three experiments with a cooling rate of 0.01 K min^{-1} on a sodium carbonate substrate is shown. In Diagram (**b**), the reverse experiment on a sodium sulfate substrate is presented.

of electrolytes $\xi_i = \frac{x_i}{\sum x_j}$, $j \neq$ solvent (compare Equation 3.1). Water was not considered since both solids should be present as decahydrates. The mass fraction of sodium sulfate is depicted in blue colored bars and can be read from the left. Sodium carbonate is shown as red colored bars and its fraction has to be read from the right. In addition to the composition, it is possible to read the final height of the solid. Also, it is possible to see incorporations of foreign components into the substrate. If the composition below the vertical position of zero is not uniformly colored, there are incorporations. In case of a blurred color, analysis was not possible which is why estimated values are used. The process conditions of both experiments were equal. A cooling rate of 0.01 K min^{-1} was applied. 16°C were chosen as end temperature. As this temperature was reached, an isothermal part was added for an hour. Both diagrams contain averaged results from multiple experiments. At minimum three repetitions were used to obtain these diagrams. Nevertheless, at some higher vertical positions, only the results from one experiment are shown. Especially with sodium sulfate as the substrate, not every experiment resulted in similar heights as are displayed. This has to be ascribed to nucleation behavior of the foreign component which was not always equal. Hence, growth processes of foreign components were initialized at different times which led to variations in final layer heights.

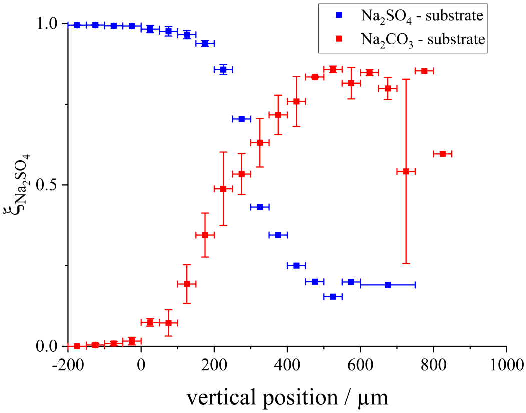

Figure 4.26: Diagram of stratification behavior. The horizontal error markers indicate the variation of the three conducted experiments. In case of sodium sulfate substrate it is replaced by the error from analysis, since layers above 200 µm were only observed in one experiment. Vertical error markers show the width of one layer. It represents the adjustment of the NC-cutter.

Both solid assemblages have in common that the substrate was not penetrated by the solution. The foreign component appears in very small concentrations and can be neglected. The final heights were similar and lay in the range of 800 µm. Both experiments show a strong stratification of components. Especially on sodium sulfate, the areas close to the substrate contained nearly 100% of its own material. From 200 µm vertical position, greater fractions of sodium carbonate can be recognized. Upon reaching 400 µm, nearly 80% of the layer were made of the foreign component. From this point, the value is constant up to the top. The distribution of material is a little different on sodium carbonate. The content of foreign material increased steadily beginning close to the substrate. A final fraction of nearly 85% was reached at a position of 500 µm. Afterwards, the composition was constant with two outliers. The stratification behavior of both experiments can be observed in Figure 4.26 more easily.

Here, the mass fraction of sodium sulfate $\xi_{Na_2SO_4}$ is plotted over the vertical position. This time, blue color represents the behavior on a sodium sulfate substrate. At first, sulfate fractions remained at one or close to one. Afterwards, the fraction decreased sharply and reached its final composition of about 20%. In contrast, red colored points representing a sodium carbonate substrate started to increase directly above the substrate. The change in composition was steady and reached a steady state at a similar position compared to the other. Hence, the stratification behavior was a little different if substrates were changed. Sodium sulfate substrate had fewer foreign contents in the vicinity of the substrate. The processes can also be interpreted with respect to the solution composition which prevailed at the time a layer was built. In Figure 4.27, the present solutions at each genesis of a layer are depicted exemplarily for one experiment of each substrate.

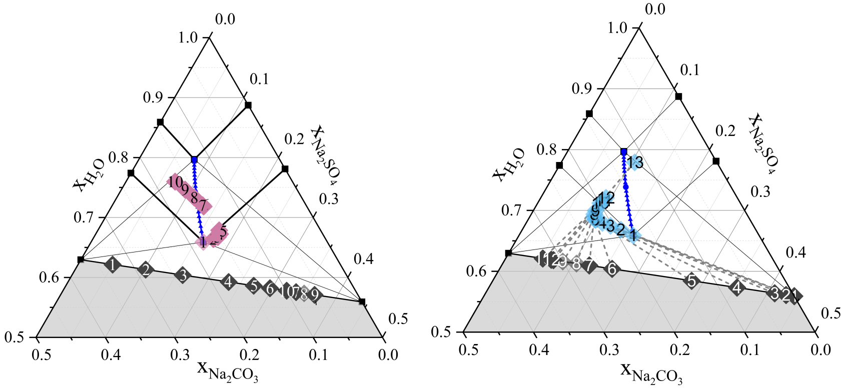

(a) **(b)**

Figure 4.27: Triangular diagrams of cooling processes with a rate of 0.01 K min^{-1} on sodium carbonate substrate (**a**) and sodium sulfate substrate (**b**). Gray diamonds represent solid compositions from each layer (1 being in the vicinity of the substrate). In lighter gray (e.g. point 8 in (**a**)), points are marked which had to be estimated because analytics could not be conducted. With light red and light blue diamonds solution compositions are shown. Gray dashed lines connect solid compositions with the prevailing solution composition at the time the solid developed.

Solid compositions are marked with gray diamonds and translated into decahydrate states. Three points of the examples could not be analyzed. Hence, estimated compositions are inserted as lighter gray diamonds (e.g., point 8 in Diagram (a) and points 8 and 9 in Diagram (b)). Liquid composition is depicted with light red and blue diamonds. Red corresponds again with carbonate and blue with sulfate substrates. With blue triangles, the course of eutectic composition with decreasing temperature is depicted. It starts at 25°C and ends at 16°C. Also, binary solubility data and linearized solubility lines are shown. The back calculation of solution composition was done with mass balances. From analytics, masses of each electrolyte in each layer were known. With the change in mass, new solution composition was possible to calculate. A remarkable difference of both solution evolutions can be recognized in early stages. While the sulfate concentration of solid layers crystallizing on a sodium carbonate substrate increased steadily, the solution composition stayed relatively close to the eutectic line. With solid layer number 5, solution turned in direction of the eutectic line. This is because of higher supersaturation of sodium sulfate in this part. Afterwards, the eutectic line was crossed and the last compositions were supersaturated with respect to the substrate material. The final fluid composition did not reach the upper blue triangle, which corresponds with equilibrium at final temperature. On the contrary, the behavior on a sodium sulfate substrate was different. The solution started to supersaturate immensely with respect to sodium carbonate while desuperaturating in case of sodium sulfate. Point 8 marks a turning point and solution regulated in direction of the eutectic line. Up to the third point, it can be argumented that sodium carbonate was in a metastable state and not able to crystallize. Afterwards, crystallization started and its phase transition increased further. The final fluid composition is close to the equilibrium state at 16°C.

Impact of supersaturation rate

Supersaturation can be built up in two ways. Both will be discussed in this section with two exemplary cases. First, the difference in cooling rate and its impact on the final layer distribution will be covered. Afterwards, exemplary cases of drying experiments will be shown. Supersaturation is built-up through solvent removal. In Figure 4.28, two solid deposits are shown which resulted from two different cooling rates.

Both experiments were conducted with a eutectic solution saturated at 25°C deposited on a sodium carbonate substrate. The final temperature was chosen to be 16°C. The cooling rates were 0.01 K min^{-1}, which was already shown in

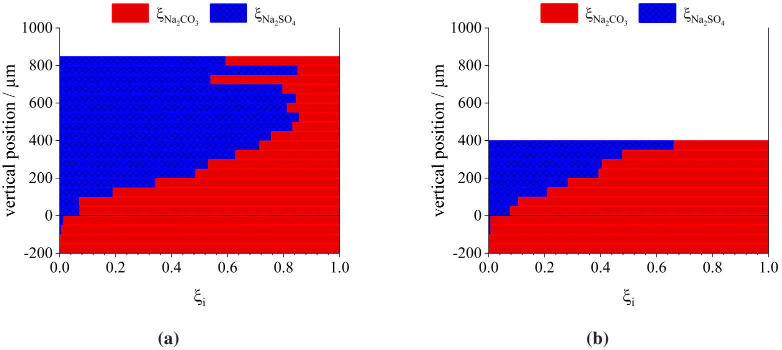

(a)

(b)

Figure 4.28: Diagrams of solid layer composition as a function of vertical position in the assemblage. In Diagram (**a**), the average of three experiments with a cooling rate of 0.01 K min^{-1} on a sodium carbonate substrate is shown. In Diagram (**b**), the same substrate was used but with a cooling rate of 0.1 K min^{-1}.

Figure 4.25, and 0.1 K min^{-1}, respectively. The final temperature was held for an additional time of 60 minutes in both experiments. All parameter sets were repeated three times and their results were averaged. The composition variation over the vertical position of the solid show obvious differences but also similarities between different supersaturation rates. On the one hand, the final solid height was about 800 µm at 0.01 K min^{-1} (shown in Diagram (a)) whereas the half of it was reached with the faster rate of 0.1 K min^{-1} (Diagram (b)). On the other hand, both substrates did not show any integration of foreign component. Also, the increments of sodium sulfate content over the height were similar. It would have been expected that a higher cooling rate would result in a more uniform layer composition even in the vicinity of the substrate. The similar stratification behavior can be seen in Figure 4.29.

The fraction of sodium sulfate increased with a similar slope and directly from the substrate surface (vertical position of 0 µm). The marks of the experiment with 0.1 K min^{-1} are displayed in light red triangles and end at 400 µm. The smaller layer height can be explained with experimental time. It summed up to 150 minutes at higher cooling rate with an additional hour at isothermal conditions. The other process took 960 minutes. Due to the longer time, a higher amount

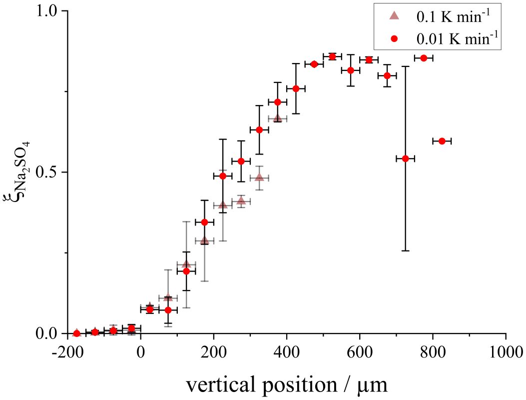

Figure 4.29: Diagram of stratification behavior. The stratification behavior does not significantly differ with changing the cooling rate. Due to the shorter process time the red triangles end at 400 µm with a cooling rate of 0.1 K min^{-1}.

could crystallize because of longer exposition to a supersaturated solution. Both processes are displayed additionally in triangular diagrams in Figure 4.30.

With gray diamonds, solid compositions of each layer are displayed in both diagrams. In Diagram (a), solution compositions of experiments with the lower cooling rate are shown with light red diamonds. In Diagram (b), these are plotted for the higher cooling rate as red diamonds. Again, masses of each electrolyte in each layer were known from layer removal and analytics. With the change in mass, new solution composition was possible to calculate. Both differ immensely. At high cooling rates, sodium carbonate mostly crystallized on its own substrate. Hence, the solution supersaturated strongly with respect to sodium sulfate. Even though the sodium sulfate fraction increased up to 50% in the upper layer, the trend did not invert. This is due to the powder masses obtained in the upper layer, which were rather low compared to the other layers due to the higher porosity. Therefore, the powder mass removed was lower and did not have a great influence on the mass balance of the solution. At the end of the process, the solution was far away from equilibrium, which is represented by the upper blue triangle. Thus, it would be expected that mostly sodium sulfate would crystallize if the process

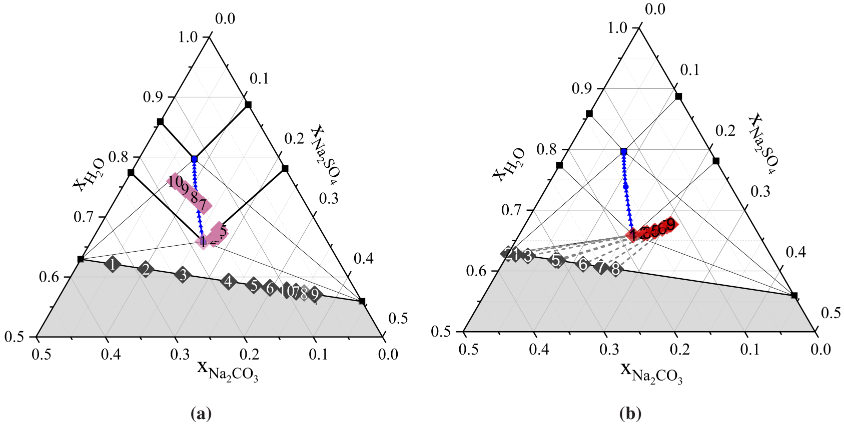

Figure 4.30: Triangular diagrams of cooling processes on sodium carbonate substrate with a rate of 0.01 K min^{-1} (**a**) and 0.1 K min^{-1} (**b**). Start of the process is at 25°C and end temperature is chosen to be 16°C. With blue triangles the temperature dependent eutectic compositions are displayed in this range. Gray diamonds represent solid compositions from each layer (1 being in the vicinity of the substrate). With light red and red diamonds solution compositions are shown. Gray dashed lines connect solid compositions with the prevailing solution composition at the time the solid developed.

ran longer. In case of the lower rate, the solution composition first supersaturated more with respect to sodium sulfate. But it turned towards the eutectic line and crossed it after a few layers. Generally, the course of the solutions can be interpreted in terms of stabilities. Sodium carbonate crystallized immediately due to the presence of its own substrate. Sodium sulfate remained supersaturated in solution. It became even more supersaturated up the turning point in case of the low rate, i.e. points 3 and 4, respectively. This can interpreted as metastable limits of heterogeneous nucleation on a sodium carbonate substrate. Afterwards, it was able to grow due to the higher supersaturation and exceeded the other component. Similarly, the higher cooling rate brought up a different metastable limit which lay at higher supersaturation.

In cases where supersaturation is produced by drying the solution, two phase transfer currents occur simultaneously. In addition to the crystallization front at the solid surface, evaporation of the pure solvent takes place at the gas-liquid interface. Therefore, it is possible that diffusion processes within the liquid film lead to a different solidification behavior than the cooling crystallization. Furthermore, the processes differ in their thermodynamic phase behavior. While drying takes place at a constant temperature and thus with an unchanged ternary solubility behavior, cooling crystallization leads to a change in solubility. In order to investigate the comparability to cooling crystallization and the influence of supersaturation rate on solid assemblages, drying rates were varied at constant temperatures of 20°C. It was assumed that fluid and air temperature were the same. To guarantee this assumption, the channel jacket was tempered to the same temperature as the drying air. In Figure 4.31, two examples of resulting layers from drying experiments are displayed.

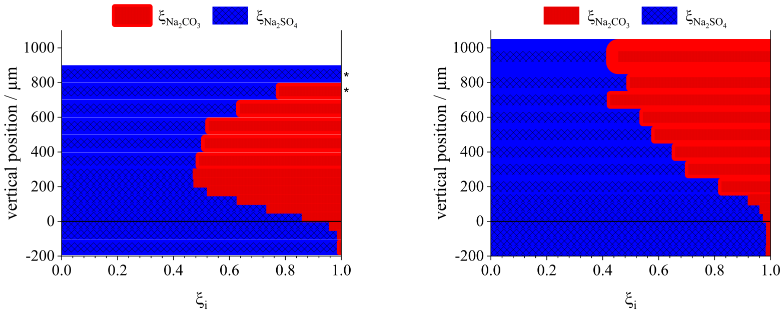

(a) **(b)**

Figure 4.31: Diagrams of solid layer composition as a function of vertical position in the assemblage. In Diagram (**a**), the average of three experiments with a drying rate of $\dot{m}_{dry} = 0.015$ g m^{-2} s^{-1} on a sodium carbonate substrate is shown. In Diagram (**b**), the same substrate was used but with a drying rate of $\dot{m}_{dry} = 0.109$ g m^{-2} s^{-1}. Both experiments were conducted isothermally at 20°C. The two marked upper layers of Diagram (**a**) were only observed in one experiment.

Diagram (a) is the result of an experiment with no drying air flux. The solution was dried at static air and a relative humidity of 67%. The theoretical specific drying rate was $\dot{m}_{dry} = 0.015$ g m^{-2} s^{-1}. It was calculated with Equations A.1-A.8 in Appendix A.1 and the assumption that water phase transfer was not impacted by other materials. In contrast, the solid layer assemblage in Diagram (b) resulted from a specific drying rate of $\dot{m}_{dry} = 0.109$ g m^{-2} s^{-1}. To achieve the ten times higher value, a mean air velocity of 0.2 m s^{-1} with a relative humidity of 10% was applied. Higher drying rates were also tried to adjust. However, at these conditions a cover layer was built on top of the solutions which prevented it from drying. Hence, the experiments were limited to relatively low supersaturation rates. Both diagrams were built with averaged values from three repetitions. In comparison with solid layers from cooling experiments, total heights reached 1000 µm or even more. In contrast to cooling experiments, the total amount of dissolved material solidified. Most of the cooling experiments had remaining solution on top of the layer which is why the resulting layer heights were lower. At first sight, the stratification behavior of both experiments were different. The foreign component content increased rapidly at lower drying rates up to a mass fraction of 0.5 at 200 µm. It remained at this concentration up to the height of 600 µm and decreased afterwards to zero at the top of the solid. The last observation was made in only one of the three experiments. Thus, it is just one possible result. Higher drying rates led to a slower increment in foreign content. It reached 0.5 after 500 µm. Afterwards, it increased a little further to 0.6 and remained at this value up to the top. At both drying rates, the penetration of the substrate can be neglected. The stratification comparison in Figure 4.32 highlights the stated phenomena.

The diagram shows demonstratively that the higher drying rate led to a slower and later decrease of substrate material in the solid layer. Due to the later growth of foreign material, the top layer was mostly made of it. In contrast, the lower rate caused an early crystallization of the foreign material and thus, later on no sodium carbonate was available for growth in the top layer. This is why the top layer consisted totally of substrate material. Again, it has to be stated that this behavior was only observed in one of three experiments. In fact, this behavior is not intuitive. A slower supersaturation build-up would be expected to produce a more stratified solid. Due to the slower build-up, the substrate material would have more time to solely grow onto the surface while the foreign component remains in solution in a metastable state. Keeping the upper two layers out of the interpretation, it could be argued that the first layers in the vicinity of the substrate were not dense. With further supersaturation, the solution in the pores crystallized. That produced a higher content of foreign components in lower

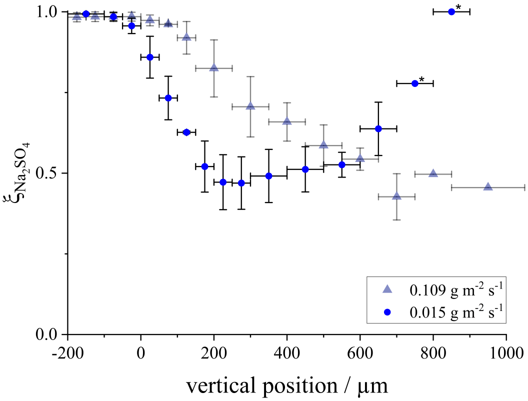

Figure 4.32: Diagram of stratification behavior. The stratification behavior differs with changing the drying rate. Due to the higher amounts of foreign component in lower positions with the lower drying rate the amounts are logically higher in higher position. The marked points with stars were only observed in one experiment.

vertical positions. Thus, the final layer assemblage cannot be interpreted as a timely growth sequence as was assumed. The two upper layers of the third experiment would not fit in this explanation. These are only reasonable if the process is considered as a time sequence of the growth process as explained earlier. Different growth behaviors can be reasoned with different nucleation behaviors. In one of the three experiments, nuclei of the foreign component were built early. The growth caught up with substrate component which was the remaining component at the end of the drying process. In Appendix A.9, additional results from drying experiments are shown. On the one hand, these depict the layering behavior on sodium carbonate decahydrate substrates. On the other hand, results of experiments at 25°C with both substrate materials are illustrated.

4.3.3 Conclusion

It was possible to investigate the solid layer composition in dependence of process parameters and conclude solution behavior. The aim of the experiments was to show the influence of substrate selection and supersaturation build-up. Sodium carbonate and sulfate decahydrate were used as substrates. Eutectic saturated solutions at 20 and 25°C were used. On sodium carbonate substrates, the foreign component sodium sulfate was able to grow immediately onto the substrate. This led to a steady increment of foreign content in the resulting solid. In the reverse experiments with sodium sulfate substrates, the layers in the vicinity of the substrate were mostly of sodium sulfate. At higher vertical positions, which correspond with higher process times, the content of foreign material increased drastically. The final layers were mostly made of foreign material.

In cooling experiments, both final solid assemblages showed material stratification. However, the increment of foreign content on sodium sulfate substrate was steeper and not as steady as reversely on sodium carbonate. It was concluded that the metastable zone of heterogeneous nucleation of sodium sulfate in presence of sodium carbonate is smaller than of sodium carbonate in presence of sodium sulfate.

Other than hypothesized in Hypothesis IV, the supersaturation rate had no great influence in the investigated cooling and drying ranges. Cooling experiments showed mostly no difference in layer compositions. The final heights differed, which can be related to longer process times of lower cooling rates. The saturated solution was exposed longer to the growing solid, which was able to grow more as a result. In drying experiments, only low supersaturation rates could be analyzed. Higher rates resulted in cover layers on the solution, which were not able to dry further. In contrast to the expectations, the stratification was observed to being stronger with lower drying rates. It is assumed that a lower supersaturation rate led to a more porous layer in the vicinity of the substrate. Hence, solution remained in the pores and crystallized at a later time. This led to a higher content of foreign material in the substrate vicinity. Thus, the solid layer could not be taken as a timeline of the growth process.

5 Comparison of experiments with theory

In Section 5.1, the results from each section in Chapter 4 are discussed with respect to their interrelationships. Each section produced interpretations of the results that were not explicitly intended by the actual experimental design. For example, phenomenological interpretations regarding solid state composition have been made from kinetic studies of crystal growth. These will be summarized and connected to each other.

In Section 5.2, the experimentally determined kinetics from Section 4.2 are used to calculate the theoretical solid assemblage of selected experiments from Section 4.3 with the model from Chapter 3. It is intended to demonstrate the applicability and optimization potential of the model to realistic processes.

5.1 Interrelationships of experiments

First of all, the results of all three experimental parts will be compared preliminarily on their similarities in provoking stratified layers and metastable zones. The conclusions from this examination will be aligned with theoretical knowledge. Figure 5.1 gives a brief overview of the relationships and dependencies of the four influencing factors: Phase equilibrium, kinetics, supersaturation rate, and initial conditions.

As far as material stratification is concerned, the three experimental studies in Sections 4.1 - 4.3 have shown that each one plays a role in affecting the solid assemblage. Beginning with crystal growth kinetics, it is obvious that a strong connection to phase equilibria exists. Different solid entities have different crystal growth kinetics. Hence, every solid entity has to be evaluated with respect to its

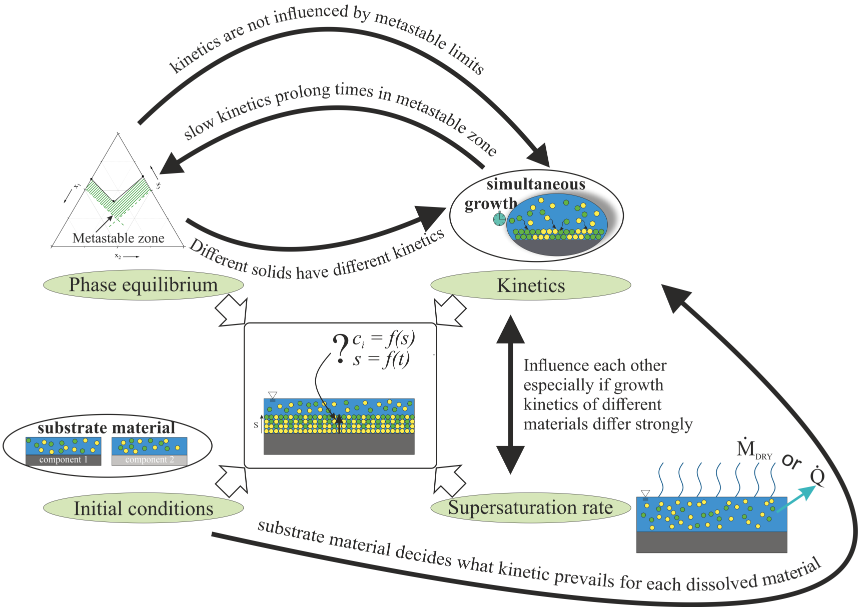

Figure 5.1: Overview and connection of the influencing factors: phase equilibrium, supersaturation rate, kinetics, and initial conditions.

own crystal growth kinetic. Considering metastable limits, growth kinetics are not influenced since these are not related. Nevertheless, if growth kinetics are slow and not able to decrease supersaturation, metastable zone limits could be crossed which would lead to unintended nucleation. This in turn creates new growth spots which could be located unfavorably. If new layers should be built on a substrate by evaporating a solution, nucleation and growth at the gas-liquid interface would create a cover layer. This would prevent drying of residual solution and the final product would have fluid inclusions. Thus, the metastability limits do not affect crystal growth kinetics with respect to layer formation, but vice versa, especially in conjunction with supersaturation rates.

On the contrary, supersaturation rate influences solid composition together with growth kinetics. But solely if kinetics of involved component's are very different. In that case, a fast supersaturation rate would lead to a uniform layer even though one components kinetic is faster. High supersaturations would diminish that effect. At slow supersaturation rates, the fast growing component would dominate early solid layers. Hence, concurrent crystal growth kinetics along with supersaturation rate influence the solid assemblage.

The influence of the supersaturation rate together with the phase equilibria and the limits of the metastable zone on the stratification has already been anticipated in the consideration of crystal growth kinetics. A rapid build-up of supersaturation would quickly lead through metastable zones. This in turn leads to instable states and unintended spontaneous nucleation.

Analyzing results from cooling stratification experiments with respect to metastable states, insights into heterogeneous nucleation can be drawn. Taking Figure 4.27, solution compositions during solidification process were estimated. From these, it is possible to derive metastable limits for heterogeneous nucleation of the counter-electrolyte. Both diagrams are displayed again in Figure 5.2 but with an addition of a metastable zone limit.

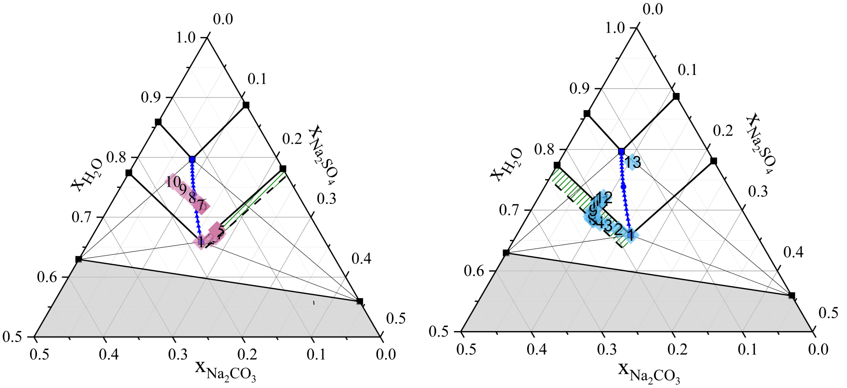

(a) **(b)**

Figure 5.2: Triangular diagrams of cooling processes with a rate of 0.01 K min^{-1} on sodium carbonate substrate (**a**) and sodium sulfate substrate (**b**). Diagrams from Figure 4.27 are taken but without solid compositions. Solution composition at different process points are indicated as light red and blue diamonds. With green dashed areas, metastable zones are indicated.

Solid composition are spared out to set the focus on solution composition over time. The metastable limits were estimated for sodium sulfate decahydrate in presence of a sodium carbonate decahydrate substrate and vice versa. The inflection points (point 4 in Diagram (a) and point 5 in Diagram (b)) of the solution composition were taken and a parallel was drawn to the solubility line. The same assumptions were used as in Section 4.1. The width of the metastable zone of a nucleation mechanism is the same throughout the concentration range. It can be concluded from Diagram (a) that sodium carbonate decahydrate initiates nucleation of sodium sulfate decahydrate rapidly and similarly to borax and secondary seeds. The metastable zone limit lies close to the solubility line which is why solution composition inflects rather early in direction of the eutectic line (blue triangles). On the contrary, it took rather long until sodium carbonate decahydrate built nuclei on sodium sulfate substrates (Diagram (b)). Compared to other heterogeneous seeds, sodium sulfate acted positively on sodium carbonate. With respect to stratification, the examples are impactful. Solid compositions on sodium carbonate substrates are more uniform than on sodium sulfate substrates. Hence, the choice of substrates is important. In many processes, fluid deposition does not take place once but several times. Considering the findings, solid build-up will not be similar each deposition step. Thus, the composition of the solid can vary over the height of a newly formed layer. In order to predict the solidification behavior of a newly deposited liquid, a model to predict the composition of the top layer would be required.

5.2 Simulation of experiments with kinetic data

In this section, calculation results of layer build-up with concurrent crystal growth kinetics are presented. The model from the theoretical case studies in Chapter 3 is used again. The simulation set-up was adapted so that the results were consistent with the experimental results from Section 4.3. Only cooling experiments will be discussed. Both substrates and both applied cooling rates, 0.1 and 0.01 K min^{-1}, were investigated with following crystal growth kinetics obtained from crystal growth experiments in Section 4.2 (Equations 5.1).

$$\dot{n}_{\mathrm{Na_2SO_4}} = \begin{cases} 2 \cdot 10^{-6} \cdot \Delta c^{1} & \text{for Na}_2\text{SO}_4\text{-substrate} \\ 1 \cdot 10^{-7} \cdot \Delta c^{2} & \text{for Na}_2\text{CO}_3\text{-substrate} \end{cases} \tag{5.1a}$$

$$\dot{n}_{\mathrm{Na_2CO_3}} = \begin{cases} 6 \cdot 10^{-6} \cdot \Delta c^{1} & \text{for Na}_2\text{SO}_4\text{-substrate} \\ 3 \cdot 10^{-6} \cdot \Delta c^{1} & \text{for Na}_2\text{CO}_3\text{-substrate} \end{cases} \tag{5.1b}$$

Upon reaching the final temperature of 16°C, an isothermal holding time of an hour was implemented. The resulting layer compositions and final heights are merged in Figure 5.3.

Diagrams (a) and (b) show results from cooling simulations with low rates of 0.01 K min^{-1} on both substrates. The other two diagrams represent the results from higher rates of 0.1 K min^{-1}. The substrate material is indicated by the respective color below a vertical position of zero. Diagrams (a) and (c) show results for sodium sulfate decahydrate substrates and Diagrams (b) and (d) for sodium carbonate decahydrate. First of all, it is obvious that layer heights resulting from lower cooling rates were higher. This is reasonable since process times were longer. On the other hand, the layer heights in simulations with sodium sulfate substrates were 5/3 respectively 2 times higher compared with simulations with sodium carbonate substrates. This can be explained with the kinetic equations. Sodium carbonate crystallized with a rather fast kinetic as foreign component. The kinetic was even slightly faster compared to the kinetic when it acted as the substrate material. Thus, two components crystallized fast onto the surface and were able to build up the solid layer quickly. Due to the high mass transport, rather high solid layers were achieved. In simulations with sodium carbonate substrates, sodium sulfate decahydrate crystallized with an order of two and a rather small mass transfer coefficient as foreign component. Hence, at low supersaturations, its rate was low. This led to smaller phase transfer fluxes and lower layer heights. Nevertheless, the calculated final layer heights are drastically lower compared with experimentally determined layer heights. Estimated heights

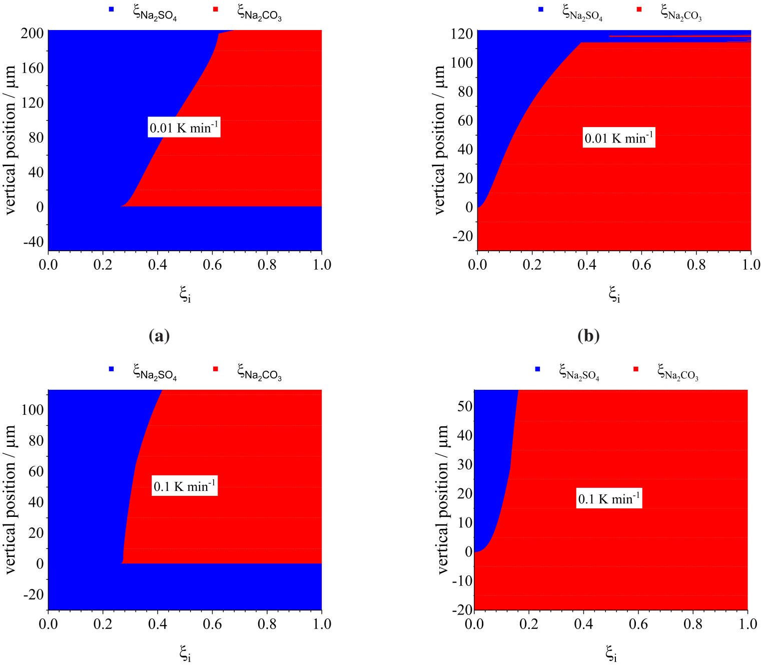

(a) (b) (c) (d)

Figure 5.3: Depiction of layer assemblages over the solid height (vertical position) resulting from crystal growth simulation. Diagrams (**a**) and (**c**) were conducted with sodium sulfate decahydrate being the substrate component. Diagrams (**b**) and (**d**) had sodium carbonate decahydrate substrates. Simulation in the first row - (**a**) and (**c**) - were cooled with a rate of 0.01 K min^{-1}, the others with a rate of 0.1 K min^{-1}.

from experiments were about eight times higher. This has to be attributed to porosities of solid layers from experiments, which were not part of the simulation set-up. However, a qualitative comparison of the calculations with experiments showed that higher cooling rates lead to lower solid thicknesses. (compare Figure 4.28).

Interpreting the results with respect to layer-wise composition, vast differences occurred in comparison with experiments. At first, simulation results on sodium sulfate substrates will be discussed (Diagrams (a) and (c)). The composition in vicinity of the substrate was dominated by sodium carbonate. From a kinetic point of view, this is obvious since both kinetics were of first order and the mass transfer coefficient of sodium carbonate slightly higher. Thus, sodium sulfate was the minor component but increased in both cases to higher positions. With slow cooling rates (Diagram (a)), it was again the major component above 100 µm and increased further up to 0.7. At higher cooling rates, the highest content of sodium sulfate was reached at the top of the solid with about 0.5. Because of the shorter process, it could not catch up with the foreign component. The experiments showed that the content of sodium carbonate was very low in first layers in the vicinity of the substrate. But afterwards, it rapidly caught up with the substrate material and exceeded it. This is to be explained with metastable states which were not part of the simulation. As stated above, the stratification experiments showed that heterogeneous nucleation of sodium carbonate due to the presence of sodium sulfate substrate needed greater supersaturations. The rapid increment of sodium carbonate in experiments can be explained very well with fast growth kinetics.

The simulation results on sodium carbonate substrates indicate a low content of foreign material in its vicinity (Diagrams (b) and (d)). At process termination with a high cooling rate (Diagram (d)), the content just reached 0.2. With slower cooling rates, the content increased from zero to 0.4 over the first 110 µm of the solid. Above it, the foreign component built a cover layer with $\xi_{Na_2SO_4} = 1$. Sodium carbonate equilibrated in solution which is why solely sodium sulfate crystallized. Some red color can still be recognized. Because of the reduction of foreign component sodium carbonate got supersaturated again and crystallized. Experiments did not show this extreme behavior (compare Figure 4.28). Sodium sulfate content increased not as fast as predicted by simulations. But indeed, the final content of foreign component was above 80% with some outliers at low cooling rates. Hence, the determined growth kinetic of sodium sulfate as foreign component does not reflect the process behavior over a greater range of supersaturation. Kinetic investigations were conducted under rather low supersaturations. In simulations, it was assumed that growth kinetics are not dependent on supersaturation. Thus, it is imaginable that sodium sulfate crystallizes with a faster kinetic at higher supersaturations which would explain the simulation results.

In a nutshell, the comparison of the experimental studies and theoretical considerations lead to following the suggestions in handling solid formation from multi-component solutions:

1. Phase equilibria and respective metastable zone limits - especially from heterogeneous nucleation - have to be determined. Metastable zone limits are needed to predict if and at which supersaturation nuclei of the foreign component are likely formed.
2. Secondary nucleation has to be analyzed in order to run the process without unintended nucleation.
3. Concurrent growth kinetics have to be investigated. Based on these results, it is already possible to predict final solid assemblages qualitatively.

With this, knowledge based choice of process conditions dependent on the intended composition is possible.

6 Summary and Outlook

The aim of this work was to give the reader a knowledge based strategy to approach layer build-up from multi-component solutions. For that purpose, influencing factors have to be identified. From theoretical considerations, three impact groups can be distinguished, i.e. phase equilibrium and metastable states, phase transfer kinetics, and supersaturation rate. In case studies, these groups may be characterized on their specific influence on final layer assemblages.

Based on these simulations, experimental set-ups had to be developed and established to investigate the groups under realistic conditions. To find general conclusions, the model material system Na_2SO_4-Na_2CO_3-H_2O was used in all experimental studies. All simulation studies were based on its properties. Because of the well-known phase equilibrium - which can also be calculated with appropriate databases based on activity models - the focus of the first group lay on metastable zones. A method was developed which made it possible to investigate metastable zone widths from homogeneous nucleation by a pseudo-binary approach. Nucleation points of eight saturated solutions with different compositions were identified from polythermal measurements. The highest nucleation temperature was taken as the metastable limit. With the assumption that $\Delta x_{\text{met}}/\Delta T_{\text{met}} = \partial x/\partial T$ holds for ternary solutions with the mass fraction of one component being constant, the metastable temperature difference ΔT_{met} was transformed into the metastable supersaturation Δx_{met}. With Δx_{met}, it was possible to define metastable zone limits. Nevertheless, the reproducibility of the metastable zones with drying experiments of three different solutions was not possible. Hence, Hypothesis II - Metastable zones of ternary systems can be predicted by a pseudo-binary approach - could not be verified completely. It should be investigated further because it promises to be a method to determine metastable zones in a small amount of time.

Since homogeneous nucleation was not identified as a key factor on layer build-up, heterogeneous and secondary nucleation were considered. Due to the solubility of both components in water, borax was chosen as heterogeneous seeding agent. Due to the similar lattice parameters, it was assumed that it is able to promote nucleation of both sodium sulfate and sodium carbonate. Nevertheless, only sodium sulfate decahydrate could build nuclei while sodium carbonate remained dissolved. Hence, the conclusion was drawn that heterogeneous seeds or substrate materials play a key role in affecting layer build-up. From secondary nucleation, it was found that both electrolytes crystallized even at very low supersaturations. This had to be taken into account for the set-up of the subsequent experimental methods.

In case studies, it was shown that crystal growth kinetics are of great importance, especially if kinetics between concurrent crystallizing components differ greatly. To investigate crystal growth kinetics of various materials from highly saturated solutions, a new method was developed and established. Concentration depletion of a thin liquid film in contact with a crystalline substrate was measured. Because nucleation had to be prevented to attribute concentration changes to crystal growth, initial subcooling was limited to $\Delta T = 3$ K in order to avoid nucleation. With this, initial supersaturations of at maximum $S_{\mathrm{Na_2SO_4}} = 1.09$ and $S_{\mathrm{Na_2CO_3}} = 1.06$ were achieved.

The experiments could identify two distinctive cases of multi-component crystallization. In the majority of experiments, concurrent crystallization was observed. While the substrate component always crystallized with an order of $g = 1$, their mass transfer coefficient was lower than the ternary diffusion mass transfer coefficient. This led to the conclusion that the substrate component was limited in its integration process due to the foreign component. The respective foreign components showed different behaviors on the respective substrates. While sodium carbonate decahydrate crystallized on sodium sulfate decahydrate similarly compared to its own substrate, sodium sulfate decahydrate was strongly influenced. The order of crystallization changed to $g = 2$, which indicated a stronger integration resistance. The conclusion of the described behavior for the resulting layer is that sodium sulfate decahydrate substrates would generate a mostly homogeneous solid layer due to similar kinetics of both components. On the other hand, multicomponent crystallization on sodium carbonate decahydrate substrates would lead to stratification because the substrate component would crystallize faster than the foreign component. Hence, the latter would be the major component in top layers. Other than simultaneous crystallization, material separation was observed in few experiments. Solely the substrate component solidified and the foreign component remained metastable in solution until the end of experiment. The effect on the mass transfer kinetic was immense. Due to the fact that the foreign material leveled up in solution, the mass transfer coefficient of the other component was reduced to the tenth of diffusion mass transfer coefficient. Similarly to the significantly slower kinetics of concurrent crystallization, the observation of material separation would lead to a highly stratified solid assemblage. Due to its supersaturation, metastable foreign material could crystallize onto the pure lower layers of substrate material.

Hence, a method was found, with which it is possible to verify Hypothesis III - Kinetics of multiple crystallizing materials can be measured simultaneously and independently.

The influence of supersaturation rate on layer build-up was investigated at two cooling and drying rates. Relatively low supersaturation rates were investigated because of the fact that secondary nucleation had to be prevented. Higher rates would have led to spontaneous nucleation and growth spots other than the substrate. The experiments on cooling rates brought up similar conclusions as were already made from case study simulations. Supersaturation rate did not have the strong impact as was imagined from theoretical reflection. Therefore, Hypothesis IV - The rate of supersaturation build-up has an impact on the final layer assemblage - could not be verified. Cooling rates would mostly have an influence on final solid height. This effect was attributed to the shorter process time of higher cooling rates. The layer assemblage did not show significant changes in stratification behavior if different cooling rates were used and all other parameters were kept constant. In addition to the layer compositions, the solution compositions that prevailed at the time a solid layer was formed were also theoretically determined. With it, it was possible to show how substrates acted as heterogeneous nuclei on dissolved foreign components in solution. Sodium carbonate decahydrate drove crystallization of sodium sulfate decahydrate faster which resulted in a lesser supersaturation of foreign component. In consequence, the produced layers were more homogeneous than layers resulting with a similar initial solution on sodium sulfate decahydrate. This was due to significantly higher developing supersaturation of foreign component sodium carbonate which in turn was the result of weaker influence of sodium sulfate decahydrate as heterogeneous seed.

These findings lead to the conclusion that the general research Hypothesis I - Multi-component crystallization from solution on crystalline substrates provokes a stratified surface - is valid but depends mostly on phase equilibrium behavior and on the concurrent crystallization kinetics. Supersaturation rates do not impact the stratification as much as it was assumed.

A strategy on multi-component crystallization could be deduced, which can either be used for product design of particles in granulation or coating processes or other related processes with multiple components dissolved in solution. At first, the phase equilibrium and ideally the metastable zones should be investigated. Therefor the proposed method from Section 2.2 has shown its capability. It can be easily adapted to other material systems and offers the possibility of determining the unknowns in a time-uncomplicated manner. Especially heterogeneous and secondary nucleation are of great interest. Hence, appropriate heterogeneous seeds have to be found which show similar properties as used entities. Experiments on secondary nucleation will show to what point the supersaturation of the process can be increased. This is mainly of interest if coating solutions are dried. At gas-liquid interface, the highest supersaturation occurs. If it exceeds secondary nucleation metastable limit, nuclei will arise which are able to build a cover layer. That would prevent drying of residual solution. First ideas of stratification behavior can already be drawn from these results. Phase transfer kinetics of all stable solids in the temperature range have to be investigated. Ideally, compositions are used at which at least two solid entities are stable. Hence, concurrent crystallization would be possible. Stratification experiments can be conducted to investigate possible process parameters and their influence on the solid material assemblage. Also, these experiments could bring up knowledge of heterogeneous seeding behavior. If the solubility properties of a material system are similar to Na_2SO_4-Na_2CO_3-H_2O, this could be necessary.

In order to predict solid layer assemblages mathematically, it was not possible to run calculations replicating experimental results (compare Chapter 5). In particular, metastable states could not be implemented in the model, which were interpreted as the reason for the strong deviations. Hence, metastability data cannot be neglected but should be part of the simulation and not only thermodynamic and kinetic data. Furthermore, the growth from solution onto freshly built solid mixtures would be of great interest. Especially with respect to granulation or coating processes, this gives the opportunity to predict solid assemblages after several subsequent fluid depositions. For this, growth experiments with substrates consisting of various solid mixtures have to be conducted to investigate growth kinetics dependent on the substrate composition. Additionally, the influence of other phase equilibria in form of more than two solid entities would generate important knowledge of stratification behavior for practical application of technical material systems.

Bibliography

A. Al-Gailani, O. Sanni, T. V. J. Charpentier, R. Crisp, J. H. Bruins, and A. Neville. Examining the effect of ionic constituents on crystallization fouling on heat transfer surfaces. *International Journal of Heat and Mass Transfer*, 160: 120180, 2020. ISSN 0017-9310.

C. Bayuadri, C. L. Verrill, and R. W. Rousseau. Stability of sodium sulfate dicarbonate ($\sim 2Na_2CO_3 \cdot Na_2SO_4$) crystals obtained from evaporation of aqueous solutions of Na_2CO_3 and Na_2SO_4. *Industrial & Engineering Chemistry Research*, 45(21):7144–7150, 2006. ISSN 0888-5885.

B. Beig, M. B. K. Niazi, Z. Jahan, A. Hussain, M. H. Zia, and M. T. Mehran. Coating materials for slow release of nitrogen from urea fertilizer: A review. *Journal of Plant Nutrition*, 43(10):1510–1533, 2020. ISSN 0190-4167.

S. A. Belyakov and C. M. Gourlay. Heterogeneous nucleation of βSn on $NiSn_4$, $PdSn_4$ and $PtSn_4$. *Acta materialia*, 71:56–68, 2014. ISSN 1359-6454.

A. Berthoud. Formation of crystal faces. *J. Chem. Phys*, 10:624–635, 1912.

S. K. Bhattacharia, N. Hossain, and C.-C. Chen. Thermodynamic modeling of aqueous Na^+-K^+-SO_4^{2-}- quaternary system with electrolyte NRTL model. *Fluid Phase Equilibria*, 403:1–9, 2015. ISSN 0378-3812.

C. Borchert, E. Temmel, H. Eisenschmidt, H. Lorenz, A. Seidel-Morgenstern, and K. Sundmacher. Image-based in situ identification of face specific crystal growth rates from crystal populations. *Crystal Growth & Design*, 14(3):952–971, 2014. ISSN 1528-7483.

A. Borsos, A. Majumder, and Z. K. Nagy. Multi-impurity adsorption model for modeling crystal purity and shape evolution during crystallization processes in impure media. *Crystal Growth & Design*, 16(2):555–568, 2016. ISSN 1528-7483.

C. H. Bovington and A. L. Jones. Tracer study of the kinetics of dissolution of barium sulphate. *Transactions of the Faraday Society*, 66:764–768, 1970.

S. Boyd, K. Back, K. Chadwick, R. J. Davey, and C. C. Seaton. Solubility metastable zone width measurement and crystal growth of the 1: 1 benzoic acid/isonicotinamide cocrystal in solutions of variable stoichiometry. *Journal of pharmaceutical sciences*, 99(9):3779–3786, 2010. ISSN 0022-3549.

G. Brenn. *Analytical solutions for transport processes*. Springer, 2016. ISBN 3662514214.

W.-K. Burton, N. Cabrera, and F. C. Frank. The growth of crystals and the equilibrium structure of their surfaces. *Philosophical Transactions of the Royal Society of London. Series A, Mathematical and Physical Sciences*, 243(866): 299–358, 1951. ISSN 0080-4614.

W. A. Caspari. CCCXXIV.—the system sodium carbonate–sodium sulphate–water. *Journal of the Chemical Society, Transactions*, 125:2381–2387, 1924.

K. Chadwick, A. Myerson, and B. Trout. Polymorphic control by heterogeneous nucleation-a new method for selecting crystalline substrates. *CrystEngComm*, 13(22):6625–6627, 2011.

J. Cornel and M. Mazzotti. Estimating crystal growth rates using in situ ATR-FTIR and Raman spectroscopy in a calibration-free manner. *Industrial & Engineering Chemistry Research*, 48(23):10740–10745, 2009. ISSN 0888-5885.

J. Cornel, C. Lindenberg, and M. Mazzotti. Quantitative application of in situ ATR-FTIR and Raman spectroscopy in crystallization processes. *Industrial & Engineering Chemistry Research*, 47(14):4870–4882, 2008. ISSN 0888-5885.

A. J. Cruz-Cabeza, G. M. Day, and W. Jones. Towards prediction of stoichiometry in crystalline multicomponent complexes. *Chemistry–A European Journal*, 14 (29):8830–8836, 2008. ISSN 0947-6539.

Y. Cui and A. S. Myerson. Experimental evaluation of contact secondary nucleation mechanisms. *Crystal Growth & Design*, 14(10):5152–5157, 2014. ISSN 1528-7483.

C. Darmali, S. Mansouri, N. Yazdanpanah, and M. W. Woo. Mechanisms and control of impurities in continuous crystallization: a review. *Industrial & Engineering Chemistry Research*, 58(4):1463–1479, 2018. ISSN 0888-5885.

J. Degrève, J. Baeyens, M. van de Velden, and S. de Laet. Spray-agglomeration of NPK-fertilizer in a rotating drum granulator. *Powder Technology*, 163(3): 188–195, 2006. ISSN 0032-5910.

C. Eder, C. Choscz, V. Müller, and H. Briesen. Jamin-interferometer-setup for the determination of concentration and temperature dependent face-specific crystal growth rates from a single experiment. *Journal of crystal growth*, 426: 255–264, 2015. ISSN 0022-0248.

Z. Fan. An epitaxial model for heterogeneous nucleation on potent substrates. *Metallurgical and Materials Transactions A*, 44(3):1409–1418, 2013. ISSN 1073-5623.

J. R. Ferraro. *Introductory raman spectroscopy*. Elsevier, 2003. ISBN 0080509126.

J. Fu, C. Wang, X. Chen, Z. Huang, and D. Chen. Classification research and types of slow controlled release fertilizers (SRFs) used-a review. *Communications in soil science and plant analysis*, 49(17):2219–2230, 2018. ISSN 0010-3624.

E. N. Fuller, P. D. Schettler, and J. C. Giddings. New method for prediction of binary gas-phase diffusion coefficients. *Industrial & Engineering Chemistry*, 58(5):18–27, 1966.

J. Garside and R. J. Davey. Invited review secondary contact nucleation: kinetics, growth and scale-up. *Chemical Engineering Communications*, 4(4-5):393–424, 1980. ISSN 0098-6445.

J. Garside, A. Mersmann, and J. Nývlt. *Measurement of crystal growth and nucleation rates*. IChemE, 2002. ISBN 0852954492.

H. Glade, A. M. Ilyaskarov, and J. Ulrich. Determination of crystal growth kinetics using ultrasonic technique. *Chemical Engineering & Technology*, 27 (7):736–740, 2004. ISSN 09307516.

J. D.S. Goulden. Infra-red spectroscopy of aqueous solutions. *Spectrochimica Acta*, 15:657–671, 1959. ISSN 0371-1951.

M. Gourdon, L. Vamling, U. Andersson, and L. Olausson. Crystallization in a pilot evaporator: Aqueous solutions of Na_2CO_3 and Na_2SO_4. *Industrial & Engineering Chemistry Research*, 49(5):2401–2409, 2010. ISSN 0888-5885.

A. Gupta, S. Shim, L. Issah, C. McKenzie, and H. A. Stone. Diffusion of multiple electrolytes cannot be treated independently: model predictions with experimental validation. *Soft matter*, 15(48):9965–9973, 2019.

E. L. Hahn. Spin echoes. *Physical review*, 80(4):580, 1950.

C. Helfenritter and M. Kind. Determination of crystal growth rates in multi-component solutions. *Crystals*, 12(11):1568, 2022a.

C. Helfenritter and M. Kind. Multi-component diffusion in the vicinity of a growing crystal. *Crystals*, 12(6):872, 2022b.

K. Higashi, K. Ueda, and K. Moribe. Recent progress of structural study of polymorphic pharmaceutical drugs. *Advanced Drug Delivery Reviews*, 117: 71–85, 2017. ISSN 0169-409X.

F. F. Hingerl, T. Wagner, D. A. Kulik, K. Thomsen, and T. Driesner. A new aqueous activity model for geothermal brines in the system Na-K-Ca-Mg-H-Cl-SO_4-H_2O from 25 to 300°C. *Chemical Geology*, 381:78–93, 2014. ISSN 0009-2541.

C. W. Hirt and B. D. Nichols. Volume of fluid (VOF) method for the dynamics of free boundaries. *Journal of computational physics*, 39(1):201–225, 1981. ISSN 0021-9991.

S. P. Jakobsson and J. G. Moore. Hydrothermal minerals and alteration rates at surtsey volcano, iceland. *Geological Society of America Bulletin*, 97(5): 648–659, 1986. ISSN 1943-2674.

E. Jänecke. Über eine neue Darstellungsform der wässerigen Lösungen zweier und dreier gleichioniger Salze, reziproker Salzpaare und der van't Hoffschen Untersuchungen über ozeanische Salzablagerungen. *Zeitschrift für anorganische und allgemeine Chemie*, 51(1):132–157, 1906. ISSN 1521-3749.

X. Jiang, M. Li, G. He, and J. Wang. Research progress and model development of crystal layer growth and impurity distribution in layer melt crystallization: A review. *Industrial & Engineering Chemistry Research*, 53(34):13211–13227, 2014. ISSN 0888-5885.

N. Kanzaki, K. Onuma, A. Ito, K. Teraoka, T. Tateishi, and S. Tsutsumi. Direct growth rate measurement of hydroxyapatite single crystal by moire phase shift interferometry. *The Journal of Physical Chemistry B*, 102(34):6471–6476, 1998. ISSN 1520-6106.

E. Karlsson, M. Gourdon, L. Olausson, and L. Vamling. Crystallization fouling of sodium salts in black liquor falling film evaporators – development of experimental method and first results. *Nordic Pulp & Paper Research Journal*, 28 (4):506–513, 2013.

G. Katona, B. Szalontai, M. Budai-Szűcs, E. Csányi, P. Szabó-Révész, and O. Jójárt-Laczkovich. Formulation of paracetamol-containing pastilles with in situ coating technology. *European journal of pharmaceutical sciences*, 95: 54–61, 2016. ISSN 0928-0987.

J-W Kim and J. Ulrich. Development of a new coating process in pharmaceutical industry by crystallization. *Engineering in life sciences*, 3(3):121–126, 2003. ISSN 1618-0240.

J.-Y. Kim, D.-W. Kim, Y.-M. Kuk, C.-W. Park, Y.-S. Rhee, T.-O. Oh, K.-Y. Weon, and E.-S. Park. Investigation of an active film coating to prepare new fixed-dose combination tablets for treatment of diabetes. *International journal of pharmaceutics*, 427(2):201–208, 2012. ISSN 0378-5173.

S. U. Kim and V. Srinivasan. A method for estimating transport properties of concentrated electrolytes from self-diffusion data. *Journal of The Electrochemical Society*, 163(14):A2977, 2016. ISSN 1945-7111.

M. Kochba, S. Gambash, and Y. Avnimelech. Studies on slow release fertilizers: 1. Effects of temperature, soil moisture, and water vapor pressure. *Soil Science*, 149(6):339–343, 1990. ISSN 0038-075X.

W. Kossel. Zur Theorie des Kristallwachstums. *Nachrichten von der Gesellschaft der Wissenschaften zu Göttingen, Mathematisch-Physikalische Klasse*, 1927: 135–143, 1927.

R. Krishna and J. M. van Baten. The darken relation for multicomponent diffusion in liquid mixtures of linear alkanes: An investigation using molecular dynamics (MD) simulations. *Industrial & Engineering Chemistry Research*, 44(17): 6939–6947, 2005. ISSN 0888-5885.

R. Krishna and J.A. Wesselingh. The Maxwell-Stefan approach to mass transfer. *Chemical Engineering Science*, 52(6):861–911, 1997.

N. Kubota. Effect of impurities on the growth kinetics of crystals. *Crystal Research and Technology: Journal of Experimental and Industrial Crystallography*, 36 (8–10):749–769, 2001. ISSN 0232-1300.

W. Kümmel. *Technische Strömungsmechanik: Theorie und Praxis*. Springer-Verlag, 2013. ISBN 3322927776.

D. Lawrencia, S. K. Wong, D. Y. S. Low, B. H. Goh, J. K. Goh, U. R. Ruktanonchai, A. Soottitantawat, L. H. Lee, and S. Y. Tang. Controlled release fertilizers: A review on coating materials and mechanism of release. *Plants*, 10(2):238, 2021.

E. Libowitzky and G. Giester. Washing soda (natron), na 2 co 3· 10h 2 o, revised: Crystal structures at low and ambient temperatures. *Mineralogy and Petrology*, 77:177–195, 2003.

T. H. Lilley. Raman spectroscopy of aqueous electrolyte solutions. In *Aqueous Solutions of Simple Electrolytes*, pages 265–299. Springer, 1973.

X. Liu, S. K. Schnell, J.-M. Simon, P. Krüger, D. Bedeaux, S. Kjelstrup, A. Bardow, and T. J. H. Vlugt. Diffusion coefficients from molecular dynamics simulations in binary and ternary mixtures. *International Journal of Thermophysics*, 34(7):1169–1196, 2013. ISSN 0195-928X.

H. Lorenz, A. Perlberg, D. Sapoundjiev, M. P. Elsner, and A. Seidel-Morgenstern. Crystallization of enantiomers. *Chemical Engineering and Processing: Process Intensification*, 45(10):863–873, 2006. ISSN 0255-2701.

I. Ludwig, W. Schabel, M. Kind, J-C Castaing, and P. Ferlin. Drying and film formation of industrial waterborne latices. *AIChE journal*, 53(3):549–560, 2007. ISSN 1547-5905.

Y. Lv, K. Lu, and Y. Ren. Composite crystallization fouling characteristics of normal solubility salt in double-pipe heat exchanger. *International Journal of Heat and Mass Transfer*, 156:119883, 2020. ISSN 0017-9310.

G. M. Marion, M. V. Mironenko, and M. W. Roberts. Frezchem: A geochemical model for cold aqueous solutions. *Computers & Geosciences*, 36(1):10–15, 2010. ISSN 0098-3004.

S. A. Markgraf and R. J. Reeder. High-temperature structure refinements of calcite and magnesite. *American Mineralogist*, 70(5-6):590–600, 1985.

H. Martin. Heat and mass transfer between impinging gas jets and solid surfaces. In *Advances in heat transfer*, volume 13, pages 1–60. Elsevier, 1977. ISBN 0065-2717.

H. Martin and M. Saberian. Improved asymptotic approximations for transient conduction and diffusion processes. *Chemical Engineering and Processing: Process Intensification*, 33(4):205–210, 1994. ISSN 0255-2701.

H. Martin, T. Wetzel, and B. Dietrich. E2 Wärmeleitung – instationär. In P. Stephan, S. Kabelac, M. Kind, D. Mewes, K. Schaber, and T. Wetzel, editors, *VDI-Wärmeatlas*, Springer Reference Technik, pages 729–755. Springer Berlin Heidelberg, Berlin, Heidelberg, 2019. ISBN 978-3-662-52988-1.

A. Mersmann. *Crystallization technology handbook.* CRC press, 2001. ISBN 0203908287.

N. Morimoto. The crystal structure of borax. *Mineralogical Journal*, 2(1):1–18, 1956.

M. Müller, M. Kind, R. Cairncross, and W. Schabel. Diffusion in multi-component polymeric systems: Diffusion of non-volatile species in thin films. *The European Physical Journal Special Topics*, 166(1):103–106, 2009. ISSN 1951-6355.

J. W. Mullin. *Crystallization.* Elsevier, 2001. ISBN 0080530117.

E. N. E. M. Nasir, F. Ab Rahman, S. Abd Rahim, R. Z. Edros, and N. Anuar. Preliminary study on operating parameters toward the metastable zone-width of carbamazepine co-crystal. *Indian Journal of Science and Technology*, 10 (7), 2017. ISSN 0974-5645.

A. E. Nielsen. Electrolyte crystal growth mechanisms. *Journal of crystal growth*, 67(2):289–310, 1984. ISSN 0022-0248.

J. M. Nielsen, A. W. Adamson, and J. W. Cobble. The self-diffusion coefficients of the ions in aqueous sodium chloride and sodium sulfate at 25°C. *Journal of the American Chemical Society*, 74(2):446–451, 1952. ISSN 0002-7863.

M. R. Nielsen, K. K. Sand, J. D. Rodriguez-Blanco, N. Bovet, J. Generosi, K. N. Dalby, and S. L.S. Stipp. Inhibition of calcite growth: combined effects of Mg^{2+} and $SO_4{}^{2-}$. *Crystal Growth & Design*, 16(11):6199–6207, 2016. ISSN 1528-7483.

J. Nijdam, S. Kachel, P. Scharfer, W. Schabel, and M. Kind. Effect of diffusion on component segregation during drying of aqueous solutions containing protein and sugar. *Drying Technology*, 33(3):288–300, 2015. ISSN 0737-3937.

J. Nyvlt. *Kinetics of industrial crystallization.* Elsevier Science Pub. Co., Inc., 1984. ISBN 0444996109.

H. Offermann, G. von Brachel, A. Al-Sabbagh, and F. Farelo. Crystallization kinetics of NaCl in multicomponent solutions. *Crystal Research and Technology*, 30(5):651–658, 1995. ISSN 1521-4079.

R. T. Pabalan and K. S. Pitzer. Thermodynamics of concentrated electrolyte mixtures and the prediction of mineral solubilities to high temperatures for mixtures in the system Na-K-Mg-Cl-SO_4-OH-H_2O. *Geochimica et Cosmochimica Acta*, 51(9):2429–2443, 1987. ISSN 0016-7037.

M. Parisi and A. Chianese. The crystal layer growth from a well-mixed melt. *Chemical Engineering Science*, 56(14):4245–4256, 2001. ISSN 0009-2509.

D. L. Parkhurst and C.A.J. Appelo. Description of input and examples for phreeqc version 3—a computer program for speciation, batch-reaction, one-dimensional transport, and inverse geochemical calculations. *US geological survey techniques and methods*, 6(A43):497, 2013.

N. Pawar, A. Saha, N. Nandan, and J. V. Parambil. Solution cocrystallization: A scalable approach for cocrystal production. *Crystals*, 11(3):303, 2021.

F. M. Penha, F. R. D. Andrade, A. S. Lanzotti, P. F. Moreira Junior, G. P. Zago, and M. M. Seckler. In situ observation of epitaxial growth during evaporative simultaneous crystallization from aqueous electrolytes in droplets. *Crystals*, 11(9):1122, 2021.

K. S. Pitzer. Ion interaction approach: theory and data correlation. In *Activity coefficients in electrolyte solutions*, pages 75–153. CRC Press, 2018.

D. Polenske and H. Lorenz. Solubility and metastable zone width of the methionine enantiomers and their mixtures in water. *Journal of Chemical & Engineering Data*, 54(8):2277–2280, 2009. ISSN 0021-9568.

B. K. Purohit and V. S. Sistla. Study on suitability of laponite–based aqueous Na_2SO_4 solution incorporated foam as latent heat storage medium. *International Journal of Energy Research*, 45(3):3999–4013, 2021. ISSN 0363-907X.

R.-Y. Qian and G. D. Botsaris. A new mechanism for nuclei formation in suspension crystallizers: the role of interparticle forces. *Chemical Engineering Science*, 52(20):3429–3440, 1997. ISSN 0009-2509.

R.-Y. Qian and G. D. Botsaris. Nuclei breeding from a chiral crystal seed of $NaClO_3$. *Chemical Engineering Science*, 53(9):1745–1756, 1998. ISSN 0009-2509.

M. Rauls, K. Bartosch, M. Kind, R. Lacmann, and A. Mersmann. The influence of impurities on crystallization kinetics–a case study on ammonium sulfate. *Journal of Crystal Growth*, 213(1-2):116–128, 2000. ISSN 0022-0248.

E. Römbach and J. Ulrich. Self-controlled coating process for drugs. *Crystal Growth & Design*, 7(9):1618–1622, 2007. ISSN 1528-7483.

A. F. Routh. Drying of thin colloidal films. *Reports on Progress in Physics*, 76 (4):046603, 2013. ISSN 0034-4885.

H. W. Ruben, D. H. Templeton, R. D. Rosenstein, and I. Olovsson. Crystal structure and entropy of sodium sulfate decahydrate. *Journal of the American Chemical Society*, 83(4):820–824, 1961.

K. Sangwal. Effect of impurities on the metastable zone width of solute–solvent systems. *Journal of Crystal Growth*, 311(16):4050–4061, 2009. ISSN 0022-0248.

K. Sangwal. On the effect of impurities on the metastable zone width of phosphoric acid. *Journal of Crystal Growth*, 312(22):3316–3325, 2010. ISSN 0022-0248.

K. Sangwal. Recent developments in understanding of the metastable zone width of different solute− solvent systems. *Journal of crystal growth*, 318(1):103–109, 2011. ISSN 0022-0248.

A. Sanjay, D. Manohar, and S. R. Bhanudas. Pharmaceutical cocrystallization: a review. *India: Journal of Advanced Pharmacy Education & Research*, 4(4), 2014.

P. Scharfer, W. Schabel, and M. Kind. Mass transport measurements in membranes by means of in situ Raman spectroscopy—first results of methanol and water profiles in fuel cell membranes. *Journal of Membrane Science*, 303(1):37–42, 2007. ISSN 0376-7388.

E.-U. Schlünder. Über die Brauchbarkeit des Newtonschen Abkühlungsgesetzes im Lichte der Fourierschen Wärmeleitungstheorie. *Wärme-und Stoffübertragung*, 5(1):9–14, 1972. ISSN 1432-1181.

C. Schmidt, M. J. Jones, and J. Ulrich. The influence of additives and impurities on crystallization. *Crystallization: Basic Concepts and Industrial Applications*, pages 105–127, 2013.

M. Schulz and J. L. Keddie. A critical and quantitative review of the stratification of particles during the drying of colloidal films. *Soft matter*, 14(30):6181–6197, 2018.

K.-S. Seo and H.-K. Han. Multilayer-coated tablet of clopidogrel and rosuvastatin: Preparation and in vitro/in vivo characterization. *Pharmaceutics*, 11(7):313, 2019.

K.-S. Seo, R. Bajracharya, S. H. Lee, and H.-K. Han. Pharmaceutical application of tablet film coating. *Pharmaceutics*, 12(9):853, 2020.

A. Shaviv. Advances in controlled-release fertilizers. *0065-2113*, 2001. ISSN 0065-2113.

O. Shemchuk, L. Song, N. Tumanov, J. Wouters, D. Braga, F. Grepioni, and T. Leyssens. Chiral resolution of RS-oxiracetam upon cocrystallization with pharmaceutically acceptable inorganic salts. *Crystal Growth & Design*, 20(4): 2602–2607, 2020. ISSN 1528-7483.

B. Shi and R. W. Rousseau. Crystal properties and nucleation kinetics from aqueous solutions of Na_2CO_3 and Na_2SO_4. *Industrial & Engineering Chemistry Research*, 40(6):1541–1547, 2001. ISSN 0888-5885.

B. Shi, W. J. Frederick, and R. W. Rousseau. Nucleation, growth, and composition of crystals obtained from solutions of Na_2CO_3 and Na_2SO_4. *Industrial & Engineering Chemistry Research*, 42(25):6343–6347, 2003. ISSN 0888-5885.

K. S. Song, J. Lim, S. Yun, D. Kim, and Y. Kim. Composite fouling characteristics of $CaCO_3$ and $CaSO_4$ in plate heat exchangers at various operating and geometric conditions. *International Journal of Heat and Mass Transfer*, 136: 555–562, 2019. ISSN 0017-9310.

J.J. Sousa, A. Sousa, M.J. Moura, F. Podczeck, and J.M. Newton. The influence of core materials and film coating on the drug release from coated pellets. *International Journal of Pharmaceutics*, 233(1):111–122, 2002. ISSN 0378-5173.

E. O. Stejskal and J. E. Tanner. Spin diffusion measurements: spin echoes in the presence of a time–dependent field gradient. *The Journal of Chemical Physics*, 42(1):288–292, 1965. ISSN 0021-9606.

P. Stephan, S. Kabelac, M. Kind, D. Mewes, K. Schaber, and T. Wetzel, editors. *VDI-Wärmeatlas*. Springer Reference Technik. Springer Berlin Heidelberg, Berlin, Heidelberg, 2019. ISBN 978-3-662-52988-1.

C. C. Sun. Cocrystallization for successful drug delivery. *Expert Opinion on Drug Delivery*, 10(2):201–213, 2013. ISSN 1742-5247.

S. Sun, H. Zhang, J. Xu, S. Wang, H. Wang, Z. Yu, L. Zhao, C. Zhu, and J. Sun. The competition between cocrystallization and separated crystallization based on crystallization from solution. *Journal of Applied Crystallography*, 52(4): 769–776, 2019. ISSN 0021-8898.

P. Suresh, I. Sreedhar, R. Vaidhiswaran, and A. Venugopal. A comprehensive review on process and engineering aspects of pharmaceutical wet granulation. *Chemical Engineering Journal*, 328:785–815, 2017. ISSN 1385-8947. doi: 10.1016/j.cej.2017.07.091.

C. Y. Tai, J.-F. Wu, and R. W. Rousseau. Interfacial supersaturation, secondary nucleation, and crystal growth. *Journal of Crystal Growth*, 116(3-4):294–306, 1992. ISSN 0022-0248.

S. Tait, W. P. Clarke, J. Keller, and D. J. Batstone. Removal of sulfate from high-strength wastewater by crystallisation. *Water Research*, 43(3):762–772, 2009. ISSN 0043-1354.

R. Taylor and R. Krishna. *Multicomponent mass transfer*, volume 2. John Wiley & Sons, 1993. ISBN 0471574171.

M. Telkes. Nucleation of supersaturated inorganic salt solutions. *Industrial & Engineering Chemistry*, 44(6):1308–1310, 1952. ISSN 0019-7866.

K. Thomsen, P. Rasmussen, and R. Gani. Correlation and prediction of thermal properties and phase behaviour for a class of aqueous electrolyte systems. *Chemical Engineering Science*, 51(14):3675–3683, 1996. ISSN 0009-2509.

S. Titiz-Sargut and J. Ulrich. Influence of additives on the width of the metastable zone. *Crystal Growth & Design*, 2(5):371–374, 2002. ISSN 1528-7483.

J.D. Toner and R.S. Sletten. The formation of Ca-Cl enriched groundwaters in the dry valleys of antarctica by cation exchange reactions: field measurements and modeling of reactive transport. *Geochim. Cosmochim. Acta*, 110:84–105, 2013.

G. I. Tóth, G. Tegze, T. Pusztai, and L. Gránásy. Heterogeneous crystal nucleation: the effect of lattice mismatch. *Physical review letters*, 108(2):025502, 2012.

R. E. Trueman, E. Lago Domingues, S. N. Emmett, M. W. Murray, and Routh. Auto-stratification in drying colloidal dispersions: A diffusive model. *Journal of Colloid and Interface Science*, 377(1):207–212, 2012. ISSN 0021-9797.

J. Ulrich and P. Frohberg. Problems, potentials and future of industrial crystallization. *Frontiers of Chemical Science and Engineering*, 7(1):1–8, 2013. ISSN 2095-0179.

S. Ummadi, B. Shravani, N. R. Rao, M. S. Reddy, and B. Sanjeev. Overview on controlled release dosage form. *System*, 7(8):51–60, 2013.

S. J. Urwin, S. Yerdelen, I. Houson, and J. H. ter Horst. Impact of impurities on crystallization and product quality: a case study with paracetamol. *Crystals*, 11(11):1344, 2021.

J. J.P. Valeton. I. Wachstum und Auflösung der Kristalle. III. *Zeitschrift für Kristallographie-Crystalline Materials*, 60(1-6):1–38, 1924. ISSN 2196-7105.

M. van der Leeden, G. van Rosmalen, K. De Vreugd, and G. Witkamp. Einfluß von Additiven und Verunreinigungen auf Kristallisationsprozesse. *Chemie Ingenieur Technik*, 61(5):385–395, 1989. ISSN 1522-2640.

A. I. Vavouraki and P. G. Koutsoukos. Kinetics of crystal growth of mirabilite in aqueous supersaturated solutions. *Journal of Crystal Growth*, 338(1):189–194, 2012. ISSN 0022-0248.

A. I. Vavouraki and P. G. Koutsoukos. The inhibition of crystal growth of mirabilite in aqueous solutions in the presence of phosphonates. *Journal of Crystal Growth*, 436:92–98, 2016. ISSN 0022-0248.

M. Volmer. Kinetics of phase formation (Kinetik der Phasenbildung), 1939.

G. M. Walker, C. R. Holland, M. N. Ahmad, J. N. Fox, and A. G. Kells. Drum granulation of NPK fertilizers. *Powder Technology*, 107(3):282–288, 2000. ISSN 0032-5910.

J. H. Wang. Self-diffusion coefficients of water. *The Journal of Physical Chemistry*, 69(12):4412, 1965. ISSN 0022-3654.

K. Wu, C. Y. Ma, J. J. Liu, Y. Zhang, and X. Z. Wang. Measurement of crystal face specific growth kinetics. *Crystal Growth & Design*, 16(9):4855–4868, 2016. ISSN 1528-7483.

S. Xu, Z. Hou, X. Chuai, and Y. Wang. Overview of secondary nucleation: From fundamentals to application. *Industrial & Engineering Chemistry Research*, 59(41):18335–18356, 2020. ISSN 0888-5885.

B. Xuan, S. N. Wong, Y. Zhang, J. Weng, H. H. Y. Tong, C. Wang, C. C. Sun, and S. F. Chow. Extended release of highly water soluble isoniazid attained through cocrystallization with curcumin. *Crystal Growth & Design*, 20(3):1951–1960, 2020. ISSN 1528-7483.

H. Yang and A. J. Florence. Relating induction time and metastable zone width. *CrystEngComm*, 19(28):3966–3978, 2017.

N. Yazdanpanah, A. Myerson, and B. Trout. Mathematical modeling of layer crystallization on a cold column with recirculation. *Industrial & Engineering Chemistry Research*, 55(17):5019–5029, 2016. ISSN 0888-5885.

Q. Yu, W. Jia, J. Pu, Y. Wang, and H. Yang. Cocrystallization of urea and succinic acid in “nano-crystallizer”. *Chemical Engineering Science*, 229:116082, 2021. ISSN 0009-2509.

G. P. Zago, F. M. Penha, and M. M. Seckler. Product characteristics in simultaneous crystallization of NaCl and $CaSO_4$ from aqueous solution with seeding. *Desalination*, 474:114180, 2020. ISSN 0011-9164.

List of Publications

Journal articles

C. Helfenritter and M. Kind. Determination of crystal growth rates in multi-component solutions. *Crystals*, 12(11):1568, 2022a.

C. Helfenritter and M. Kind. Multi-component diffusion in the vicinity of a growing crystal. *Crystals*, 12(6):872, 2022b.

Conference contributions

C. Helfenritter and M. Kind. Stratification of multi-component solutions on crystalline substrates (Poster). 21st International Symposium on Industrial Crystallization, 30.08. - 02.09.2021, online.

C. Helfenritter and M. Kind. Estimation of crystal growth rates from multicomponent thin films (Talk). Annual meeting of the ProcessNet Working Party on Crystallization, 18.03. - 19.03.2021, online.

C. Helfenritter, A. Roth, and M. Kind. Spektroskopische Untersuchungen des Kristallwachstums von mehrkomponentigen, wässrigen Elektrolytsystemen (Poster). Annual meeting of the ProcessNet Working Party on Crystallization, 12.03. - 13.03.2019, Bamberg, Germany.

C. Helfenritter and M. Kind. Experimentelle Untersuchung des Verfestigungsverhaltens von Mehrkomponenten-Granulaten (Poster). Annual meeting of the ProcessNet Working Party on Crystallization, 06.03. - 09.03.2018, Bremen, Germany.

Student theses conducted in conjunction with this thesis

A. Roth. *Methode zur Bestimmung des Konzentrationsprofils in mehrkomponentigen Elektrolytlösungen in der Nähe von wachsenden Kristallflächen.* Master thesis, 09/2018.

A. Potthoff. *Untersuchung des Kristallwachstums aus mehrkomponentigen dünnen Filmen mittels inverser konfokaler Raman Spektroskopie.* Bachelor thesis, 02/2019.

J. Sanders. *Untersuchung des Flüssig-Fest-Phasengleichgewichts von mehrkomponentigen, wässrigen Elektrolytlösungen.* Bachelor thesis, 02/2019.

Q. Jünemann. *Methode zur Bestimmung des Konzentrationsprofils dünner trocknender Elektrolytlösungsfilme.* Master thesis, 06/2019.

S. Höll. *Untersuchung der Schichtenbildung bei der Erstarrung von mehrkomponentigen Elektrolytlösungen auf Salzsubstraten.* Bachelor thesis, 09/2019.

K. Swaid. *Untersuchung der Schichtenbildung bei der Erstarrung von mehrkomponentigen Elektrolytlösungen auf Salzsubstraten bei variierten Trocknungsbedingungen.* Bachelor thesis, 01/2020.

K. Bauer. *Untersuchung der Schichtenbildung bei der Erstarrung von mehrkomponentigen Elektrolytlösungen auf Salzsubstraten bei variierten Kühlraten.* Bachelor thesis, 08/2020.

N. Ritter. *Untersuchung des Kristallwachstums aus mehrkomponentigen dünnen Filmen mittels inverser konfokaler Raman Spektroskopie mit einem hochviskosen Stoffsystem.* Bachelor thesis, 08/2020.

R. Samman. *Bestimmung metastabiler Zonen des Stoffsystems Natriumsulfat-Natriumcarbonat-Wasser.* Bachelor thesis, 09/2020.

T. Kieble. *Untersuchung der Schichtenbildung bei der Erstarrung von mehrkomponentigen Elektrolytlösungen auf Salzsubstraten in komplexen Phasengebieten.* Bachelor thesis, 10/2020.

M. Gratzfeld. *Bestimmung metastabiler Zonen des Stoffsystems Natriumsulfat-Natriumcarbonat-Wasser bei unterschiedlichen Keimbildungsarten.* Master thesis, 11/2021.

List of Figures

List of Tables

A Appendix

A.1 Generation of supersaturation through drying

Experiments on layer formation were performed either by supersaturation by cooling or by drying. In the following, principles of drying and channel design will be addressed.

A.1.1 Theory

In Figure A.1, the principle of a drying liquid film is depicted. An air flux coming from the left takes up solvent from the film. Above the film, a hydrodynamic boundary layer develops as a function of the air flux. At higher fluxes, the layer diminishes [Brenn, 2016].

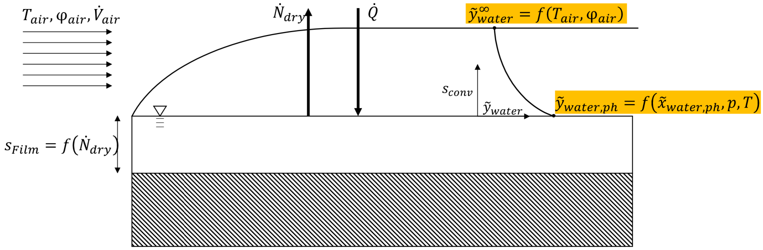

Figure A.1: Schematic depiction of film drying through forced convection.

The difference in molar fractions of water in the gas stream at the fluid phase boundary $\tilde{y}_{\text{water,ph}}$ and in the core of the stream $\tilde{y}^{\infty}_{\text{water}}$ represent the driving force of molar flux $\dot{N}_{\text{dry}}$ (Equation A.1).

$$\dot{N}_{\text{dry}} = A_{ph} \cdot \beta_{\text{water,air}} \cdot \tilde{\rho}^{L} \cdot \ln\left(\frac{1 - \tilde{y}_{\text{water}}^{\infty}}{1 - \tilde{y}_{\text{water,ph}}}\right) \tag{A.1}$$

The heat transfer Q to the film can be described with an energy balance at stationary conditions (Equation A.2).

$$\frac{dH}{dt} = 0 = \dot{Q} - \dot{N}_{\text{dry}} \cdot \Delta\tilde{h}_{v,\text{water}}(T) \tag{A.2}$$

It equals the molar flux multiplied with specific heat of vaporization of water $\Delta\tilde{h}_{v,\text{water}}(T)$. The law of Raoult-Dalton relates solution composition $\tilde{x}_{\text{water,ph}}$ with the molar fraction at the gas-liquid interface (Equation A.3).

$$\tilde{y}_{\text{water,ph}} \cdot p = \tilde{x}_{\text{water,ph}} \cdot \gamma \cdot p^{*}_{\text{water}}(T) \tag{A.3}$$

Thus, it is also a function of the actual pressure p, the temperature dependent water vapor pressure $p^{*}_{\text{water}}(T)$, and activity coefficient γ. The molar fraction in the gas stream can be calculated with the knowledge of pressure p, water vapor pressure $p^{*}_{\text{water}}(T)$, and relative humidity φ (Equation A.4).

$$\tilde{y}^{\infty}_{\text{water}} \cdot p = \varphi \cdot p^{*}_{\text{water}}(T) \tag{A.4}$$

The Sherwood relation is used to calculate the mass transfer coefficient $\beta_{\text{water,air}}$ (Equation A.5).

$$Sh = \frac{\beta_{\text{water,air}} \cdot L_{\text{char}}}{D_{\text{water,air}}} \tag{A.5}$$

The characteristic length L_{char} of a horizontal even plane is its length and diffusion coefficient of water in air $D_{\text{water,air}}$ can be calculated with the Fuller equation (Equation A.6) [Fuller et al., 1966].

$$\frac{D_{\text{water,air}}}{\text{cm}^2 \cdot \text{s}^{-1}} = \frac{0.00143 \cdot \left(\frac{T}{\text{K}}\right)^{1.75} \cdot \left[\left(\frac{\tilde{M}_{\text{water}}}{\text{g}\cdot\text{mol}^{-1}}\right)^{-1} + \left(\frac{\tilde{M}_{\text{air}}}{\text{g}\cdot\text{mol}^{-1}}\right)^{-1}\right]^{-1/2}}{\frac{p}{bar} \cdot \sqrt{2} \cdot \left[(\sum \Delta_{\nu_{\text{water}}})^{1/3} + (\sum \Delta_{\nu_{\text{air}}})^{1/3}\right]^{2}} \tag{A.6}$$

The molar volumes of air $\Delta_{\nu_{\text{air}}} = 19.7$ and water $\Delta_{\nu_{\text{water}}} = 13.1$ can be taken from Stephan et al. [2019]. From empirical correlations that are given in Stephan et al. [2019], Sherwood numbers can be calculated for free convection and forced convection. Beginning with free convection, the correlation is dependent on Rayleigh number Ra and Schmidt number Sc (Equation A.7).

$$Sh_{\text{free}} = 0.766 \cdot [Ra \cdot f_2(Sc)]^{1/5} \tag{A.7}$$

Forced convection is correlated as a function of Reynolds number and Schmidt number (Equation A.8) [Stephan et al., 2019].

$$Sh_{\text{forced}} = 0.664 \cdot Re^{1/2} \cdot Sc^{1/3} \tag{A.8}$$

The dimensionless numbers are calculated as follows (Equations A.9) [Stephan et al., 2019].

$$Ra = Gr \cdot Sc \tag{A.9a}$$

$$f_2(Sc) = \left[1 + \left(\frac{0.322}{Sc}\right)^{11/20}\right]^{-20/11} \tag{A.9b}$$

$$Sc = \frac{\nu_{\text{air}}}{D_{\text{water,air}}} \tag{A.9c}$$

$$Gr = \frac{g \cdot L_c^3 \cdot \Delta\rho}{\nu_{\text{air}}^2 \cdot \rho_{\text{air}}^{\infty}} \tag{A.9d}$$

$$Re = \frac{w_{\text{air}} \cdot L_c}{\nu_{\text{air}}} \tag{A.9e}$$

$$\tag{A.9f}$$

A.1.2 Design of drying channel

A drying channel is designed to supersaturate a solution gradually. Results of such experiments are shown in Section 4.3.2 in Figures 4.31 and 4.32. It is constructed so that an air stream is hydrodynamically fully developed at the position of the sample carrier. Laminar flow is required because the phase transfer should not be too high since nucleation on the surface should be prevented. Turbulent air flow would increase phase transition so that this restriction would not be met. The channel design corresponds to a Carnotian diffuser. To meet a fully developed flow, the length of the channel up to the carrier is calculated with Equation A.10 [Kümmel, 2013].

$$L_{\text{channel,th}} = 10 \cdot d_h \tag{A.10}$$

The channel has a rectangular cross section and is made of aluminum. The hydraulic diameter of the cross section can be calculated with $d_h = 4 \cdot A_{\text{cs}}/L_{\text{circumference}} = 4 \cdot 0.05 \cdot 0.06/0.22\ \text{m}^2$. An additional safety coefficient of 1.05 is applied to fully ensure a developed flow. Hence, the final length is calculated to $L_{\text{channel}} = 572, 73\ \text{mm} \approx 570\ \text{mm}$. The top cover is made from Plexiglas® (thickness of 19 mm) to give the opportunity to observe the process. All surfaces are isolated with a 2 cm layer of insulation material (AF/Armaflex®, $\lambda = 0.033$ W m^{-1} K^{-1}). The channel is pictured in Figure 4.23.

The temperature and humidity of the air flowing through the channel is set with a thermostat and a tempered bubble column. A bypass adjusts the volume flux. Humidity and temperature are measured above the sample. The volume flux of dry air is set in front of the bubble column and the thermostat. It is adjusted with two flow-meters (Q-Flow 140, Vögtlin). The channels body temperature is set to the air flow temperature. The total set-up is depicted in Figure A.2.

Due to that, it can be assumed that the temperature of the solution in the carrier has also this temperature. A temperature difference measurement of a sample containing water is conducted to show the validity of this assumption (compare Figure A.3). The air stream conditions were: air volume flux of 50 L min^{-1}, air temperature of 25°C, and a relative humidity of 6%. The temperature offset is 1.2 K at maximum which is why it is neglected. In experiments, conditions were normally set to lower drying rates. It will remain at air temperature and does not decrease due to evaporation. Thus, isothermal conditions prevail. This is important because of the temperature dependency of the phase equilibrium.

To obtain different drying rates humidity is varied. Drying temperature can also be varied to change phase equilibrium. The third parameter - air volume

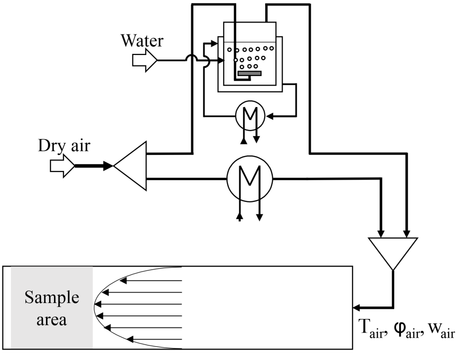

Figure A.2: Schematic drawing of the drying set-up. Humidity is adjusted with a bypass stream of air through a tempered bubble column. Air and channel are both adjusted to similar temperatures.

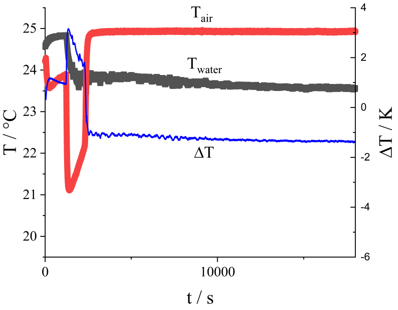

Figure A.3: Steady-state temperature measurement of drying water and air in the tempered drying channel.

flow - is kept constant at 40 L min^{-1}. The empty channel is set to experimental conditions and is kept that way for at least one hour. Then, a carrier device is prepared as described in Section 4.3.1. It is inserted in the drying channel and evaporation starts immediately. If there is no more remaining solution visible, the experiment is aborted. It is important to observe the exact point because of efflorescence. The hydrate will give up its water to the external air due to low partial pressure of water. Afterwards, the carriers are covered with laboratory foil and stored in a fridge at 8°C until the layers are analyzed according to Section 4.3.1.

A.2 Heat-mass-transfer analogy

In addition to multi-component diffusion modeling in Section 4.2.1, it is also possible to justify a single measurement point with heat-mass transfer analogies. Film diffusion can be compared with transient heat conduction in a slab.

Schlünder [1972], Martin and Saberian [1994], and Martin et al. [2019] developed asymptotic approximations to Fourier's solution of the transient heat conduction equation in a stagnant body (slab, cylinder, sphere). They defined an internal and time-dependent heat transfer coefficient (Equation A.11).

$$\alpha_{\text{int}} \equiv \frac{\dot{Q}}{A(\bar{T} - T_0)} \tag{A.11}$$

The term $\dot{Q}/A$ is the heat flux to the environment, T_0 the temperature at the surface of the body and $\bar{T}$ the caloric mean temperature of the body. Initially, they found that this heat transfer coefficients is time-dependent (short-time approximation) and then becomes constant (long-time approximation). From Fourier's solution, general equations for both approximations were derived.

Under the boundary condition of constant surface temperature, $T_0 =$ const. or Biot number $Bi \to \infty$, the long-time approximation simplifies to:

$$Nu \left(\equiv \frac{\alpha_{\text{int}} X}{\lambda} \right) = \frac{1 + 2 + Bi}{1 + Bi/\frac{\pi^2}{4}} \approx \frac{\pi^2}{4} \tag{A.12}$$

The long-time approximation holds, if the dimensionless time $\tau(\equiv \kappa t/X^2) > 0.5$. Also, approximations for estimating average slab temperature $\bar{\Theta}$ and center temperature Θ_c are derived (Equations A.13).

$$\bar{\Theta}\left(\equiv\frac{\bar{T}-T_0}{T_{\text{init}}-T_0}\right)=\exp(-Nu\cdot\tau) \tag{A.13a}$$

$$\Theta_c\left(\equiv\frac{T_c-T_0}{T_{\text{init}}-T_0}\right)=\exp(-Nu\cdot\tau_c) \tag{A.13b}$$

$$\tag{A.13c}$$

Temperature T_{init} represents initial temperature and $\Delta\tau$ is the time lag between center temperature and mean caloric temperature. The dimensionless time in the center follows: $\tau_c = \tau - \Delta\tau$.

If the long-term approximation prevails, the temperature difference between the surface and the center $\Delta T = T_c - T_0$ is similar to the mean temperature difference. Hence, internal heat transfer coefficients can be retrieved from transient measurements of temperature at one position.

In analogy, this applies also for mass transfer in a thin film in the vicinity of a crystallizing substrate. The internal heat transfer coefficient α_{int} becomes the internal growth coefficient $k^{'}_{g,i}$ in the power law function (A.14).

$$\dot{n}_i = k^{'}_{g,i}\cdot(\bar{c}_i - c_{i,0})^g \tag{A.14}$$

Besides transfer coefficients, the other analogues in mass transfer are concentration c_i of component i replacing temperature T, diffusion coefficient D_i replacing thermal diffusivity κ and thermal conductivity λ, and Sherwood-number Sh replacing Nusselt-number Nu. It is known from crystal growth theories that the mass transfer coefficient $k^{'}_{g,i}$ may be a function of supersaturation [Garside et al., 2002]. To take this into account, a mean coefficient $k_{g,i}$ is used, which is not supersaturation dependent (Equation A.15).

$$\dot{n}_i = k_{g,i}\cdot(\bar{c}_i - c_{i,0})^g \tag{A.15}$$

If the film thickness of 150 µm from crystal growth experiments is taken and if an assumed diffusion coefficient of 10^{-9} m^2 s^{-1} prevails, then the long-time approximation is achieved already 11 s after contacting the substrate with superor undersaturated film. Thus, at $\tau > 0.5$ the mean concentration difference is similar to the maximum difference. Similar time ranges were observed in multi-component diffusion simulations. In Figure 4.15 (d), constant values of $k_{g,i}$ were achieved after 10 s. Hence, simulation and theoretical derivation come to similar results.

A.3 Layer simulation model

In this section, the model equations and assumptions of the simulation case studies in Chapter 3 are presented. The simulation is aligned with spatial dimensions from stratification experiments. Hence, the crystallization area is a square with side length of 0.043 m. The initial thickness is calculated with the solution density ρ^L_{mix} (Equation A.16) and the initial mass M_{init} of 2 g.

$$\rho^L_{mix} = (x_{\text{H}_2\text{O},init}/\rho^L_{\text{solvent}} + x_{\text{Na}_2\text{SO}_4,\text{init}}/\rho^S_{\text{Na}_2\text{SO}_4} + x_{\text{Na}_2\text{CO}_3,\text{init}}/\rho^S_{\text{Na}_2\text{CO}_3})^{-1} \quad \text{(A.16)}$$

It is assumed that the mixture density ρ^L_{mix} can be calculated with a weighted sum of the solvent density ρ^L_{solvent} and the solid densities of sodium sulfate decahydrate $\rho^S_{\text{Na}_2\text{SO}_4}$ and sodium carbonate decahydrate $\rho^S_{\text{Na}_2\text{CO}_3}$. All calculations are conducted with Matlab® 2019b. For initialization, start temperature, substrate material and initial mass fractions have to be specified. Also, cooling rate $\dot{T}_{\text{cool}}$ and crystal growth kinetics - in form of power law function (compare Equation 2.10c) - are fixed. The material properties are assumed to be constant over the temperature range with exception of water density ρ^L_{water} and viscosity η^L_{water} which are calculated as a function of temperature. The polynomial functions are fits of literature data [Stephan et al., 2019]. All constant and temperature dependent variables are listed in Table A.1.

Each time step, the saturation state of the involved materials are calculated using a plug-in of the geochemical calculation program PHREEQC Version 3 [Parkhurst and Appelo, 2013]. The database *FREZCHEM* is applied to calculate phase equilibria of the material system Na_2SO_4-Na_2CO_3-H_2O [Marion et al., 2010; Toner and Sletten, 2013]. The output of the plug-in are the actual and

Table A.1: List of simulation variables. Temperature dependent values are functions with respect to °C-temperatures.

variable	value / temperature function	unit
$\tilde{M}_{\mathrm{H_2O}}$	0.018	kg mol-1
$\tilde{M}_{\mathrm{Na_2SO_4}}$	0.142	kg mol-1
$\tilde{M}_{\mathrm{Na_2CO_3}}$	0.106	kg mol-1
ρ^L_{water}	$3 \cdot 10^{-5} \cdot T^3 - 0.0075 \cdot T^2 + 0.0541 \cdot T + 999.87$	kg m-3
$\rho^S_{\mathrm{Na_2SO_4 \cdot 10H_2O}}$	1460 (source: Carl Roth GmbH + Co. KG, CAS Nr. 7727-73-3)	kg m-3
$\rho^S_{\mathrm{Na_2CO_3 \cdot 10H_2O}}$	1460 (source: Carl Roth GmbH + Co. KG, CAS Nr. 6132-02-1)	kg m-3
η^L_{water}	$(2 \cdot 10^{-8} \cdot T^3 - 0.00001 \cdot T^2 - 0.1966 \cdot T + 127)$	µPa s
A_{cryst}	$1.85 \cdot 10^{-3}$	m2
M_{init}	0.002	kg

equilibrium activity of the components and the supersaturation. Hence, if one or more components are supersaturated, crystallization is possible. As explained in Chapter 3, no metastable states are considered. Thus, a supersaturation leads automatically to growth. Nucleation is also neglected. Crystallization fluxes follow Equation 2.10c. The liquid film is assumed to be ideally mixed. No gradients occur within. Hence, mass balances of components *i* in the film volume follow Equation A.17.

$$\frac{dN_i}{dt} = -\dot{n}_{i,\mathrm{cryst}} \cdot A_{\mathrm{cryst}} \tag{A.17}$$

The calculated molar flux of crystallizing entity $\dot{n}_{i,\mathrm{cryst}}$ is divided into molar fluxes of each component in solution. Hence, for each molecule of crystallizing decahydrate, ten moles of water are removed from the solution. From changing moles, new molar fractions are calculated (Equation A.18).

$$\tilde{x}_i = \frac{N_i}{\sum N_j} \tag{A.18}$$

At the end of a time step, temperature is adapted according to Equation A.19.

$$T = T - \dot{T}_{\text{cool}} \cdot \Delta t \tag{A.19}$$

Time steps are chosen to be $\Delta t = 0.01$ s. The process ends with reaching a desired temperature T_{end} or a defined end time t_{end}.

A.4 Phase equilibrium of Na_2SO_4-Na_2CO_3-H_2O at 30℃

As was mentioned in Section 4.1, the phase behavior of Na_2SO_4-Na_2CO_3-H_2O changes at temperatures above 30°C. In Figure A.4, the triangular diagram with its four stable solid phases is shown.

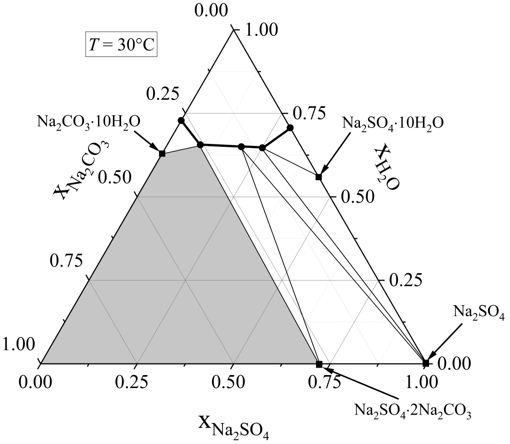

Figure A.4: Triangular diagram of Na_2SO_4-Na_2CO_3-H_2O at 30°C. The data points on the solubility line (black points) are taken from Caspari [1924]. The connections are linearly interpolated.

In addition to the already introduced solid equilibrium states ($Na_2SO_4 \cdot 10H_2O$ and $Na_2CO_3 \cdot 10H_2O$), sodium sulfate anhydrate (Na_2SO_4) and Burkeite ($Na_2SO_4 \cdot 2Na_2CO_3$) are stable solid entities at temperatures above 30°C. Due to the higher amount of solid states, two additional eutectic points occur. At higher temperatures, the phase behavior does not change significantly compared to the one presented.

A.5 Calibration of Raman spectroscopic arrangements

For analytics in Sections 4.1 and 4.3 and crystal growth experiments in Section 4.2, calibration functions had to be determined. Because the experimental set-ups were different for analytics and crystal growth, two different calibration functions had to be found. For the calibration of the crystal growth set-up, the same experimental cell was used as for the experiments (compare Figure 4.16). The analytical set-up is a tempered metal cylinder, which can incorporate a small glass vial (diameter of 11.6 mm, volume of 1.5 mL). A hole in the bottom of the cylinder allows the laser beam to be focused into the glass vial. Since there is no need for spatial resolution, a lens with a rather low resolution is used (Olympus "M-Plan" 10x/0.25). In Figure A.5, the set-up is depicted schematically.

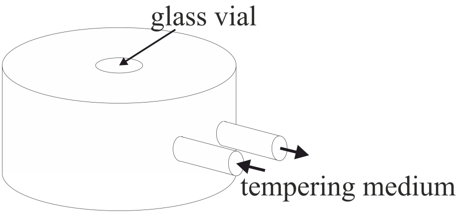

Figure A.5: Depiction of the analytical set-up. The objective (not shown) focuses the laser beam into the tempered glass vial from below.

Generally, ternary mixtures of both salts and water with known compositions were used. The peak areas of sulfate, carbonate and water peaks were taken as measure of intensity (compare Figure 4.17). The integration boundaries were determined from slope analysis and set to the point where slope changed its sign or the inclination was lower 0.0025. To apply Equation 4.12, water was chosen to be the internal reference material. Since the cations had no characteristic peak, the intensities of the anion peaks were related to the intensity of the water peak. All calibration functions were forced through the origin. In Figure 4.17, functions of both salts dissolved in water are shown at 25°C for the desupersaturation set-up. The corresponding solutions are displayed as squares and diamonds in the ternary diagram in Figure A.6.

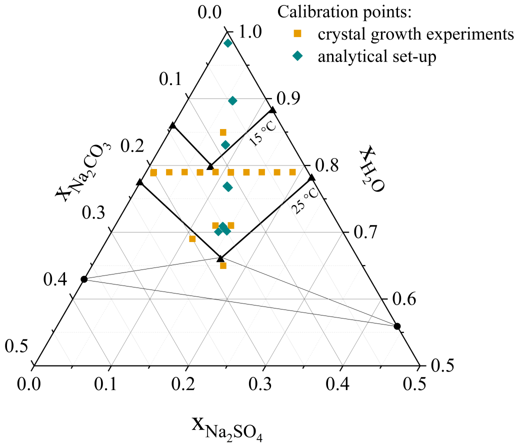

Figure A.6: Calibration solutions of both Raman spectroscopic arrangements. Blue diamonds belong to the analytical set-up. Orange squares show concentrations of crystal growth arrangement.

Blue diamonds represent compositions which were used for calibrating the analytical set-up. For crystal growth experimental set-up, two independent solutions at all displayed concentrations (orange squares) were prepared. Calibration was repeated for other temperatures in the range of 20 to 30°C. The calibration factors at different temperatures for both set-ups are summarized in Table A.2. In addition, the averaged factors are shown.

Also, the residual standard deviations (RSD) of all averaged functions at all temperatures are given. The RSD is defined as the square root of the sum of square errors divided by the degrees of freedom (compare Eq. A.20). Here, the degrees of freedom are sample number n minus one.

Table A.2: List of Raman calibration constants K_i for Equation 4.12 of Na_2SO_4 and Na_2CO_3 dissolved in water at different temperatures. The mean values correspond were used in experiments. Additionally, residual standard deviations (RSD) are given. These were calculated at each temperature with mean calibration constants.

	crystal growth				solution analytics			
	Na_2SO_4		Na_2CO_3		Na_2SO_4		Na_2CO_3	
T / °C	K	RSD	K	RSD	K	RSD	K	RSD
20	5.67	0.002	11.07	0.007	-	-	-	-
23.5	5.74	0.004	11.54	0.008	-	-	-	-
25	5.57	0.003	11.09	0.008	6.60	0.0007	13.54	0.0014
30	5.62	0.003	11.31	0.007	6.58	0.0005	13.56	0.0014
mean	5.65	-	11.25	-	6.59		13.55	

$$RSD = \sqrt{\frac{\sum(X_i - \hat{X}_i)^2}{n-1}} \tag{A.20}$$

Thus, the RSD displays the agreement of the calibration function with the calibration standards with the unit of mass load.

A.6 Evaporation experiments for homogeneous nucleation

The crystallization system Crystalline (Technobis) is extended with an evaporation add-on which is displayed in Figure A.7.

It consists of an inlet at the top of the reactors which introduces a nitrogen stream. It is adjusted with a flow controller (EL-Flow-Select, Bronkhorst). Additionally, the pressure can be adjusted with a vacuum pump (LVS 105 T - 10 ef, Welch). Since all experiments were conducted at ambient pressure, no adjustment had to be made with the vacuum pump. The volume flux of nitrogen is set to $\dot{V}_{N_2} = 500$ L min^{-1}, which is the maximum possible value. The temperature is set to 25°C. It is recorded with a Pt-100 resistance thermometer. The nitrogen

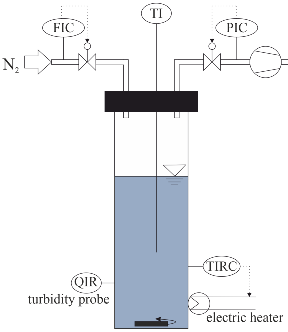

Figure A.7: Schematic depiction of evaporation add-on for Crystalline system.

stream has no content of water and impacts the fluid surface as an impinging jet. The drying flux $\dot{N}_{\text{dry}}$ can be calculated with the Equation A.21.

$$\dot{N}_{dry} = A_{ph} \cdot \beta_{\text{water,N}_2} \cdot \tilde{\rho}^L \cdot \ln\left(\frac{1}{1 - \tilde{y}_{\text{water},ph}}\right) \tag{A.21}$$

Mass transfer coefficient $\beta_{\text{water,N}_2}$ can be calculated with Sh-correlation for impinging jets taken from Martin [1977].

$$Sh\left(\equiv \frac{\beta_{\text{water,N}_2} \cdot L_c}{D_{\text{water,N}_2}}\right) = \frac{(1 - 1.1)/r^*}{r^* + 0.1 \cdot (h^* - 6)} \cdot F(Re) \cdot Sc^{0.42} \tag{A.22}$$

The definition of $F(Re)$ and geometric variables r^* and h^* are as follows:

$$F(Re) = a \cdot Re^b \tag{A.23a}$$

$$r^* = \frac{r_{\text{reactor}}}{d_{\text{jet}}} \tag{A.23b}$$

$$h^* = \frac{H_0 + h(t)}{d_{\text{jet}}} \tag{A.23c}$$

Function $F(Re)$ is an empirical correlation of Reynolds number with constants a and b. Geometric variables are with respect to the jet diameter d_{jet} and represent the reactor radius r_{reactor} and the distance of the jet from the liquid surface. It changes with time which is why the term $H_0 + h(t)$ is chosen. The reduction of liquid is considered with $h(t)$. Equation A.21 applies under ideal conditions. Due to the high electrolyte content in solution, water activity is low and evaporation mass transfer reduced. Hence, the final realistic mean evaporation fluxes are in a range of 0.001 - 0.009 g min^{-1}. The initial solution compositions are summarized in Table A.3.

Table A.3: List of initial solution compositions for evaporation experiments on homogeneous nucleation.

	$x_{\mathrm{Na_2SO_4}}$	$x_{\mathrm{Na_2CO_3}}$	$x_{\mathrm{H_2O}}$
1	0.162	0.179	0.659
2	0.050	0.200	0.750
3	0.180	0.070	0.750

In Figure 4.6 (b), the nucleation points are depicted as stars. The description and interpretation of the results can be read at the end of Section 4.1.2.

A.7 Self-diffusion coefficients of water and carbonate ions

For multi-component diffusion simulations, self-diffusion coefficients are needed. As stated in Section 4.2.1, it is possible to determine self- coefficients from spin-echo method of Hahn [1950].

The ^{1}H and ^{13}C PFG-STE measurements were performed at 293.5 K with a 400 MHz spectrometer of Bruker (Ultrashield. Bruker BioSpin, Germany, probe: DiffBB). The experimental adjustments and conditions are summarized in Table A.4.

With ^{1}H-NMR-diffusometry measurements at 293.5 K, self-diffusion coefficients of water were determined at different solution compositions. The same

Table A.4: Experimental adjustments and conditions of NMR measurements.

variable	value
Number of averages (-)	8
Repetition time τ_r (s)	4
Diffusion time Δ (ms)	100
Number of increments (-)	16
Gradient duration δ (ms)	2
Gradient amplitude g (T/m)	1.00
Temperature T (K)	293.5

solutions were investigated with respect to carbonate ion diffusion with ^{13}C-NMR-diffusometry. In Figure A.8, the signal decay of a solution containing $x_{\mathrm{Na_2SO_4}} = 0.15$ and $x_{\mathrm{Na_2CO_3}} = 0.11$ of a ^{1}H and a ^{13}C measurement are shown exemplarily.

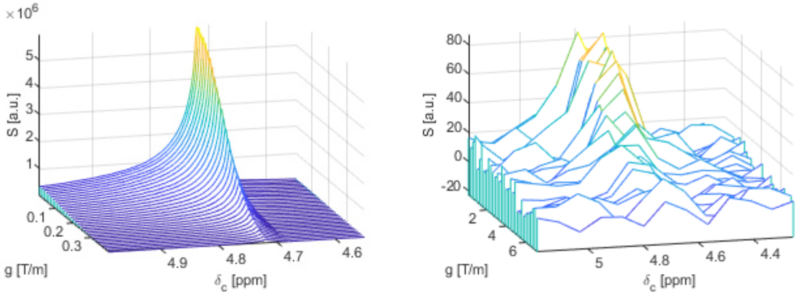

(a) **(b)**

Figure A.8: (**a**) ^{1}H-PFG-STE-NMR spectra of a sample with $x_{\mathrm{Na_2SO_4}} = 0.15$ and $x_{\mathrm{Na_2CO_3}} = 0.11$. (**b**) ^{13}C-PFG-STE-NMR spectra of the same sample.

The signal decay of both ^{1}H and ^{13}C were modeled with the exponential correlation by Stejskal and Tanner [1965] (Equation A.24) to obtain the self-diffusion coefficient D.

$$\frac{S(q)}{S_0} = \exp(-D \cdot q^2 \cdot (\Delta - \delta/3)) \tag{A.24}$$

The parameter q represents the product of the proton magnetogyric ratio γ, the gradient amplitude g, and the gradient pulse duration δ. The signal intensity $S(q)$ is standardized by the intensity at $q = 0$ S_0. The decay is also a function of the diffusion time Δ. With it, it was possible to determine the self-diffusion coefficient of water and carbonate ions at different concentrations of sodium carbonate and sodium sulfate (Figure A.9).

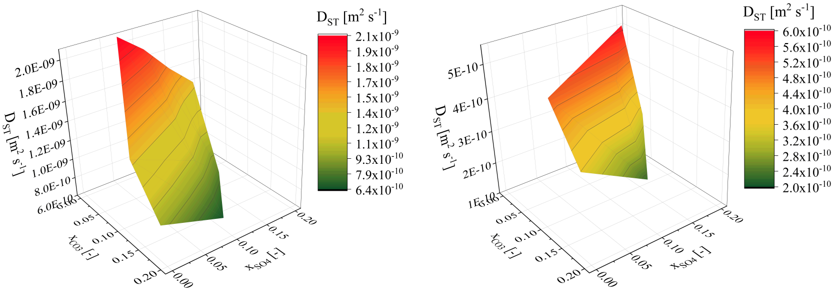

(a) **(b)**

Figure A.9: (**a**) Self-diffusion coefficient of H_2O in dependence of electrolyte mass fraction of sodium carbonate $x_{Na_2CO_3}$ and sodium sulfate $x_{Na_2SO_4}$ at 293.5 K. In (**b**), self-diffusion coefficient of Carbonate ions $CO_3{}^{2-}$ are plotted as a function of sodium sulfate and sodium carbonate mass fraction.

In Table A.5, all determined diffusion coefficients of water are listed.

It can be seen that the self-diffusion coefficient of water D_{water} lay in the range of 0.5 - 2 $\cdot 10^{-9}$ m^2 s^{-1}. For diffusion simulation, a constant water diffusivity of 1 $\cdot 10^{-9}$ m^2 s^{-1} was assumed.

With ^{13}C-NMR-diffusometry measurements at 293.5 K, self-diffusion coefficients of carbonate ions ($CO_3{}^{2-}$) were investigated in binary and ternary solutions. The results are listed in Table A.6.

At rather high concentrations of carbonate the self-diffusion coefficient lied in a range of 0.2 - 0.6 $\cdot 10^{-9}$ m^2 s. At simulation compositions which were rather high,

Table A.5: List of measured self-diffusion coefficients of water from ^{1}H-NMR-diffusometry measurements at 293.5 K.

$x_{\mathrm{Na_2SO_4}}$	$x_{\mathrm{Na_2CO_3}}$	$D_{\mathrm{H_2O}}/\ \mathrm{m^2\ s}$
0	0.19	$9.89 \cdot 10^{-10}$
0	0.19	$9.59 \cdot 10^{-10}$
0	0.13	$1.42 \cdot 10^{-9}$
0	0.13	$1.39 \cdot 10^{-9}$
0.19	0	$1.42 \cdot 10^{-9}$
0.19	0	$1.39 \cdot 10^{-9}$
0.15	0	$1.64 \cdot 10^{-9}$
0.15	0	$1.62 \cdot 10^{-9}$
0.11	0	$1.93 \cdot 10^{-9}$
0.11	0	$1.87 \cdot 10^{-9}$
0.07	0	$2.10 \cdot 10^{-9}$
0.07	0	$2.09 \cdot 10^{-9}$
0.11	0.11	$1.01 \cdot 10^{-9}$
0.11	0.11	$1.09 \cdot 10^{-9}$
0.11	0.17	$6.32 \cdot 10^{-10}$
0.11	0.17	$6.56 \cdot 10^{-10}$
0.15	0.11	$8.26 \cdot 10^{-10}$
0.15	0.11	$8.20 \cdot 10^{-10}$
0.15	0.07	$1.06 \cdot 10^{-9}$
0.15	0.07	$1.08 \cdot 10^{-9}$

the lower diffusion coefficients prevail. Hence, a value of 0.3 $\cdot 10^{-9}$ m^2 s was assumed. The self-diffusion coefficient of sulfate ions (SO_4^{2-}) was not investigated. Nielsen et al. [1952] determined the self-diffusivity to be 0.6 $\cdot 10^{-9}$ m^2 s at rather high concentrations (3 mol L^{-1}) in binary solutions at 293.5 K. For simulations it was assumed that the diffusivity was a little lower because of higher prevailing concentrations. As can be seen from results of CO_3^{2-}-diffusion coefficients decrease with increasing concentrations of both components. This behavior is

Table A.6: List of measured self-diffusion coefficients of carbonate ions (CO_3^{2-}) from ^{13}C-NMR-diffusometry measurements at 293.5 K.

$x_{Na_2SO_4}$	$x_{Na_2CO_3}$	$D_{CO_3^{2-}}$ / m^2 s
0	0.19	$3.59 \cdot 10^{-10}$
0	0.13	$5.26 \cdot 10^{-10}$
0	0.13	$4.81 \cdot 10^{-10}$
0.11	0.11	$4.65 \cdot 10^{-10}$
0.11	0.17	$2.27 \cdot 10^{-10}$
0.15	0.11	$3.41 \cdot 10^{-10}$
0.15	0.07	$5.71 \cdot 10^{-10}$

also assumed for SO_4^{2-}-diffusion coefficients. An equal self-diffusion coefficient compared to carbonate of $0.3 \cdot 10^{-9}$ m^2 s was assumed for calculations.

A.8 Results of homogeneous nucleation at other temperatures

In Figure A.10, results from homogeneous nucleation at 15°C ((a) and (b)) and 25°C ((c) and (d)) are depicted.

Each minimum ΔT_{met} was used in Figure 4.5. It is noticeable that most of the solutions saturated at 15°C had to be subcooled to lowest temperature of -9°C at least once. Nevertheless, highest nucleation temperatures were in the range of -2°C to 12.5°C. Experiments at 25°C yielded in a closer range of highest nucleation temperatures in a range of -2.5°C to 10°C with an outlier of this trend at 18°C (solution number 7). Additionally, experiments with a lower cooling rate of 0.01 K min^{-1} were conducted (compare Figure A.11).

The cooling rate of 0.01 K min^{-1} produced similar metastable subcoolings like the higher rate (compare Figure A.10 (c) with Figure A.11).

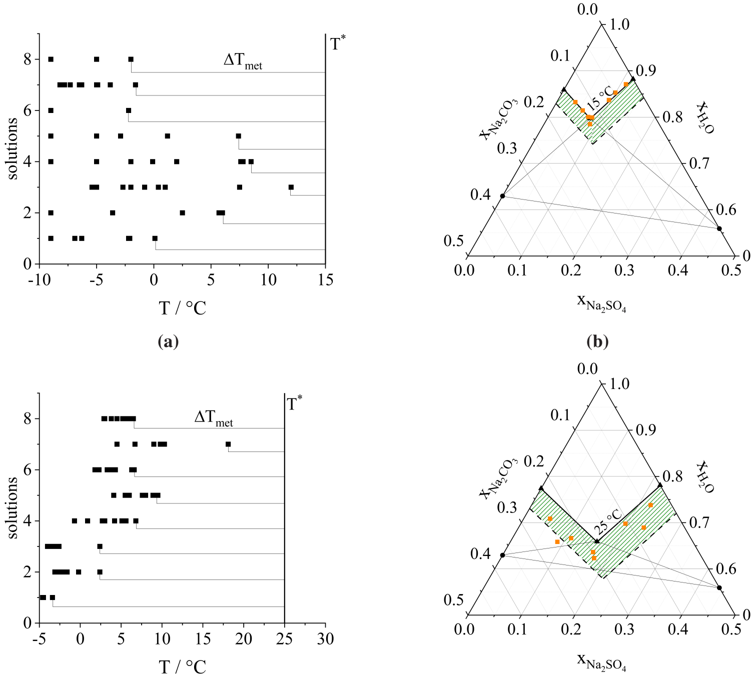

(a) (b)

(c) (d)

Figure A.10: In Diagrams (**a**) and (**c**), metastable supercooling temperatures ΔT_{met} are shown at saturation temperatures of 15°C and 25°C. They result from cooling rates of 0.1 K min^{-1}. Diagrams (**b**) and (**d**) represent the triangle diagrams of Na_2SO_4-Na_2CO_3-H_2O at 15°C and 25°C, respectively. By dashed green areas, the estimated metastable zones are marked. Orange points mark the evaluated solution compositions.

A.9 Additional post-process assessments of solid layers

Additional drying and cooling parameters of experiments in Section 4.3 were investigated. In Figures A.12 and A.13, additional data from drying experiments are shown.

In comparison to results on sodium sulfate substrates at 20°C, final layer heights were 200 µm lower on sodium carbonate. Stratification behavior is similar

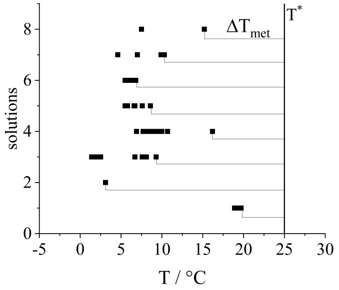

Figure A.11: Metastable supercooling temperatures ΔT_{met} are shown at saturation temperature of 25°C from cooling rates of 0.01 K min^{-1}.

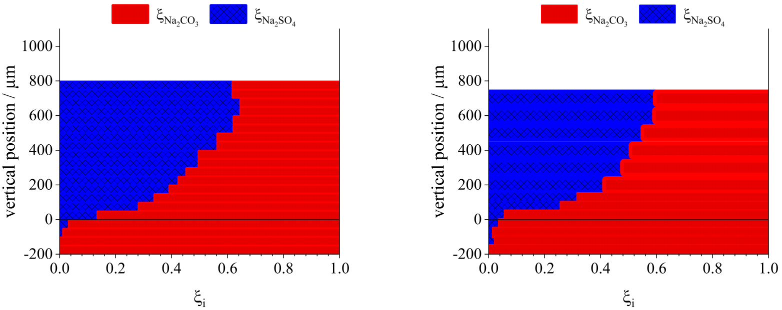

(a) **(b)**

Figure A.12: Diagrams of solid layer composition as a function of vertical position in the assemblage. Blue color represents the fraction of sodium sulfate $\xi_{\mathrm{Na_2SO_4}}$. It is to be read from zero. In red, fraction of sodium carbonate $\xi_{\mathrm{Na_2CO_3}}$ is illustrated. The fraction has to be read from the right. Experiments on sodium carbonate with drying rates of $\dot{m}_{\mathrm{dry}} = 0.015$ g m^{-2} s^{-1} (**e**) and $\dot{m}_{\mathrm{dry}} = 0.109$ g m^{-2} s^{-1} (**f**) at 20°C resulted in layer heights of ≈800 µm. The substrates were not penetrated by foreign component sodium sulfate.

in both experiments regardless of the drying rate ($\dot{m}_{\mathrm{dry}} = 0.015$ g m^{-2} s^{-1} (**e**) and $\dot{m}_{\mathrm{dry}} = 0.109$ g m^{-2} s^{-1}). In the upper layer, the foreign content increased up to 60 %.

In contrast to experiments at 20°C, the final heights of all experiments at 25°C were in the order of 600 µm. The substrates were not penetrated with exception of

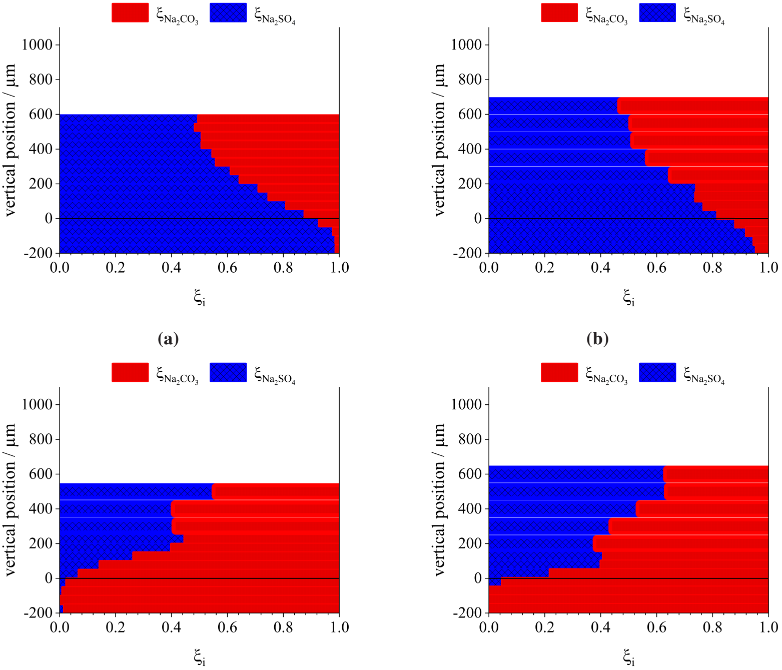

(a) **(b)** **(c)** **(d)**

Figure A.13: Diagrams of solid layer composition as a function of vertical position in the assemblage. Blue color represents the fraction of sodium sulfate $\xi_{\mathrm{Na_2SO_4}}$. It is to be read from zero. In red, fraction of sodium carbonate $\xi_{\mathrm{Na_2CO_3}}$ is illustrated. The fraction has to be read from the right. In Diagram (**a**), the average of three experiments at 25°C with a drying rate of $\dot{m}_{\mathrm{dry}} = 0.176$ g m^{-2} s^{-1} on a sodium sulfate substrate is shown. In Diagram (**b**), the same substrate was used but with a drying rate of $\dot{m}_{\mathrm{dry}} = 0.214$ g m^{-2} s^{-1} at 25°C. The stratification behavior of both is similar. The experiments at higher drying rates showed a higher penetration of the substrate than at lower rates. The final heights are similar with 600 and 700 µm, respectively. In Diagrams (**c**) and **d**, experiments on sodium carbonate substrates are depicted. The drying rates were $\dot{m}_{\mathrm{dry}} = 0.026$ g m^{-2} s^{-1} and $\dot{m}_{dry} = 0.176$ g m^{-2} s^{-1}, respectively. The substrates were not penetrated by the solution and consisted solely of sodium carbonate. Final heights were 550 and 650 µm. At slower drying rates, the increment of foreign component is lower than with higher rates. In contrast, experiments with drying rates of $\dot{m}_{dry} = 0.015$ g m^{-2} s^{-1} (**e**) and $\dot{m}_{\mathrm{dry}} = 0.109$ g m^{-2} s^{-1} (**f**) at 20°C resulted in layer heights of .

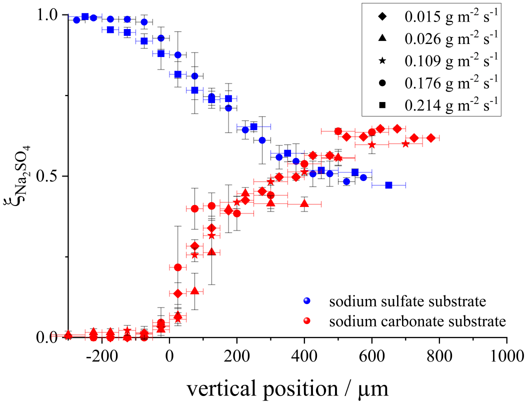

Figure A.14: Steady-state temperature measurement of drying water and air in the tempered drying channel.

experiments with higher drying rates of $\dot{m}_{\mathrm{dry}} = 0.214\ \mathrm{g\ m^{-2}\ s^{-1}}$. The stratification behavior of experiments in Figures A.12 and A.13 can be observed in Figure A.14.

All experiments with equal substrate materials exhibited a similar behavior. The increment of foreign component was lower on sodium sulfate substrates. Hence, a mostly uniform material distribution was achieved on sodium carbonate substrates in early developed layers.